

ANNUAL REPORT ON

**EXPLOITATION OF MICRODOPPLER AND
MULTIPLE SCATTERING PHENOMENA
FOR RADAR TARGET RECOGNITION**

**Office of Naval Research
Research Grant N00014-03-1-0021**

For the period October 1, 2002 through September 30, 2003

Submitted by

Professor Hao Ling

**Department of Electrical and Computer Engineering
The University of Texas at Austin
Austin, TX 78712-1084**

January 15, 2004

DISTRIBUTION STATEMENT A
Approved for Public Release
Distribution Unlimited

20040218 123

REPORT DOCUMENTATION PAGE			Form Approved OMB No. 0704-0188	
Public reporting burden for this collection of information is estimated to average 1 hour per response, including the time for reviewing instructions, searching existing data sources, gathering and maintaining the data needed, and completing and reviewing the collection of information. Send comments regarding this burden estimate or any other aspect of this collection of information, including suggestions for reducing this burden to Washington Headquarters Services, Directorate for Information Operations and Reports, 1215 Jefferson Davis Highway, Suite 1204, Arlington, VA 22202-4302, and to the Office of Management and Budget, Paperwork Reduction Project (0704-0188), Washington, DC 20503.				
1. AGENCY USE ONLY (Leave blank)		2. REPORT DATE Jan. 15, 2004	3. REPORT TYPE AND DATES COVERED Annual Report 1 Oct. 02 - 30 Sept. 03	
4. TITLE AND SUBTITLE Annual Report on Exploitation of MicroDoppler and Multiple Scattering Phenomena for Radar Target Recognition			5. FUNDING NUMBERS Research Grant ONR N00014-03-1-0021	
6. AUTHOR(S) Hao Ling				
7. PERFORMING ORGANIZATION NAMES(S) AND ADDRESS(ES) The University of Texas at Austin Department of Electrical and Computer Engineering Austin, TX 78712-1084			8. PERFORMING ORGANIZATION REPORT NUMBER No. 4	
9. SPONSORING / MONITORING AGENCY NAMES(S) AND ADDRESS(ES) Office of Naval Research Program Officer Ballston Centre Tower One G. D. McNeal 800 North Quincy Street ONR 313 Arlington, VA 22217-5660			10. SPONSORING / MONITORING AGENCY REPORT NUMBER	
11. SUPPLEMENTARY NOTES				
a. DISTRIBUTION / AVAILABILITY STATEMENT Approval for Public Release Distribution Unlimited			12. DISTRIBUTION CODE	
13. ABSTRACT (Maximum 200 words) This report summarizes the scientific progress on the reserach grant "Exploitation of MicroDoppler and Multiple Scattering Phenomena for Radar Target Recognition" during the period 1 October 2002 - 30 September 2003. Research on the construction of a microDoppler radar and the resulting data collection and signal processing is presented. Additional reseach into ray tracing simulation, inverse scattering and time reversal imaging is also reported.				
14. SUBJECT TERMS MicroDoppler, Multiple Scattering, Radar Target Recognition			15. NUMBER OF PAGES 67	
			16. PRICE CODE	
17. SECURITY CLASSIFICATION OF REPORT Unclassified	18. SECURITY CLASSIFICATION OF THIS PAGE Unclassified	19. SECURITY CLASSIFICATION OF ABSTRACT Unclassified	20. LIMITATION OF ABSTRACT	

ANNUAL REPORT ON

**EXPLOITATION OF MICRODOPPLER AND
MULTIPLE SCATTERING PHENOMENA
FOR RADAR TARGET RECOGNITION**

**Office of Naval Research
Research Grant N00014-03-1-0021**

For the period October 1, 2002 through September 30, 2003

Submitted by

Professor Hao Ling

**Department of Electrical and Computer Engineering
The University of Texas at Austin
Austin, TX 78712-1084**

January 15, 2004

EXPLOITATION OF MICRODOPPLER AND MULTIPLE SCATTERING PHENOMENA FOR RADAR TARGET RECOGNITION

Project Starting Date: October 1, 2002

Reporting Period: October 1, 2002 – September 30, 2003

Principal Investigator: Professor Hao Ling
(512) 471-1710
ling@ece.utexas.edu

Graduate Students: M. Anderson, J. Philson, Y. Zhou, A. Bandyopadhyay

A. SCIENTIFIC OBJECTIVES:

Conventional radar signal processing is based on two simplified assumptions about target scattering: (i) that the target is a rigid body; (ii) that the target can be modeled as a collection of independent point scatterers without any multiple scattering effects. However, real radar data can deviate significantly from these two simplified assumptions. First, real-world targets are often observed by radar sensors under dynamic conditions where non-rigid body motions can exist. These non-rigid body motions give rise to "microDoppler" phenomena, which have been observed in a number of SAR and ISAR sensors. Examples of microDoppler phenomena include returns from moving components on the target such as scanning antennas or rotating wheels, as well as those from flexing and vibration of the target frame. Second, strong multiple scattering physics are often encountered in inlets and cavity structures on the target. For instance, the most prominent feature on an air target is often the range-delayed return from the jet inlet duct. Significant modeling work has been carried out by the computational electromagnetics community to characterize the complex scattering from inlet structures, yet little effort has been placed on utilizing the results to develop better imaging algorithms to map the inlet interior. The objectives of this research program are: (i) to gain in-depth understanding of these higher-order phenomena through simulation and measurement, (ii) to develop physics-based models and the associated signal processing strategies to extract the resulting radar features, and (iii) to exploit and utilize these additional features to enhance the performance of automatic target recognition (ATR) algorithms.

B. SUMMARY OF RESULTS AND SIGNIFICANT ACCOMPLISHMENTS:

During the first year of this research program, three areas of investigation have been initiated. First, we have designed, built and tested a low-cost radar sensor for microDoppler data collection. The system costs less than \$3,000 and is tunable between 4 to 10 GHz. Preliminary data from a moving human have been collected and processed. Second, we have begun to develop simulation tools to aid in the interpretation and understanding of microDoppler and multiple scattering phenomena in complex targets. In particular, a multi-platen z-buffer algorithm was investigated for fast ray tracing and the results show promise as a real-time simulation tool. Finally, we have investigated the application of genetic algorithms and time-reversal imaging techniques to improve target-to-clutter performance and to achieve better feature extraction. Our detailed progress along these three lines is described below.

MicroDoppler Radar and MicroDoppler Data Collection. We have developed a wideband radar testbed that is fully tunable between 4 to 10 GHz (see Fig. 1). The purpose of this hardware effort is to provide data collection capability that will allow us to study the microDoppler phenomenology in great detail. The radar is a homodyne system with full I/Q detection. Data acquisition is accomplished using a National Instruments DAQ card and the results can be displayed on a laptop computer. Careful calibration of the radar was carried out using tuning forks and an audio speaker.

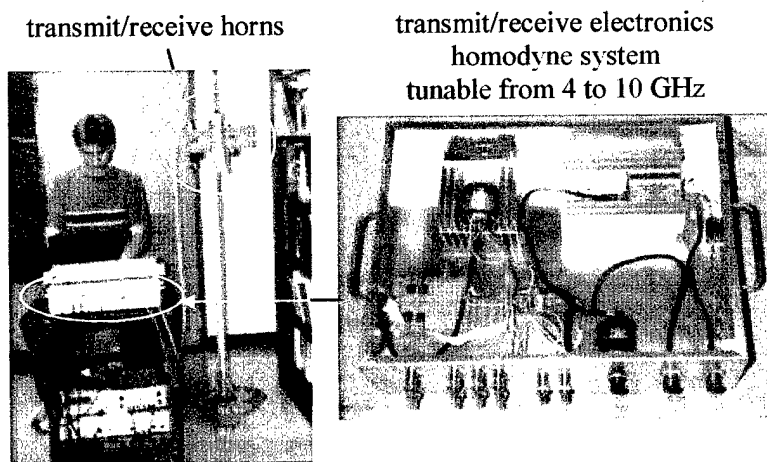


Fig. 1. A low-cost Doppler radar system built at UT-Austin. The radar is tunable from 4 to 10 GHz.

Preliminary data collection of walking humans was carried out in an indoor, high-clutter environment (see Fig 2). The microDoppler phenomenon from human gait was previously investigated by Geisheimer et al. [1, 2]. It was shown that a number of interesting microDoppler features from a walking person can be observed using the spectrogram. A similar analysis was also carried out by processing the data collected from Navy's APY-6 radar of a person walking [3]. However, much work is needed to gain a more complete phenomenological understanding of the detailed features associated with human movements in a wide variety of scenarios.

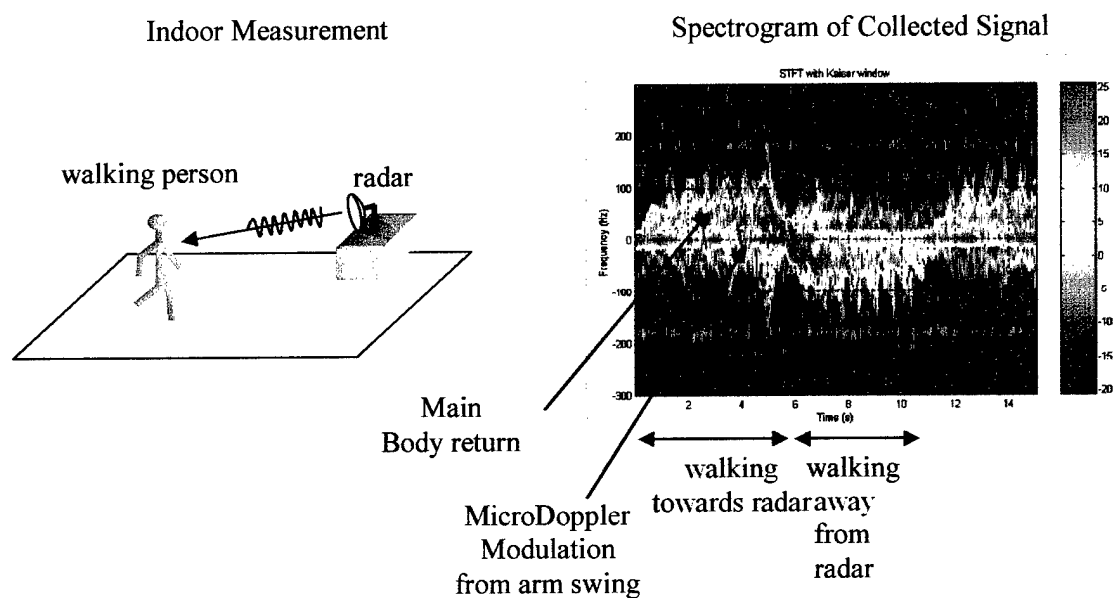


Fig. 2. MicroDoppler features observed in the measured data of a walking person collected using the radar shown in Fig. 1.

We have carried out some preliminary feature extraction effort using the joint time-frequency (JTF) processing tools that we have developed previously under ONR sponsorship. Fig. 3 shows the use of chirplet bases to achieve signal separation of the human gait data. The different (dwell time)-(Doppler frequency) behaviors from various body movements were exploited to separate out the individual microDoppler features.

In the coming year, we plan to carry out extensive data collection over a wide variety of parameter spaces, include various types of movements (walking, running, crawling, and involuntary motions such as respiration), different environments (indoor,

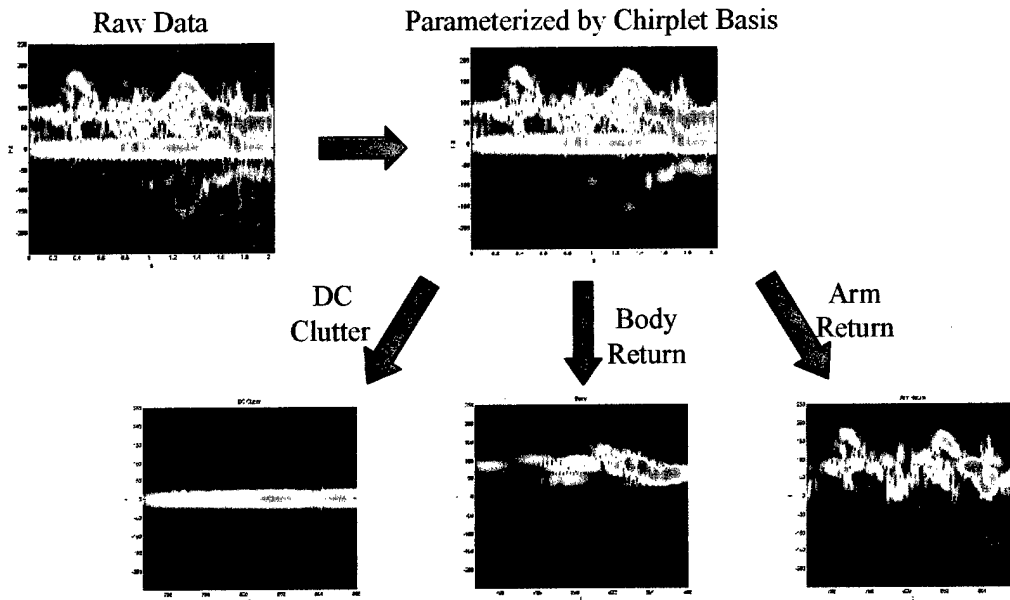


Fig. 3. Feature extraction of the measured walking data using joint time-frequency signal processing. The raw data are parameterized using the adaptive chirplet decomposition, and the different features are extracted based on the chirplet parameters.

outdoor urban, through-wall, occluded by foliage, underground facilities), over a wide range of frequencies, and for different human subjects. We will investigate the use of improved basis sets derived from the actual physics of human movements for feature extraction. As this research matures, we expect to build up a comprehensive dictionary of microDoppler features, from which feature extraction and automatic classification algorithms can be successfully developed.

Ray Tracing Simulation. We have initiated research to develop efficient simulation tools to aid in the interpretation and understanding of microDoppler and multiple scattering phenomena in complex targets. Our simulation methodology is based on the shooting and bouncing ray (SBR) technique. The simulation of radar returns from non-rigid targets is extremely computationally intensive based on SBR. Therefore, we have devoted our efforts to explore ways to speed up the ray tracing time.

The Binary Space Partition (BSP) tree algorithm [4] is the most standard ray tracer in use. In the algorithm, a BSP tree is first built based on the facet model of the

target by recursively cutting the bounding box of the object along a spatial plane. Ray tracing is then performed by traversing the BSP tree. The BSP-tree based ray tracer is considered the fastest among all of the spatial subdivision approaches. Recently, the multiplaten z-buffer ray-tracing algorithm was proposed by Hu et al [5, 6] as an alternative to the traditional BSP tree algorithm. In the multiplaten z-buffer (MPZ) approach, a multi-layered z-buffer is first generated from the scan conversion process (Fig. 4(a)). Instead of just storing the z-coordinates of the visible pixels as in the traditional z-buffer process, multiple z-buffers are created to store the z-coordinates of all of the facets within each pixel during the scan conversion. During the ray trace, a ray is tracked by moving along the ray direction pixel-by-pixel. Within every pixel, the z-depth of the ray is compared to all of the z-buffer values for that pixel to check for possible intersections (Fig. 4(b)). Once an intersection is found, the hit point and the reflection direction can be calculated, and the tracing process is then iterated until the ray departs from the bounding box. We have evaluated the computation time performance of the MPZ ray tracer against that of the BSP tree-based algorithm. Results for a wide range of targets have been tested to determine the computational as well as memory complexity as functions of the number of facets and the complexity of the target. We found that, contrary to the BSP algorithm, the complexity of the MPZ is independent of the number of facets comprising the target (see Fig. 5). However, the computation time is dependent on the number of pixels traversed by a ray.

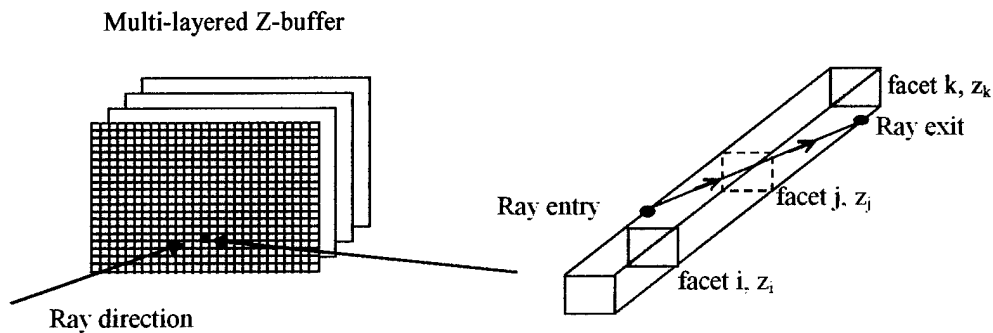


Fig. 4. (a) Multi-layered z-buffer. (b) Ray tracing using the multilayered z-buffer.

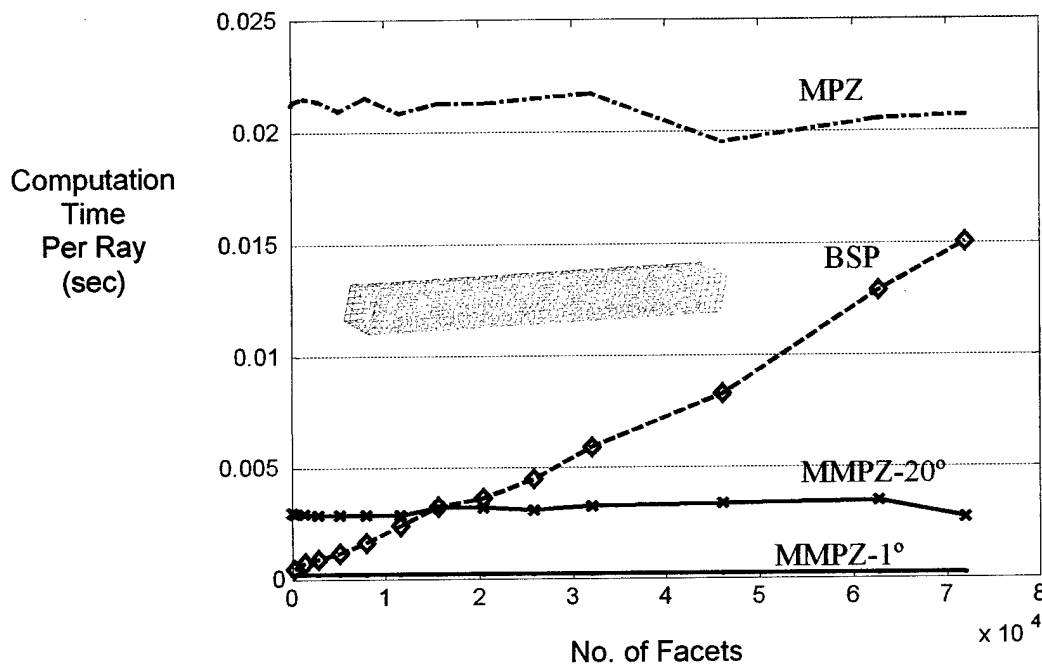


Fig. 5. Computational time of the various ray-tracing algorithms versus the number of facets comprising a test cavity. (a) Binary Space Partition (BSP) tree. (b) Multi-platen z-buffer (MPZ). (c) Multi-aspect MPZ (MMPZ) with a z-buffer every 20° . (d) Multi-aspect MPZ with a z-buffer every 1° .

To further speed up the performance of MPZ algorithm, we are investigating a multi-aspect MPZ approach. The approach is motivated by the fact that the number of pixels a ray traverses between bounces can be reduced dramatically by decreasing the angle between the ray direction and the z-buffer direction. In the algorithm, multiple multi-layered z-buffers are first generated from the scan conversion process along many aspect angles. The maximum number of multi-layered z-buffers is limited only by the available memory resource. The more aspect angles that be stored, the less pixels a ray traverses in one bounce, and the better the time performance. During the ray trace, the multi-layered z-buffer structure that has the closest aspect to the ray direction is selected to carry out the ray tracing. A ray is then tracked by moving along the ray direction inside this MPZ structure pixel-by-pixel to check for possible intersections. Once an intersection is found, the hit point and the reflection direction are calculated. Based on the new ray direction, a new MPZ is chosen, and the tracing process is iterated until the ray departs

from the bounding box. As can be seen in Fig. 5, a dramatic improvement of performance against that of the single-aspect MPZ can be achieved. We are currently investigating the possibility of implementing this algorithm as a real-time tool to simulate scattering from complex targets.

Exploratory Research on Inverse Scattering and Time-Reversal Imaging. We have carried out some exploratory research into the topics of inverse scattering and time-reversal imaging. It is well recognized that traditional imaging algorithms suffer from resolution limitation and image artifacts due to multiple scattering phenomena. Rigorously solving the electromagnetic inverse scattering problem, on the other hand, is much more challenging. In our previous research on inverse scattering, we applied a genetic algorithm (GA) together with a computational electromagnetics solver to attack the two-dimensional inverse scattering problem [7]. The inversion was cast into an optimization problem whereby the difference between the measured fields and the computed fields from a forward electromagnetic solver was minimized. We found that while GA was well suited in searching for the global optimum, it suffered from slow convergence. Since the evolutionary process for the standard GA to reach a cost minimum is in general very slow in comparison to a local search algorithm, a natural improvement to speed up the simple GA is to hybridize the simple GA with a local search. While this hybrid GA (HGA) shows improvements in performance, it also leads to some inefficiency. As the parent selection scheme of GA gives priority to the best members, it usually leads to a population that is highly clustered around the local minima. This clustering is necessary for the simple GA to evolve closer to the exact minimum. For HGA, however, since the local minima have been completely explored by the local search, such clustering will lead to the re-exploration of these regions, which is quite wasteful. In our research, we have proposed a technique combining HGA with the tabu list concept to increase the efficiency of the HGA. The idea was motivated by the Tabu Search (TS) algorithm used in combinatorial problems [8, 9]. The tabu list is adopted to exclude those regions in the parameter space that have already been explored by the local search. In this manner, there will be no revisiting of the explored regions and the GA population can be spread out to explore new regions, thus improving the search

efficiency. We have applied this algorithm to the electromagnetic inverse problem of shape reconstruction of metallic cavity structures containing strong multiple scattering effects. The algorithm has been applied to reconstruct the shape of a metallic cavity based on the measured Ipswich data [10]. Fig. 6 shows that the inversion results from the HGA-Tabu converge faster and at higher success rate than those of the simple GA and hybrid GA. The algorithm could potentially be useful in other optimization/inverse problems.

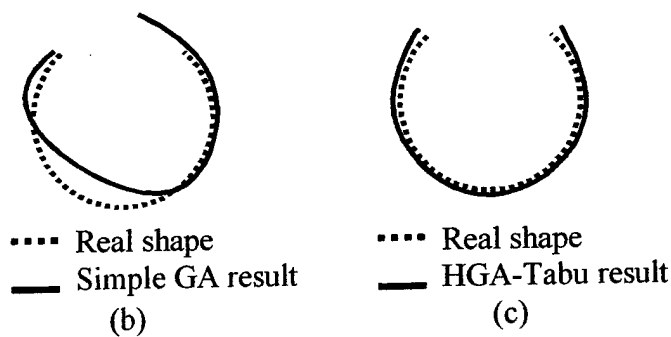
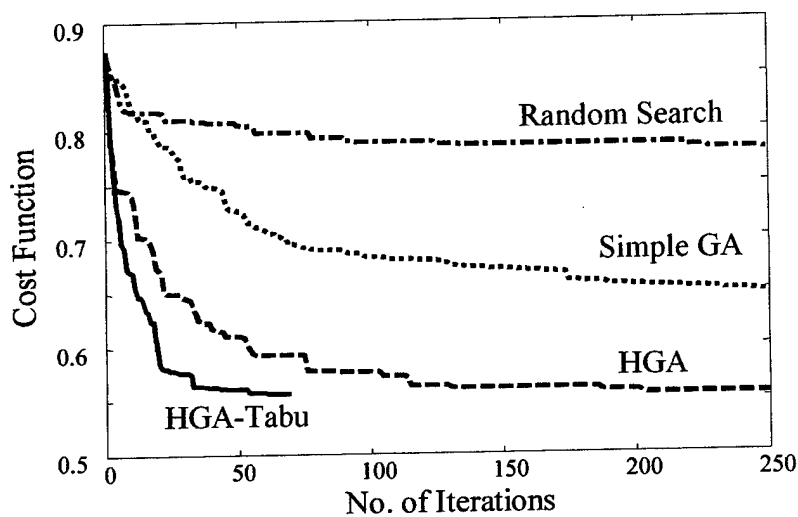
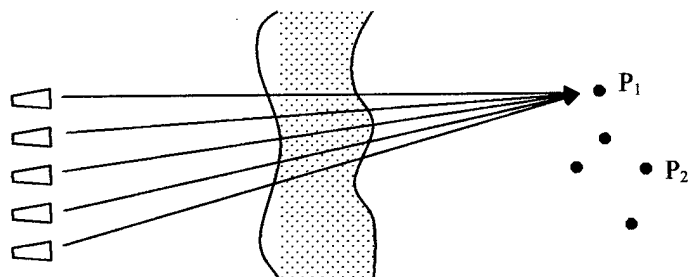


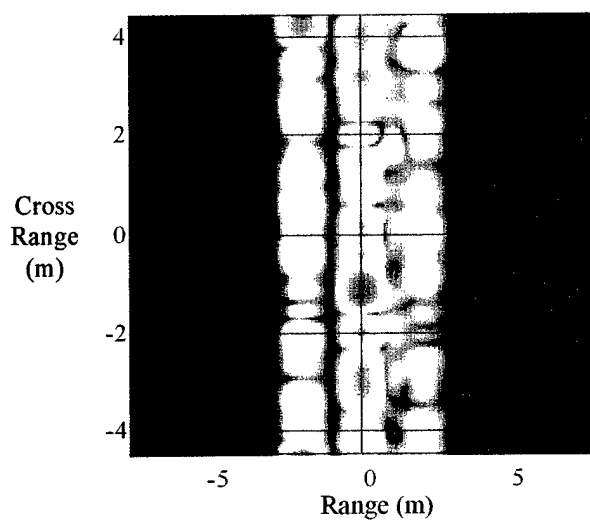
Fig. 6. (a) Convergence comparison for the shape inversion of a metallic cavity for random search, simple GA, hybrid GA (HGA) and HGA-Tabu. The HGA-Tabu shows the best convergence. (b) Typical inverted shape based on measured data by simple GA. (c) Typical inverted shape by HGA-Tabu.

Finally, we have initiated some exploratory research into the concept of time reversal imaging. In the past decade, time reversal methods have been extensively investigated in the acoustics and mathematics communities [11-14]. The original motivation of time reversal was to achieve lithotripsy by focusing the acoustic field from a near-field, physical array on a prescribed focal point through a complex propagation medium. This was accomplished by applying the time reversal operation (or phase conjugation in frequency) to a pilot signal sent out by the array. It was demonstrated theoretically and experimentally that the fields from the array could be focused at a prescribed point through a complex propagation medium. Thus, it is potentially an attractive means of overcoming medium distortion and clutter in radar imaging of occluded targets. However, there are major gaps between what has been achieved in acoustics and what needs to be developed for radar sensors to achieve high-resolution radar imaging. First, it has not been demonstrated to date that being able to focus on a point scatterer can translate directly into good imaging performance without additional information about the medium. Nor is it clear that any proposed algorithms can perform effectively in realistic radar clutter such as foliage or walls. Second, existing time reversal methods require the collection of array calibration data in the bistatic scenario involving a real physical array. Realistic radar imaging sensors, on the other hand, operate in the monostatic, synthetic aperture mode. Finally, contrary to the scalar wave case considered in acoustics, electromagnetic polarization is a new dimension that should be exploited in time reversal imaging for clutter rejection.

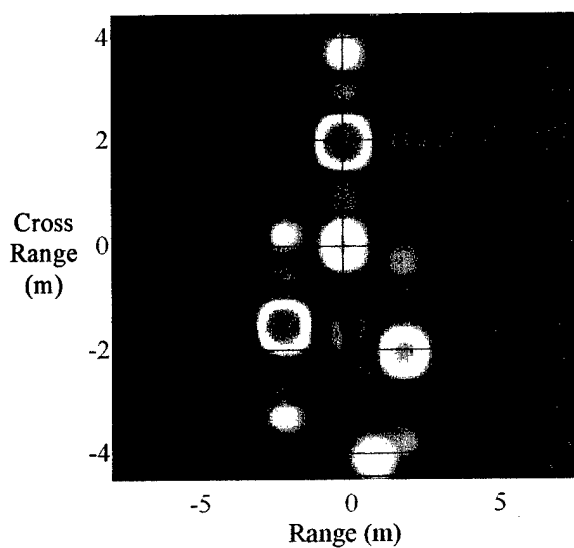
In our preliminary research, we address the case when the medium is unknown, yet a set of "calibration targets" with known positions is located in the vicinity of the target to be imaged. This means that once we can focus the wave on the calibration target using time reversal, it is possible to extract useful information about the propagation distortion caused by the clutter. Fig. 7(a) shows the scenario considered. We use point scatterer testing and assume that the medium distortion is described by a random phase function Φ that is uniformly distributed between $[0, 2\pi]$ and uncorrelated between paths. Fig. 7(b) shows the results of applying conventional free-space imaging to the data. The smearing in the cross range is severe. Next, we apply a subspace-based time reversal algorithm [12] to the data and focus the wave onto a calibration point (x_0, y_0) . After the



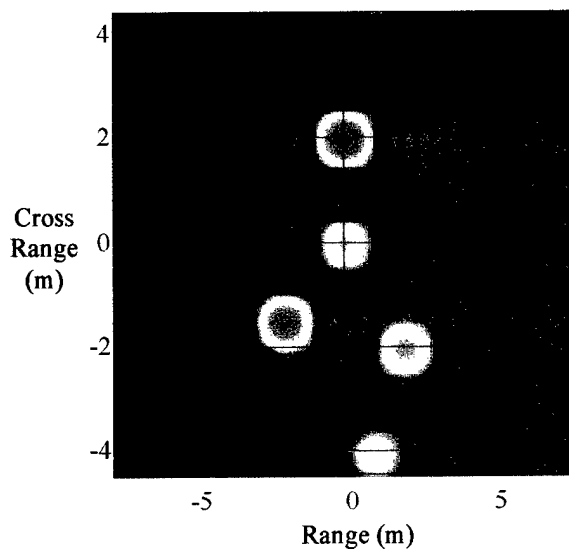
(a) Medium with random phase fluctuation between $[0, 2\pi]$.



(b) Applying free-space imaging to the resulting radar data.



(c) Applying time reversal imaging with a known calibration point.



(d) Reference clutter-free image.

Fig. 7. Results of time reversal imaging by focusing on a calibration point.

time reversal process, the synthesized receive fields on the array elements are:

$$E^r(k_x, k_y) = e^{-j(k_x x_0 + k_y y_0)} e^{-j\Phi} \quad (1)$$

where k_x and k_y are related to the array element position and radar frequency. Since (x_0, y_0) are known, we can now remove the propagation effect and construct the image. The result is shown in Fig. 7(c). Fig. 7(d) shows the reference image in the absence of any clutter. As we can see, the time reversal processing with calibration nearly recovers the clutter-free image. The minor "ghosts" are believed to be due to the assumption that the eigenvector chosen corresponds only to the calibration point. This deficiency can be circumvented by carrying out a MUSIC-like procedure using null-space processing [15]. There are many open questions still yet to be addressed theoretically, and much more research is needed to make this concept a practical radar algorithm.

C. FOLLOW-UP STATEMENT:

During the coming year, our research will be devoted to three fronts. First, we will utilize our microDoppler radar testbed to carry out extensive data collection. Various scenarios will be considered, including types of movements, different environments, over a wide range of frequencies, and for different targets. Second, we will apply simulation and signal processing tools for the extraction and interpretation of scattering phenomenology in the measured data. Third, we will leverage upon the measured database to develop classification algorithms to distinguish different classes of targets to achieve automatic recognition. The potential impacts of this basic research program on naval radar surveillance capabilities are twofold. First, through simulation, measurement and signal processing, this research will result in an in-depth understanding of the radar features due to target micro-dynamics and multiple scattering physics. Second, our research will lead to novel exploitation of target features that can significantly improve the non-cooperative target recognition (NCTR) capabilities for existing and future naval radar sensors.

D. REFERENCES:

1. J. L. Geisheimer, E. F. Greneker and W. S. Marshall, "High-resolution Doppler model of the human gait," *SPIE Proc., Radar Sensor Technology and Data Visualization*, vol. 4744, pp. 8-18, July 2002.
2. J. L. Geisheimer, W. S. Marshall and E. Greneker, "A continuous-wave (CW) radar for gait analysis," *Proc. IEEE Asilomar Conf. Signal Syst. Comp.*, pp. 4-7, Nov. 2001.
3. V. C. Chen, "Analysis of radar micro-Doppler with time-frequency transform," *Proc. of the 10th IEEE Workshop on Statistical Signal and Array Processing*, pp. 463-466, Pocono Manor, PA, Aug. 2000.
4. K. Sung and P. Shirley, "Ray tracing with the BSP tree," *Graphics GEMS IV*, edited by Kirk, D., Academic Press, 1992, pp. 271-274.
5. J. L. Hu, Y. Ma, S. M. Lin and W. B. Wang, "Multiplaten Z-buffer algorithm and its application to multiple scattering," *Electron. Lett.*, vol. 33, pp. 825-826, 1997.
6. J. L. Hu, C. H. Chan and S. M. Lin, "Computation of RCS of jet engine with complex terminations based on multiplaten Z-buffer algorithm," *Microwave Optical Tech. Lett.*, vol. 23, pp. 281-284, Dec. 1999.
7. Y. Zhou and H. Ling, "Electromagnetic inversion of Ipswich objects with the use of the genetic algorithm," *Microwave Optical Tech. Lett.*, vol. 33, pp. 457-459, June 2002.
8. F. Glover, "Tabu search-part I," *ORSA Journal on Computing*, vol. 1, pp. 190-206, 1989.
9. F. Glover and M. Laguna, *Tabu Search: Modern Heuristic Techniques for Combinatorial Problems*, Blackwell Scientific Publication, Oxford, 1993.
10. R. V. McGahan and R. E. Kleinman, "Second annual special session on image reconstruction using real data," *IEEE Antennas Propagat. Mag.*, vol. 39, pp. 7-9, Apr. 1997.
11. M. Fink, "Time-reverse mirrors," *J. Phy. D: Appl. Phys.*, vol. 26, pp. 1333-1350, 1993.
12. C. Prada, S. Manneville, D. Spoliansky and M. Fink, "Decomposition of the time reversal operator: detection and selective focusing on two scatterers," *J. Acoust. Soc. Am.*, vol. 99, pp. 2067-2076, 1996.
13. P. Blomgren, G. Papanicolaou and H.-K. Zhao, "Superresolution in time reversal acoustics," *J. Acoust. Soc. Am.*, vol. 111, pp. 230-248, 2002.

14. L. Borcea, G. Papanicolaou, C. Tsogka and J. Berryman, "Imaging and time reversal in random media," *Inverse Problems*, vol. 18, pp. 1247-1279, 2002.
15. H. Lev-Ari and A. J. Devaney, "The time-reversal technique re-interpreted: subspace-based signal processing for multi-static target location," *Proc. Sensor Array Multichannel Signal Proc. Workshop*, pp. 509-513, 2000.

E. PUBLICATIONS:

I. LIST OF JOURNAL ARTICLES (ONR supported in whole or in part)

1. J. Li, H. Ling and V. C. Chen, "An algorithm to detect the presence of 3D target motion from ISAR data," *Multidimensional Systems and Signal Processing*, special issue on Radar Signal Processing and Its Applications, vol. 14, pp. 223-240, January-July 2003.
2. J. Li and H. Ling, "Use of genetic algorithms in ISAR imaging of targets with higher order motions," *IEEE Trans. Aerospace Electronic Syst.*, vol. AES-39, pp. 343-351, January 2003.
3. Y. Zhou, J. Li and H. Ling, "Shape inversion of metallic cavities using a hybrid genetic algorithm combined with a tabu list," *Elect. Lett.*, vol. 39, pp. 280-281, February 2003.
4. J. Li, Y. Zhou and H. Ling, "Sparse parameterization of electromagnetic scattering data using a genetic algorithm with adaptive feeding," *Elect. Lett.*, vol. 39, pp. 1104-1105, July 2003.
5. J. Li and H. Ling, "ISAR feature extraction from non-rigid body targets using adaptive chirplet signal representation," *IEE Proc. - Radar, Sonar and Navigation*, special issue on time-frequency analysis for synthetic aperture radar and feature extraction, vol. 150, pp. 284-291, August 2003.
6. C. Ozdemir, S. Lim and H. Ling, "A synthetic aperture algorithm for ground-penetrating radar imaging," submitted for publication in *Microwave Opt. Tech. Lett.*, November 2003.

II. LIST OF CONFERENCE PROCEEDINGS (ONR supported in whole or in part)

7. Y. Zhou and H. Ling, "Evaluation of the multiplaten z-buffer algorithm for electromagnetic ray tracing in high-frequency electromagnetic scattering computations," *URSI National Radio Science Meeting*, p. 471, Columbus, OH, June 2003.

8. H. Ling and Y. Wang, "A revisit of random arrays and some recent applications," URSI National Radio Science Meeting, p. 160, Columbus, OH, June 2003.
9. C. Ozdemir, S. Lim and H. Ling, "An algorithm for ground penetration imaging using synthetic aperture radar concept," accepted for presentation in URSI International Union of Radio Science General Assembly, Pisa, Italy, May 2004.
10. Y. Zhou and H. Ling, "A multi-aspect z-buffer algorithm for ray tracing in high-frequency electromagnetic scattering computations," submitted for presentation in URSI National Radio Science Meeting, Monterey, CA, June 2004.

III. LIST OF RELATED PRESENTATIONS

11. "Scattering from periodic surfaces – analysis, design and optimization," Lockheed Fort Worth Company, Fort Worth, Texas, January 10, 2003.
12. "Electromagnetics research at the University of Texas," Motorola Wireless Systems Group, Austin, TX, February 27, 2003.
13. "Nevada Test Site measurement campaign," DARPA Unattended Ground Sensor Program Review, Austin, TX, May 2, 2003.
14. "Antenna miniaturization via genetic algorithms," Motorola Antenna Workshop, Net meeting, June 17, 2003.
15. "Cross flux and scattering center research," Air Force Research Lab, Wright-Patterson Air Force Base, Ohio, August 27, 2003.
16. "Recent research on Xpatch at the University of Texas," AFOSR High Frequency Workshop, Dayton, Ohio, August 28, 2003.

IV. LIST OF THESES AND DISSERTATIONS

None.

V. CONTRACTS AND GRANTS

H. Ling, "Application of model-based signal processing and genetic algorithms for shipboard antenna design, placement and optimization," Office of Naval Research, December 1, 2000 - November 30, 2002.

H. Ling, "Exploitation of microDoppler and multiple scattering phenomena for radar target recognition," Office of Naval Research, October 1, 2002 - September 30, 2005.

R. L. Rogers and H. Ling, "Extended line-of-sight communications for unattended ground sensors," DARPA, October 1, 2002 - May 31, 2004.

H. Ling, "Dynamic signature exploitation," Air Force Research Lab (via SAIC), June 1, 2003 - May 31, 2004.

H. Ling and D. Tanner, "A passive radar sensor exploiting existing wireless infrastructures," Texas Advanced Technology Program, January 1, 2004 - December 31, 2005.

H. Ling, "Wideband wireless channel sounder for multiple antenna channel measurements and estimations," Research Grant, Univ. of Texas, December 4, 2003 - August 31, 2004.

F. INTERACTIONS/COLLABORATIONS WITH OTHER SCIENTISTS:

During the reporting grant period, we hosted Professor Caner Ozdemir of Mersin University, Turkey as a visiting professor under the NATO B-2 Fellowship. Professor Ozdemir spent three months in the summer of 2003 at the University of Texas. He carried out research with our group in ground penetrating radar imaging. Both simulation and measurements were carried out at our facility. Some initial results of this work have been reported in [6] and [9]. Further collaborative research is being carried out between Professor Ozdemir and our group since his return to Turkey.

We have also interacted closely with Dr. Charles Liang of the Joint Strike Fighter program at Lockheed Martin Aeronautics Company in Fort Worth, TX on scattering from inlet ducts. Extensive validation of our simulation tools were carried out against wideband measured data from Lockheed. We are exploring the potential of developing an RCS diagnostic tool for finding "hot spots" in an inlet structure for signature reduction applications.

The PI, together with Dr. Victor Chen of Naval Research Laboratory and Bill Miceli of ONR, guest-edited a special issue of the *IEE Proceedings* on time-frequency analysis for synthetic aperture radar and feature extraction.

G. NEW DISCOVERIES, INVENTIONS, OR PATENT DISCLOSURES:

None.

H. HONORS AND AWARDS:

Mr. Hosung Choo, a graduate research assistant in our laboratory, received first place at the student paper competition at the 2003 URSI National Radio Science Meeting held in Columbus, Ohio in June 2003.

APPENDIX

Publications Supported by ONR

Research Grant N00014-03-1-0021



An Algorithm to Detect the Presence of 3D Target Motion from ISAR Data

JUNFEI LI

Department of Electrical Engineering, The University of Texas-Pan American, Edinburg, TX 78539

fei@panam.edu

HAO LING

Department of Electrical and Computer Engineering, The University of Texas at Austin, Austin, TX 78712-1084

VICTOR CHEN

Airborne Branch, Naval Research Laboratory, Washington, DC 20375

Received December 1, 2000; Revised December 1, 2000; Accepted August 7, 2001

Abstract. We present an algorithm to detect the presence of 3D target motion from ISAR data. Based on the 3D point scatterer model, we first examine the effect of 3D motion on ISAR imaging. It is shown that existing motion compensation algorithms cannot properly focus targets exhibiting 3D motion during the imaging interval. An algorithm is then derived to blindly detect the degree of 3D target motion from raw radar data. It is based on measuring the linearity of phases between two or more point scatterers on the target. The phase estimation is implemented using the adaptive joint time-frequency technique. Examples are provided to demonstrate the effectiveness of the 3D motion detection algorithm with both simulation and real ISAR data. The detection results are corroborated with the truth motion data from on-board motion sensors and correlated with the resulting ISAR images.

Key Words: radar imaging, motion compensation, 3D motion detection

1. Introduction

High-resolution inverse synthetic aperture radar (ISAR) imaging is regarded as an effective tool in automatic target recognition [1], [2]. Ideally, the desired target motion is uniform rotation without translational motion, under which a two-dimensional (2D) Fourier transform brings the radar data in the (frequency)-(dwell time) domain into the (range)-(Doppler frequency) domain. Otherwise, motion compensation is needed as an intermediate step to form a focused ISAR image.

Since target motion can always be decomposed into translational motion and rotational motion, a typical motion compensation algorithm consists of two steps. First, a point on the target is focused through translational motion compensation. When there is non-uniform rotational motion, other points on the target are not necessarily focused. Rotational motion compensation is then applied to focus these other points. Existing motion compensation algorithms usually assume that the rotational motion of a target is confined to a 2D plane during the dwell duration [1], [2], [3], [4], [5], [6], [7]. We shall use the term *2D motion* to refer to target rotational motion of this type. Under the 2D motion assumption, rotational compensation of a second point on the target will focus

the whole target. When there is *3D motion*, i.e., when the rotational motion is not confined to a 2D plane, rotational compensation of a second point cannot focus the whole target.

Recently, several independent research groups have reported that, for aircraft undergoing fast maneuvers or ships on rough seas, the motion of a target may be highly chaotic and does not always obey the 2D motion model [8], [9], [10]. As a result, the image formed using the standard motion compensation algorithms is blurred. In [8] and [9], the effect of 3D motion on ISAR imaging is discussed. However, target motions are assumed to be known from other auxiliary sensor data that are usually not accessible in real operational environment. In [10], the imaging interval is adaptively chosen based on the resolved target feature in the radar image to overcome the 3D motion issue. It requires sound knowledge of the target under consideration, which is often not known to the end users of ISAR data.

The objective of this paper is to develop an algorithm to detect the presence of 3D motions during the imaging interval from ISAR data. Based on the 3D point scatterer model, we first examine the effect of 3D motion on existing imaging algorithms. We then develop an algorithm to blindly detect the existence of 3D motion. For this purpose, only the estimation of phases of several prominent point scatterers is needed. It can be accomplished by the joint time-frequency analysis [6]. With the detection algorithm, we have the ability to distinguish the time intervals when the target undergoes smooth 2D motion from those containing more chaotic 3D motion. As a result, the good imaging intervals where focused images are more easily formed can be automatically determined.

The paper is organized as follows. First, the ISAR imaging problem is formulated in terms of a point scatterer model in Section 2. In Section 3, the 2D motion assumption in existing motion compensation algorithms is analyzed. We show the reason why 3D motion is a problem for ISAR imaging. Section 4 discusses the 3D motion detection algorithm in detail. Examples from both simulation and measurement data are presented in Section 5. The conclusions are given in the last section.

2. 2D and 3D Motion Models

The standard model used in ISAR processing is the point scatterer model given as

$$E(f, t_D) = \sum_{i=1}^{N_s} \sigma_i(x_i, y_i) \exp \left\{ -j \frac{4\pi f}{c} [r(t_D) + x_i + y_i \varphi(t_D)] \right\} \quad (1)$$

where f is the radar frequency and t_D is the dwell time. The radar echo data $E(f, t_D)$ is in the (frequency)-(dwell time) domain. x and y represent the target range and cross-range positions, respectively. The target consists of N_s point scatterers, with the i^{th} point scatterer depicted by position (x_i, y_i) and strength $\sigma(x_i, y_i)$. The target motion includes both the translational motion described by $r(t_D)$ and the rotational motion

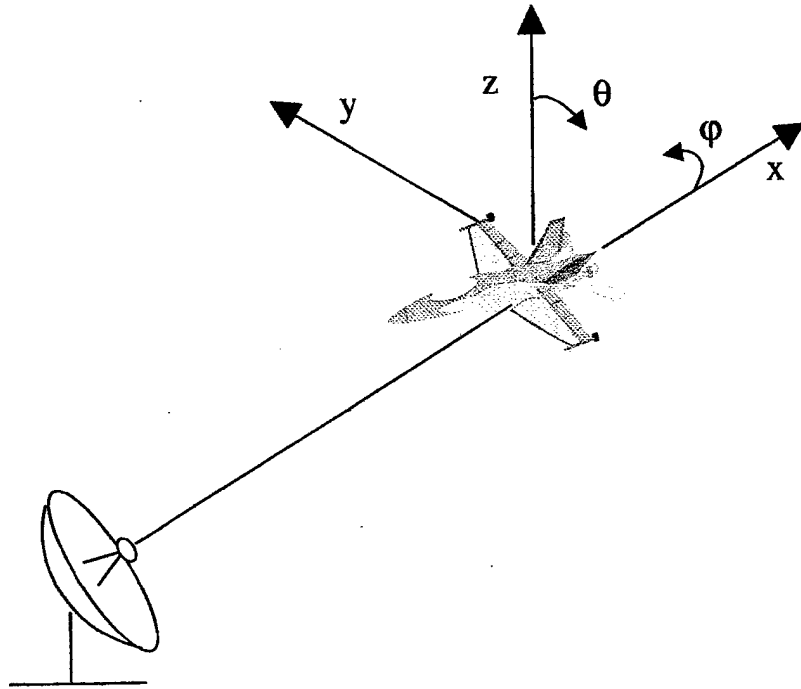


Figure 1. Geometry of an ISAR problem.

described by $\varphi(t_D)$. When there is no translational motion and the rotational motion is uniform, it is seen that a 2D Fourier transform brings the radar data $E(f, t_D)$ into a radar image $\sigma(x, y)$. Otherwise, motion compensation is a critical step in ISAR imaging.

The above model is what we call a 2D problem since the target rotational motion is confined to a 2D plane and describable in terms of only one angular parameter φ . When there is 3D motion of the target, a more general 3D model is required:

$$E(f, t_D) = \sum_{i=1}^{N_s} \sigma_i(x_i, y_i, z_i) \exp \left\{ -j \frac{4\pi f}{c} [r(t_D) + x_i + y_i \varphi(t_D) + z_i \theta(t_D)] \right\}. \quad (2)$$

In the above expression, a third coordinate z of the target is included to represent the 3D target and another independent angular motion parameter θ is introduced to describe the 3D rotational motion (see Figure 1). It is possible to perform 3D target imaging if the target motion is known exactly [11], [12]. In practical ISAR scenarios, however, we have no access to the target motion. Our objectives here are to examine the effect of 3D motion on ISAR imaging and devise an algorithm to detect the

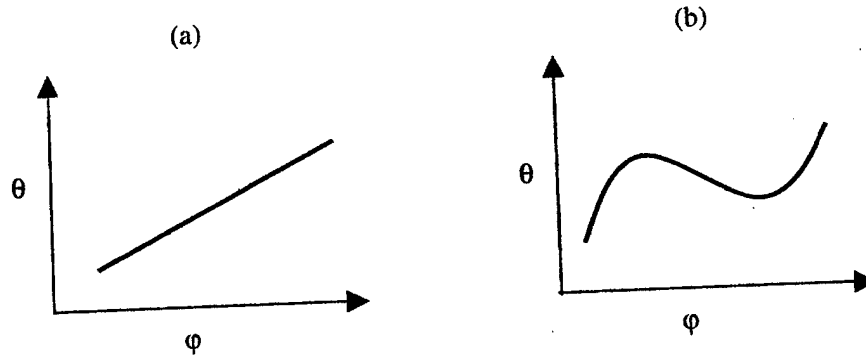


Figure 2. Illustration of 2D motion vs. 3D motion.

presence of 3D motion from the radar data itself, i.e., without any additional knowledge of the target motion.

3. Problem of Existing Motion Compensation Algorithms with 3D Target Motion

First, we show that the more general 3D model degenerates into the 2D model under two conditions. The first case is when there is a linear relationship between ϕ and θ (Figure 2), i.e.,

$$\theta(t_D) = b\phi(t_D). \quad (3)$$

This allows us to cast equation (2) into the form

$$E(f, t_D) = \sum_{i=1}^{N_s} \sigma_i(x_i, y_i, z_i) \exp \left\{ -j \frac{4\pi f}{c} [r(t_D) + x_i + (y_i + bz_i)\phi(t_D)] \right\}. \quad (4)$$

Comparing (4) with (1), we see that if we define $y'_i = y_i + bz_i$, then the rotational motion is in fact a two-dimensional one and the resulting 2D image $\sigma(x_i, y'_i)$ is the projection from the 3D target $\sigma(x_i, y_i, z_i)$ onto the 2D motion plane.

The second case is when the z dimension of the target is so small that the third phase term in (2) can be neglected. For example, suppose a radar operates at a frequency of 10 GHz and the θ variation is limited to 0.5 degree. If the target thickness in the z -dimension is less than 0.2 m, then the third phase term is less than $\pi/4$ and the 2D model is adequate.

From the above consideration, we see that the 2D model is applicable if either the rotational motion is 2D or the target is of 2D in extent. When there exists 3D motion on a full 3D target, any motion compensation algorithms based on the 2D model is not expected to focus the target well. We will now examine this issue in more detail. Since the

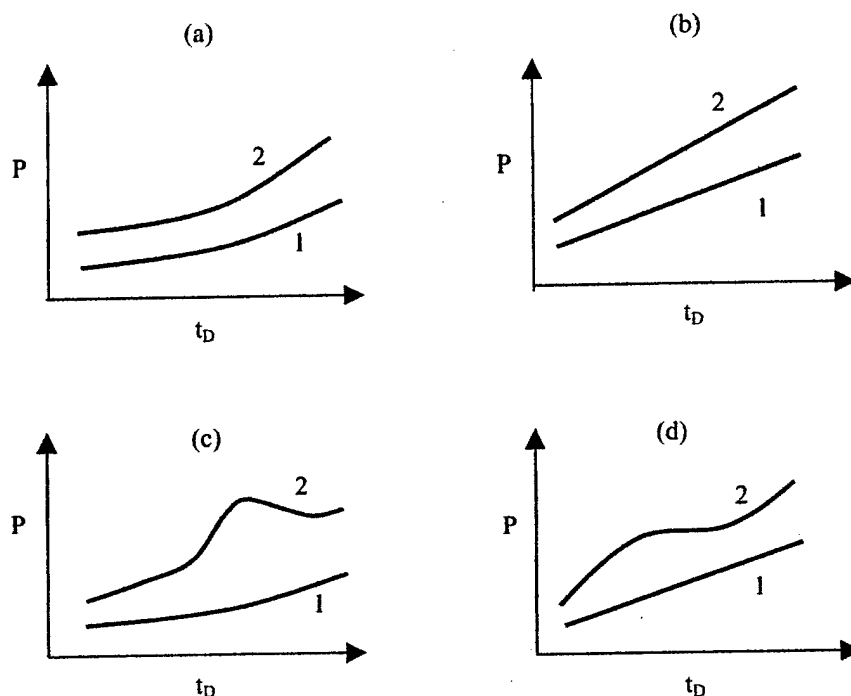


Figure 3. Phase linearization achieved by rotational motion compensation. (a) Phases of two point scatterer with 2D rotational motion. (b) Both phases are linearized with rotational motion compensation. (c) Phases of two point scatterers with 3D motion. (d) Only one phase is linearized with rotational motion compensation.

translational motion compensation is independent of the models in (1) and (2), only the rotational motion compensation needs to be investigated. With 2D rotational motion present, the phase of a point scatterer i due to the rotational motion is

$$P_i(t_D) = y_i \varphi(t_D). \quad (5)$$

Here, the constant $4\pi f/c$ has been suppressed for simplicity. As we can see from (5), the phases of all the point scatterers are linearly related to each other (through the ratio of their cross range positions). If we make one of the phases a linear function of time, then all the phases are linearized simultaneously, and the whole target can be focused after the Fourier transform. This is the basis of most 2D rotational motion compensation algorithms based on the point scatterer model [3], [4], [5], [6]. This concept is illustrated in Figure 3. Figure 3(a) shows the phase functions of two point scatterers under 2D rotational motion. Figure 3(b) shows that both points can be made linear functions of time after we force one of them to be a linear function.

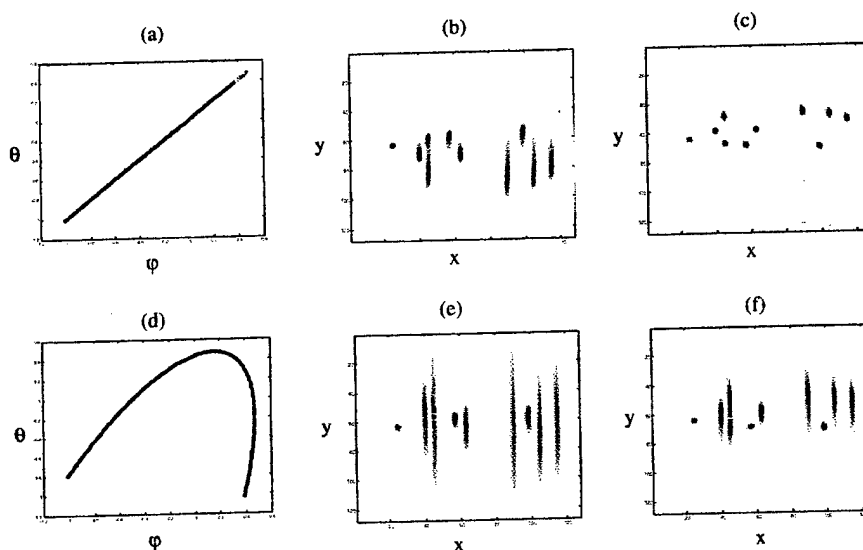


Figure 4. Problem with a typical motion compensation algorithm. (a) Target undergoes a 2D motion. (b) Image after translational motion compensation. (c) Image after rotational motion compensation. (d) Target undergoes a 3D motion. (e) Image after translational motion compensation. (f) Image after rotational compensation.

With 3D motion, the phase of a point scatterer due to the rotational motion is

$$P_i(t_D) = y_i\varphi(t_D) + z_i\theta(t_D). \quad (6)$$

In this case, the phases of the point scatterers are no longer linearly related. If we make one of the phases a linear function of time, the phases of the other point scatterers are not automatically made linear functions of time, as was the case of 2D motion. Figure 3(c) shows the phase functions of two point scatterers with 3D motion. As we can see from Figure 3(d), after one point is forced to be of linear phase, the phase of the other point remains nonlinear.

Figure 4 illustrates some simulation results of the effect of the rotational motion compensation based on the model in (1) on the final images under 2D and 3D target motion. The adaptive joint time-frequency (AJTF) algorithm reported in [6] is used for motion compensation. Ten points in 3D space are used to simulate the radar data. Figure 4(a) shows an assumed 2D rotational motion. Figure 4(b) shows the image after the translational motion compensation. The image shows one point being focused in range cell 25 while other points are unfocused due to the rotational motion. Figure 4(c) shows the image after the 2D rotational motion compensation in which a point scatterer in range cell 57 is selected for focusing. All the point scatterers are focused in the image. The situation with an assumed 3D target motion is shown in Figures 4(d)–4(f).

Figure 4(d) shows the assumed 3D motion. Figure 4(e) shows the image after translational motion compensation. Figure 4(f) shows the final image after the 2D rotational motion compensation. The two points in range cells 25 and 57 are focused, as expected. Another point scatterer in range cell 99 is also focused as it happens to be in the same 2D motion plane as the point scatterer in range cell 57. However, it is not possible to focus all the points simultaneously with an existing algorithm based on the 2D motion model.

4. 3D Motion Detection Algorithm

Since existing motion compensation algorithms cannot handle 3D target motion, it is desirable to develop a general compensation algorithm that can accommodate 3D motion. However, this is a difficult task (see [13] for background on this problem) and outside the scope of this work. Our goal here is to develop an algorithm to detect the presence of 3D motion from radar data. If we can reliably detect those time intervals where 2D target motions are predominant, we can use the existing 2D motion compensation algorithms to form well-focused ISAR images.

As discussed in the last section, 2D motion can be represented by a linear relationship between θ and φ . Therefore, we set out to detect the existence of a nonlinear relationship between θ and φ in our 3D motion detection algorithm. First, we write the relationship between θ and φ into a linear and a nonlinear part as follows:

$$\theta(t_D) = b\varphi(t_D) + m(t_D) \quad (7)$$

where b is the linear constant and $m(t_D)$ is the nonlinear part which indicates deviation from 2D target motion, or the degree of 3D motion. Next we try to gather target motion information by analyzing the phases of two point scatterers on the target. Let us write the relationship between the phase functions P_1 and P_2 of two point scatterers as:

$$P_2(t_D) = aP_1(t_D) + n(t_D). \quad (8)$$

The relationship is again decomposed into the linear part, where a is the linear constant, and the nonlinear part $n(t_D)$. Our goal is to derive a relationship between $m(t_D)$ and $n(t_D)$ so that the presence of m can be detected by observing n .

After the standard translational motion compensation, the time-varying phase of a point scatter is in the form of

$$P_i(t_D) = \Delta y_i \varphi(t_D) + \Delta z_i \theta(t_D) \quad (9)$$

where Δy_i and Δz_i are differential positions of point scatterer i relative to the reference point chosen during translational motion compensation. Substituting (7) into (9) and then

evaluating (9) at point scatterers 1 and 2, we have

$$P_1(t_D) = (\Delta y_1 + b\Delta z_1)\varphi(t_D) + \Delta z_1 m(t_D) \quad (10a)$$

$$P_2(t_D) = (\Delta y_2 + b\Delta z_2)\varphi(t_D) + \Delta z_2 m(t_D). \quad (10b)$$

We next substitute (10) into (8), which leads to

$$a[(\Delta y_1 + b\Delta z_1)\varphi(t_D) + \Delta z_1 m(t_D)] + n(t_D) = (\Delta y_2 + b\Delta z_2)\varphi(t_D) + \Delta z_2 m(t_D) \quad (11)$$

Notice that if there is only 2D motion, then the phases of the two point scatterers must be linear. This means if $m = 0$, then $n = 0$. By using this fact and equating the coefficients of $\varphi(t_D)$ in (11), the constant a can be derived:

$$a = \frac{\Delta y_2 + b\Delta z_2}{\Delta y_1 + b\Delta z_1}. \quad (12)$$

By substituting (12) into (11), we finally arrive at

$$m(t_D) = \frac{\Delta y_1 + b\Delta z_1}{\Delta z_2 \Delta y_1 - \Delta y_2 \Delta z_1} n(t_D). \quad (13)$$

Equation (13) states that once the nonlinear phase term n is known, it is proportional to nonlinear motion m . Therefore, the steps to determine the degree of 3D target motion are as follows. First, we extract the phases of two point scatterers from the radar data. Next we find the nonlinear phase function n using a minimum least squares fit of equation (8). Once n is known, we use equation (13) to decide on the degree of 3D motion. The remaining issues are: (i) how to determine the phase functions of the point scatterers, (ii) how to define the degree of nonlinearity and the degree of 3D motion once n is known, and (iii) how to compare the degree of 3D motion from one imaging interval to another. These three issues are discussed in the following subsections.

4.1. Phase Estimation Using Adaptive Joint Time-Frequency Projection

After the translational motion compensation, the radar signal contains only rotational motion. To estimate the phase of a prominent point scatterer, we utilize the adaptive joint time-frequency (AJTF) projection technique discussed in [6]. We begin with the radar data in the (range)-(dwell time) domain. Within a fixed range cell, the data can be written as

$$E_s(t_D) = \sum_{i=1}^{N_r} \sigma_i \exp\left(-j \frac{4\pi f_c}{c} (y_i \varphi(t_D) + z_i \theta(t_D))\right) \quad (14)$$

where f_c is the center frequency. Among the N_r point scatterers within the range cell,

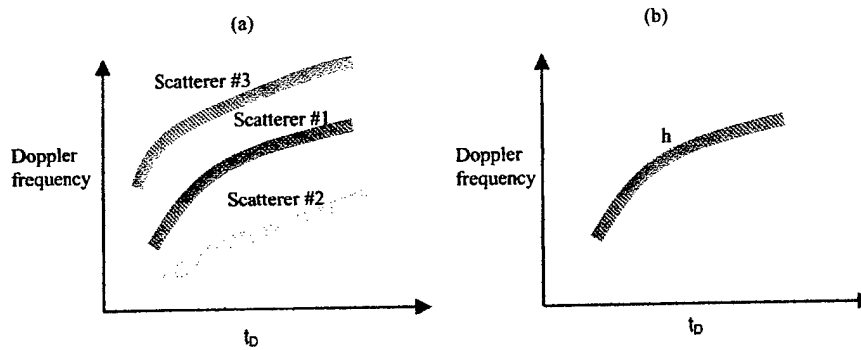


Figure 5. (a) (Dwell time)-(Doppler frequency) representation of radar signal in a range cell with three point scatterers. (b) The basis function that is best matched to the dominant point scatterer is found by the AJTF project method.

we express the phase behavior of the strongest one as a polynomial function:

$$\phi_M(t_D) = (f_1 t + f_2 t^2 + f_3 t^3 + \dots) \quad (15a)$$

and consider

$$h(t) = \exp[-j\phi_M(t_D)] \quad (15b)$$

as a basis for the radar signal. The phase parameters are then found by searching for the maximum projection from the radar signal onto the basis function:

$$\langle f_1, f_2, f_3, \dots \rangle = \arg \max \left| \int E(t_D) h^*(t_D) dt_D \right|. \quad (16)$$

Equation (16) means that the phase function parameters are estimated to give a maximum projection from the radar data onto the basis function for that prominent point scatterer. In the search procedure, the first term f_1 can be obtained by using the fast Fourier transform, while all other higher order terms f_2, f_3, \dots are obtained using exhaustive search. Figure 5 illustrates the process of AJTF phase estimation. Figure 5(a) shows the radar signal in one range cell with three point scatterers in the joint (dwell time)-(Doppler frequency) plane. The tilted trajectory of the prominent point scatterer 1 implies there exist higher-order terms in the phase function. Figure 5(b) shows the basis function $h(t_D)$. During the search, we change the position (f_1), tilting (f_2) and curvature (f_3, \dots) of h until the projection of h onto the radar signal is maximized.

4.2. Measure of Nonlinearity Between Two Phase Functions

We notice that in (8), the two phase functions are formulated with a linear relationship plus a nonlinear residual part. After the two phase functions are estimated using the AJTF technique, a least-squares fitting can be performed to generate the best-fit linear part. The actual

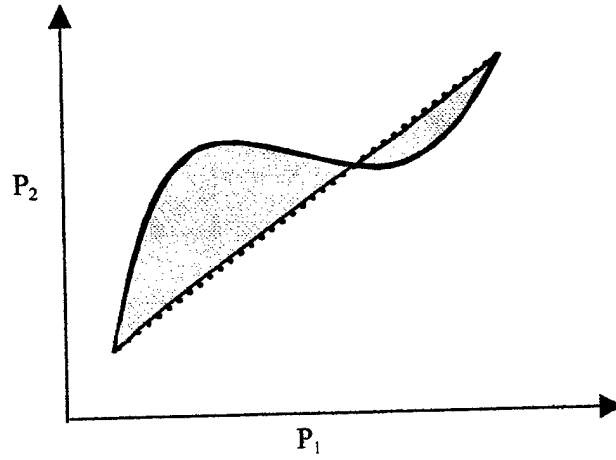


Figure 6. Measure of the nonlinearity of two phase functions.

phases deviates from this linear relationship. The deviation n is integrated over the dwell time to represent the degree of phase nonlinearity over the imaging interval as follows:

$$N_{12} = \int |n_{12}(t_D)| dt_D. \quad (17)$$

The process is illustrated in Figure 6. The solid line is the actual relationship between the two phase functions P_1 and P_2 . The dotted line is the linear approximation of the relationship. The area of the shadowed region is N_{12} .

In a similar fashion, we define the degree of 3D motion as the deviation from a linear relationship between θ and φ over the dwell interval as follows:

$$M = \int |m(t_D)| dt_D. \quad (18)$$

Based on (13), we see that M and N_{12} are directly related:

$$N_{12} = \beta_{12} M \quad (19a)$$

where

$$\beta_{12} = \left| \frac{\Delta z_1 \Delta y_2 - \Delta y_1 \Delta z_2}{\Delta y_1 + b \Delta z_1} \right|. \quad (19b)$$

Thus by finding the observable N_{12} , we can obtain the degree of 3D motion M to within a proportionality constant.

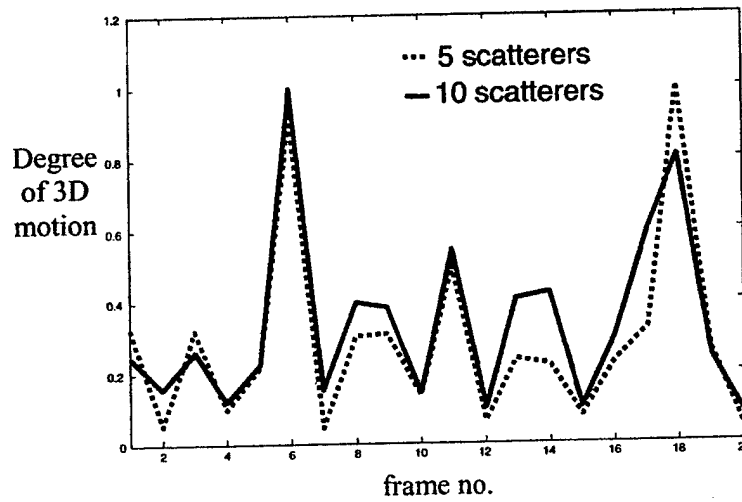


Figure 7. Effect of the number of point scatterers used on 3D motion detection result.

4.3. 3D Motion Comparison among Different Imaging Intervals

As indicated by (19), the phase nonlinearity of two point scatterers N is proportional to the degree of 3D motion M , so we can use the detected phase nonlinearity as a measure of 3D motion. However, we notice that the constant of proportionality is dependent on the point scatterer positions. A problem arises when we need to compare the detection result from one imaging interval to that from another imaging interval. Since we cannot guarantee that we track the same set of points from frame to frame, the proportionality constant can change from frame to frame, and we cannot reliably observe M from N across frames. To overcome this difficulty, we track more than two point scatterers within each frame and compute N_{ij} for each pairing of scatterers i and j ($i \neq j$). Then we generate an average value $\langle N_{ij} \rangle$ from all the possible phase relationships. From (19), we have

$$\langle N_{ij} \rangle = \langle \beta_{ij} \rangle M. \quad (20)$$

We postulate that, from a statistical point of view, $\langle \beta_{ij} \rangle$ approaches a constant that is independent of frames if we average over a sufficient number of point scatterers. If this is true, $\langle N_{ij} \rangle$ should become a good indicator of M .

We test the effectiveness of this approach on the detection result by simulation. We input a set of motion parameters and generate the phase functions based on the 3D motion model. 20 point scatterers from an airplane model is used. We then randomly choose a number of point scatterers and use their phase functions to compute $\langle N_{ij} \rangle$. We examine how the results vary as different number of point scatterers is used. We find that the results begin to converge after about 5 scatterers. Figure 7 shows a plot of $\langle N_{ij} \rangle$ versus the frame number if

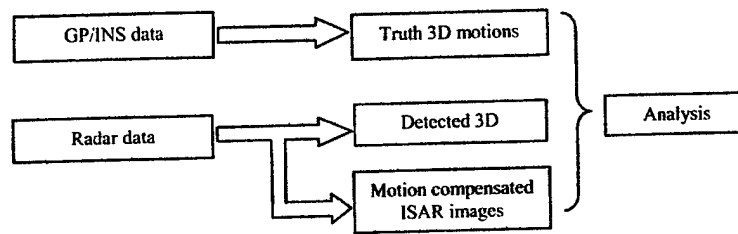


Figure 8. Data processing flow chart.

we use 5 point scatterers (10 phase pairs). If we increase the number of point scatterers to 10 (45 phase pairs), there is only minor change in the detection output. Therefore, $\langle N_{ij} \rangle$ can be used to indicate the degree of 3D motion given a sufficient number of point scatterers.

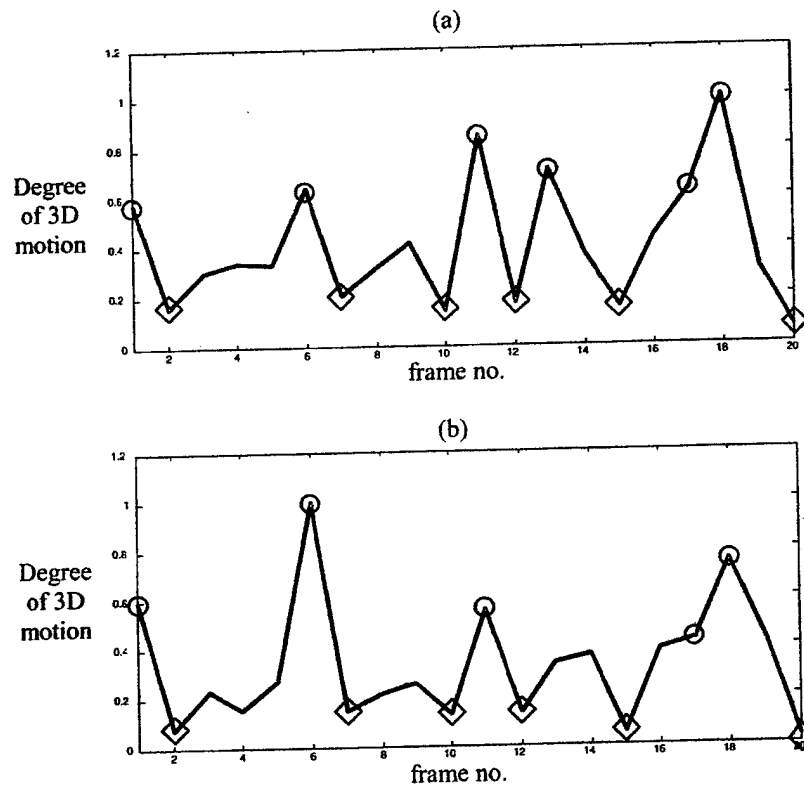


Figure 9. (a) Detected 3D motion from simulated radar data. (b) Degree of 3D motion from truth motion data.

5. Results

To demonstrate the effectiveness of the 3D motion detection algorithm, we test our algorithm on radar data from two targets. The first target is an aircraft, which flew in a large clockwise circle during a 9-minute interval. We also have access to the target motion data through the GPS (global positioning system) and INS (inertial navigation system) sensors carried on-board the aircraft [14]. Figure 8 shows our processing flow chart. The GPS/INS data is used to establish the truth target motion. The raw radar data is used as input to the 3D motion detection algorithm. We can also generate the ISAR images using our AJTF motion compensation algorithm [6]. We are therefore able to both compare the detection result with the truth motion, and observe the effect of the 3D motion on the ISAR image quality.

We first test the 3D motion detection algorithm on simulated radar data. To generate the simulation data, we use the actual motion data from the GPS/INS sensors in conjunction with a point scatterer model. From the aircraft model, 60 point scatterers are selected to simulate the radar data based on the actual motion data and equation (2). Five range cells are then chosen for phase analysis in the detection procedure. Figure 9(a) shows the detected degree of 3D motion for 20 image frames from the simulated radar data. For comparison, Figure 9(b) shows the degree of 3D motion obtained based on the truth motion data. The frames with significant 3D motion are highlighted with circles and the frames with 2D motion are highlighted with diamonds. It is seen that the two results agree fairly well.

Next, we test the detection algorithm using the actual radar measurement data. Figure 10(a) shows the detected 3D motion from the radar data over 20 frames. The corresponding imaging interval for each frame is 2.3 seconds while the total flight duration is 5 minutes. The four frames with the most significant 3D motion based on our detection algorithm are labeled as circles. They are frames 6, 14, 17 and 18. Figure 10(b) shows the degree of 3D motion obtained based on the truth motion data. We observe that the truth motion data indeed contains a high degree of 3D motion at those four frames detected by our algorithm.

To further examine the quality of the ISAR images when 3D motion is present, we generate images using our motion compensation algorithm in Figures 11 to 14. Figure 11(a) shows the plot of θ vs. ϕ derived from the truth motion data for frame 18, which is a frame found to contain substantial 3D motion. The actual motion is shown in the solid curve and the dashed line is the best-fit 2D motion approximation. It is clear that the curve deviates significantly from the dashed line and the actual motion cannot be well approximated with 2D motion. Figure 11(b) shows the resulting image obtained after the motion compensation, and is blurred in the Doppler dimension (vertical axis). As expected, the 2D motion compensation algorithm cannot focus all the points due to the 3D target motion. Figures 12(a) and 12(b) show the same conclusion for frame 14, which is another frame identified as having significant 3D motion. In Figure 13, we show the results for frame 2, which has very little 3D motion. As we can see from Figure 13(a), the actual motion can be well approximated by a line in the θ - ϕ plot. The image shown Figure 13(b) is well focused. In particular, the point scatterers on the target show nearly equal range and Doppler extent, contrary to the previous two images. The aircraft body line is clearly recognizable.

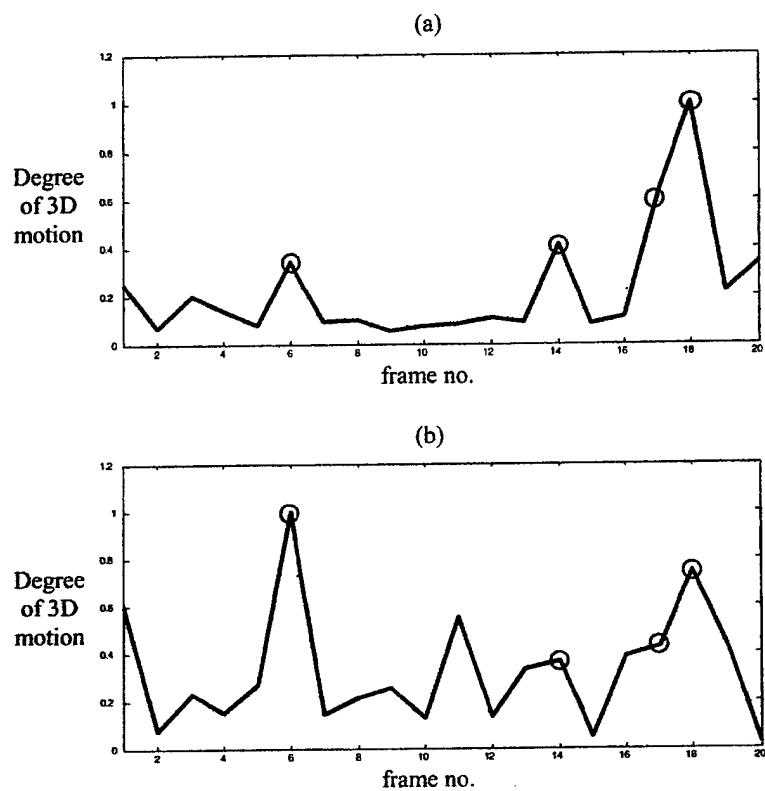


Figure 10. (a) Detected 3D motion from aircraft radar data. (b) Degree of 3D motion from truth motion data.

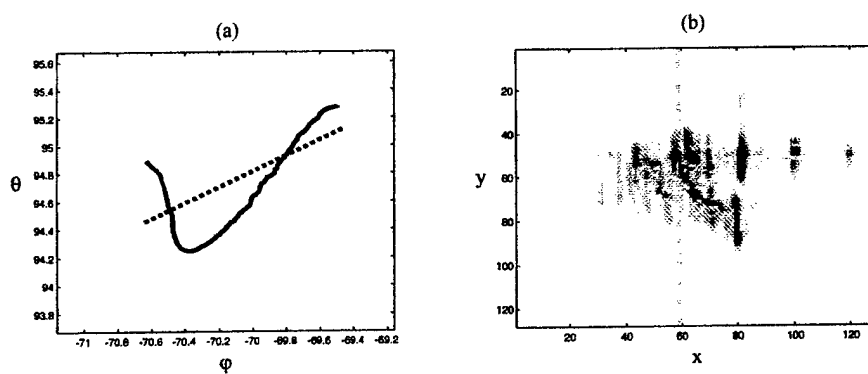


Figure 11. 3D motion and resulting ISAR image (frame 18).

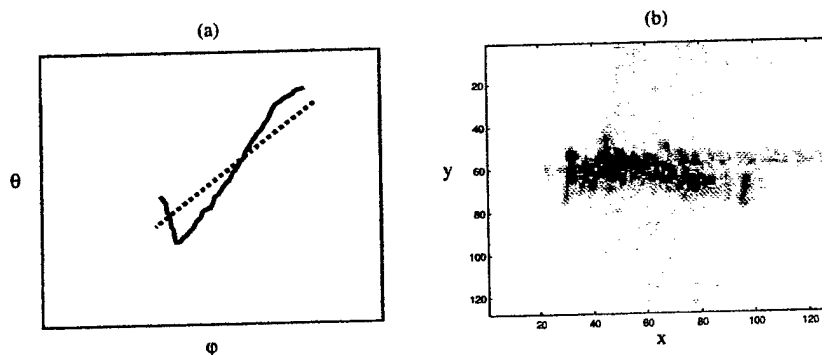


Figure 12. 3D motion and resulting ISAR image (frame 14).

From Figure 10, we notice that there exists a discrepancy in frame 11, where the detection result does not indicate any 3D motion while the truth motion data shows a significant amount of 3D motion. The truth motion is shown in Figure 14(a), confirming the presence of 3D motion. One explanation is that those prominent points used by the detection algorithm lie nearly on a 2D plane so that they still can be focused. As we have discussed in Section 3, the 2D model is applicable if either the motion is 2D or the target is of 2D in extent. It is likely that the latter condition is met for this frame. This is confirmed by the image shown in Figure 14(b). We see that the image quality is actually not so bad. Therefore, our detection algorithm objectively reflects the quality of the images generated by the 2D motion compensation.

A second data set is used to test our 3D motion detection algorithm. This data set consists of the ISAR data collected from a small ship on the ocean. Because of the surface movement of the sea, the target is believed to have considerable 3D motion during the imaging intervals. The 3D motion detection result is shown in Figure 15(a) with the peaks

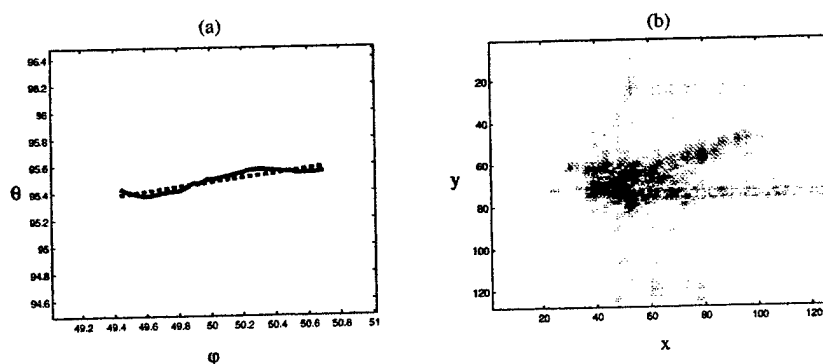


Figure 13. 2D motion and resulting ISAR image (frame 2).

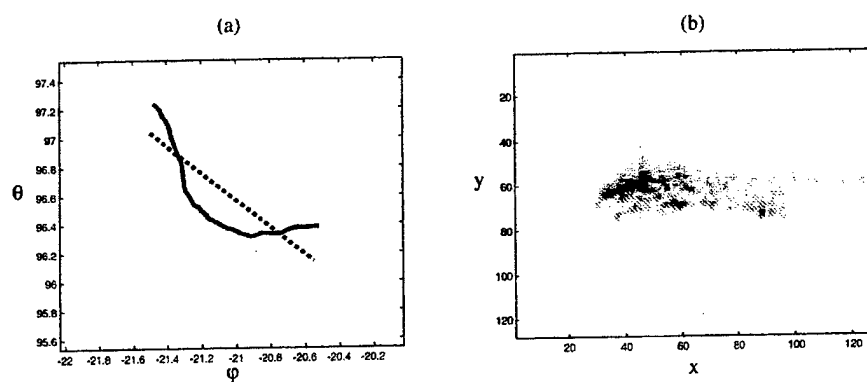


Figure 14. Frame no.11 showing focused ISAR image with 3D motion.

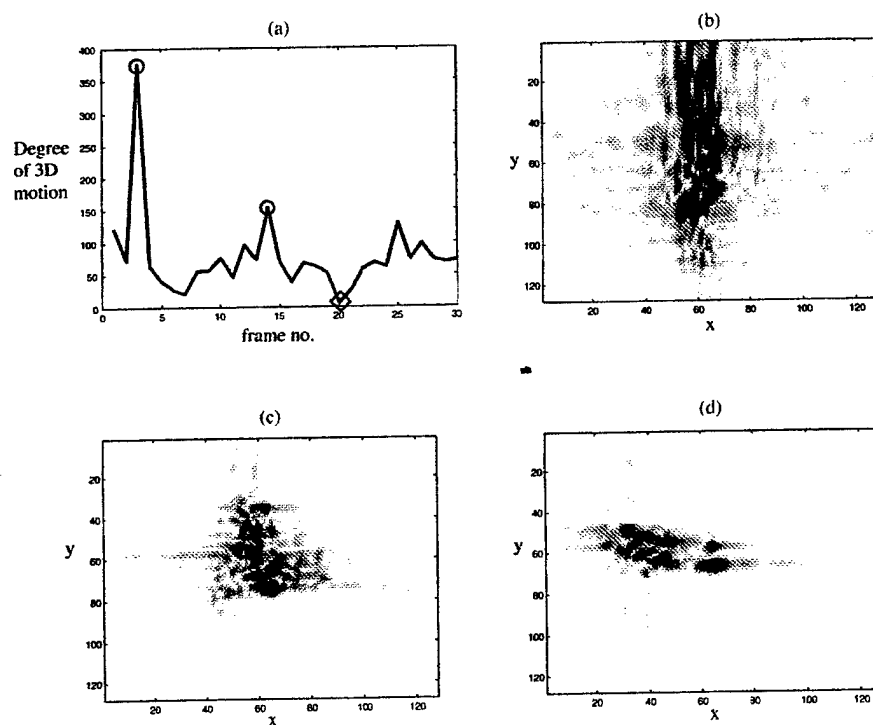


Figure 15. 3D motion detection result from radar data of a ship. (a) Detected 3D motion. (b) ISAR image from frame 3. (c) ISAR image from frame 14. (d) ISAR image from frame 20.

corresponding to regions with 3D motion. The total data duration is 20 seconds and the imaging dwell time is 0.64 second per frame. For this data set, reliable truth target motion is not available. Instead, we generate the motion compensated images shown in Figures 15(b) to 15(d) to demonstrate the effect of 3D motion on ISAR image quality. The image frame with the largest detected 3D motion, frames 3, is shown in Figure 15(b). It is poorly focused. Figure 15(c) shows the image from frame 14, which is the frame with the second highest detected 3D motion. The frame with the smallest 3D motion based on our algorithm, frame 20, is shown in Figure 15(d). It shows a well-focused ISAR image. This test confirms the effectiveness of our algorithm in detecting good imaging intervals from those imaging intervals containing large 3D motion.

6. Conclusions

In this paper, we set out to develop an algorithm to detect the presence of 3D target motion from ISAR data. Based on the 3D point scatterer model, we first examined the effect of 3D motion on ISAR imaging. It was shown that the existing motion compensation algorithms could not properly focus targets exhibiting 3D motion during the imaging interval. We then derived an algorithm to blindly detect the degree of 3D target motion from raw radar data. It is based on measuring the linearity of phases between two or more point scatterers on the target. The phase estimation was implemented using the adaptive joint time-frequency technique. Examples were provided to demonstrate the effectiveness of the 3D motion detection algorithm with both simulation and real ISAR data. The detection results were corroborated with the truth motion data from on-board motion sensors and correlated with the resulting ISAR images. With the detection algorithm, we have the ability to distinguish the time intervals when the target undergoes smooth 2D motion from those containing more chaotic 3D motion. As a result, the good imaging intervals where focused images are more easily formed can be automatically selected.

Acknowledgments

This work is supported by the Office of Naval Research under contract No. N00014-98-1-0615.

References

1. C.C. Chen and H.C. Andrews, "Target Motion Induced Radar Imaging," *IEEE Trans. Aerospace Electron. Syst.*, vol. 16, no. 1, Jan. 1980, pp. 2-14.
2. A. Ausherman, A. Kozma, J.L. Waker, H.M. Jones, and E.C. Poggio, "Developments in Radar Imaging," *IEEE Trans. Aerospace Electron. Syst.*, vol. 20, no. 4, July 1984, pp. 363-400.
3. W.G. Carrara, R.S. Goodman, and R.M. Majewski, *Spotlight Synthetic Aperture Radar - Signal Processing and Algorithms*, Boston, MA: Artech House, 1995.

4. S. Werness, W. Carrara, L. Joyce, and D. Franczak, "Moving Target Imaging Algorithms for SAR Data," *IEEE Trans. Aerospace Electron. Syst.*, vol. 26, no. 1, Jan. 1990, pp. 57-67.
5. D.E. Wahl, P.H. Eichel, D.C. Ghiglia, and C.V. Jakowatz, "Phase Gradient Autofocus- A Robust Tool for High Resolution SAR Phase Correction," *IEEE Trans. Aerospace Electron. Syst.*, vol. 30, no. 3, July 1994, pp. 827-835.
6. Y. Wang, H. Ling, and V.C. Chen, "ISAR Motion Compensation via Adaptive Joint Time-Frequency Techniques," *IEEE Trans. Aerospace Electron. Syst.*, vol. 34, no. 2, Apr. 1998, pp. 670-677.
7. Z. Liu, R. Wu, and J. Li, "Complex ISAR Imaging of Maneuvering Targets via the Capon Estimator," *IEEE Trans. Signal Processing*, vol. 47, no. 5, May 1999, pp. 1262-1271.
8. V.C. Chen and W.J. Miceli, "Effect of Roll, Pitch and Yaw Motions on ISAR Imaging," in *SPIE Proc. Radar Processing, Technology and Applications VI*, vol. 3810, Denver, CO, July 1999, pp. 149-158.
9. J. Li, Y. Wang, R. Bhalla, H. Ling, and V.C. Chen, "Comparison of High-Resolution ISAR Imagery from Measured Data and Synthetic Signatures," *SPIE Proc. Radar Processing, Technology and Applications VI*, vol. 3810, Denver, CO, July 1999, pp. 170-179.
10. A.W. Rihaczek and S.J. Hershkowitz, "Choosing Imaging Intervals for Identification of Small Ships," *SPIE Proc. Radar Processing, Technology and Applications VI*, vol. 3810, Denver, CO, July 1999, pp. 139-148.
11. S. Xiao and D.C. Munson, "Spotlight-Mode SAR Imaging of a Three-Dimensional Scene Using Spectral Estimation Techniques," in *Proc. IEEE Inter. Geosci. and Remote Sensing Symp.*, vol. 2, Seattle, WA, July 1998, pp. 642-644.
12. J.T. Mayhan, M.L. Burrows, K.M. Cuomo, and J.E. Piau, "High Resolution 3D 'Snapshot' ISAR Imaging and Feature Extraction," *IEEE Trans. Aerospace Electron. Syst.*, vol. 37, no. 2, Apr. 2001, pp. 630-641.
13. M.A. Stiff, "Three-Dimensional Analysis of Moving Target Radar Signals: Methods and Implications for ATR and Feature-Aided Tracking," *SPIE Proc. Algorithms for Synthetic Aperture Radar Imagery VI*, vol. 3721, Aug. 1999, pp. 485-496.
14. H. Ling, Y. Wang, J. Li, and R. Bhalla, "ISAR Image Formation of TIRA Data Using Adaptive Joint Time-Frequency Processing," in *NATAO Sensors and Electronics Technology Symposium on High Resolution Radar Techniques*, Granada, Spain, Mar. 1999, pp. 61.1-61.7.

Evaluating at $\mu = \mu_0$ yields

$$p(\mu_0) = \frac{A^2}{T} \int_{-\infty}^{\infty} \left| \int_{-\infty}^{\infty} \text{rect}\left(\frac{t}{T}\right) \text{rect}\left(\frac{t-\tau}{T}\right) dt \right| d\tau = A^2 T,$$

the LFM waveform energy E .

BRIAN K. JENNISON¹
Dept. of Electrical Engineering
and Engineering Science
Loyola College in Maryland
Baltimore, MD

REFERENCES

- [1] Akes, R. A. (1980)
Detection, estimation, and classification with spectrograms.
Journal of the Acoustical Society of America, 67 (Apr. 1980), 1232-1246.
- [2] Friedlander, B., and Porat, B. (1989)
Detection of transient signals by the Gabor representation.
IEEE Transactions on Acoustics, Speech, and Signal Processing, 37 (Feb. 1989), 169-180.
- [3] Hinich, M. J. (1990)
Detecting a transient signal by bispectral analysis.
IEEE Transactions on Acoustics, Speech, and Signal Processing, 38 (July 1990), 1277-1283.
- [4] Fonollosa, J. R., and Nikias, C. L. (1993)
Wigner higher order moment spectra: Definition, properties, computation and application to transient signal analysis.
IEEE Transactions on Signal Processing, 41 (Jan. 1993), 245-266.
- [5] Kay, S., and Boudreaux-Bartels, G. F. (1985)
On the optimality of the Wigner distribution for detection.
In Proceedings of the IEEE International Conference on Acoustics, Speech, and Signal Processing, Mar. 1985.
- [6] Li, W. (1987)
Wigner Distribution method equivalent to dechirp method for detecting a chirp signal.
IEEE Transactions on Acoustics, Speech, and Signal Processing, 35 (Aug. 1987), 1210-1211.
- [7] Wood, J. C., and Barry, D. T. (1994)
Radon transformation of time-frequency distributions for analysis of multicomponent signals.
IEEE Transactions on Signal Processing, 42 (Nov. 1994), 3166-3177.
- [8] Wang, M., Chan, A. K., and Chui, C. K. (1998)
Linear frequency-modulated signal detection using radon-ambiguity transform.
IEEE Transactions on Signal Processing, 46 (Mar. 1998), 571-586.
- [9] Akay, O., and Boudreaux-Bartels, G. F. (2001)
Fractional convolution and correlation via operator methods and an application to detection of linear FM signals.
IEEE Transactions on Signal Processing, 49 (May 2001), 979-993.
- [10] Ozdemir, A. K., and Arikan, O. (2001)
Fast computation of the ambiguity function and the Wigner distribution on arbitrary line segments.
IEEE Transactions on Signal Processing, 49 (Feb. 2001), 381-393.
- [11] Eaves, J. L., and Reedy, E. K. (1987)
Principles of Modern Radar.
New York: Van Nostrand Reinhold, 1987.
- [12] Peebles, P. Z. (1998)
Radar Principles.
New York: Wiley, 1998.
- [13] Lewis, B. L., Kretschmer, F. F., and Shelton, W. W. (1986)
Aspects of Radar Signal Processing.
Norwood, MA: Artech House, 1986.
- [14] Nunn, C. J., and Welch, L. R. (2000)
Multi-parameter local optimization for the design of superior matched filter polyphase pulse compression codes.
In The Record of the IEEE 2000 International Radar Conference, May 2000, 435-440.

Use of Genetic Algorithms in ISAR Imaging of Targets with Higher Order Motions

Genetic algorithms (GA) are proposed for inverse synthetic aperture radar (ISAR) imaging. GA is used for motion parameters search in place of exhaustive search in the adaptive joint time-frequency (AJTF) algorithm. While maintaining the same accuracy, GA has lower computational complexity, especially for targets with higher order motions.

I. INTRODUCTION

An inverse synthetic aperture radar (ISAR) system usually collects radar data from a target moving on the ground, in the air, or over the ocean. In the ISAR problem, the radar is stationary while the target moves with both translation motion and rotational motion. In the microwave frequency range, ISAR has been identified as an effective tool for target identification [1].

Target motion is an essential part in ISAR imaging. On the one hand, target motion is needed to generate Doppler (or cross-range) resolution [2]. On the other hand, unwanted motion causes image blurring. When the target has uniform rotational motion only and the radar data is collected over a small angular aperture, a simple Fourier transform will bring the raw radar data into a two-dimensional ISAR image. However, actual targets observed by operational radar rarely have such an ideal motion. Therefore, motion compensation is needed to generate

Manuscript received October 11, 2001; revised May 24 and September 9, 2002; released for publication October 28, 2002.

IEEE Log No. T-AES/39/1/808686.

Refereeing of this contribution was handled by L. M. Kaplan.

This work is supported by the Office of Naval Research under Contract N00014-98-1-0615.

¹Now with Johns Hopkins University, Applied Physics Laboratory, MS 8-250, 11100 Johns Hopkins Rd., Laurel, MD 20723-6099.

focused ISAR imagery. There exist many different motion compensation algorithms to deal with target motion [3-5]. Most of the algorithms start with coarse range alignment based on the correlation of the range profiles. Then the phase information within one range cell is utilized to achieve fine motion compensation.

Phase estimation is critical in fine motion compensation. Compared with the amplitude, the phase of the radar signal is much more sensitive to the change in range. Based on the concept of signal parameterization reported in [6, 7], an adaptive joint time-frequency (AJTF) algorithm was proposed in [8] for phase estimation of a prominent point scatterer. In this method, the target motion is modeled as a polynomial function and an exhaustive search procedure is used to find the motion parameters that are embedded in the phase of the prominent point scatterer. While the performance of this algorithm is very good [9], the main bottleneck in this procedure is the computational complexity associated with the parameter search. When the target motion is highly irregular, i.e., when the number of parameters needed to model the motion is large, the use of the exhaustive search becomes prohibitively expensive.

Our objective here is to reduce the computation time associated with the motion parameter search in the AJTF procedure. Our proposed approach is to incorporate genetic algorithms (GA) [10] into the AJTF search process. (Some preliminary work on this topic was reported in [11].) In contrast with conventional optimization methods, GA is a population-based, statistical search technique. It borrows such concepts as inheritance and mutation from the biological evolution process [12]. As a global optimization technique, GA is known to be very easy to implement and applicable to many design and inverse problems [13].

This paper is organized as follows. In Sections II and III, we outline the methodology. The AJTF analysis for ISAR motion compensation is described in Section II. GAs are introduced in Section III. The next two sections include results and analysis. In Section IV, simulations with point scatterers are provided to validate the use of GA for phase estimation. Measurement data processing results are shown in Section V. Finally, conclusions are given in Section VI.

II. ISAR MOTION COMPENSATION USING JOINT TIME-FREQUENCY PROJECTION

We restrict our attention here to rigid body targets with a fixed rotational axis. We also assume that the target undergoes only a small angular rotation within the dwell interval. Under these assumptions,¹

¹We consider the conventional motion assumptions for ISAR imaging in this paper. Those assumptions may not hold for moving ground vehicles or small ships. The reader is referred to [18-20] for a detailed discussion of those more challenging scenarios.

a two-dimensional point scatterer model relates the radar data to a moving target through the following equation:

$$E(f, t_D) = \sum_i \sigma_i \exp \left\{ -j \frac{4\pi f}{c} [r(t_D) + x_i + y_i \varphi(t_D)] \right\} \quad (1)$$

where f is the frequency and t_D is the dwell time. In this model, the radar data is comprised of the sum of responses from a collection of point scatterers. (x_i, y_i) denotes the point scatterer position while σ_i denotes the scatterer strength. The target motion includes both translation motion $r(t_D)$ and rotational motion $\varphi(t_D)$.

After range compression and range alignment to place all the point scatterers in their correct range bins, the radar signal through one range cell r can be expressed in the form of

$$E_r(t_D) = \sum_i \sigma_i \exp \left\{ -j \frac{4\pi f_0}{c} [\Delta r(t_D) + x_i + y_i \varphi(t_D)] \right\} \quad (2)$$

where f_0 is the center frequency of the radar and the index includes only those point scatterers in the particular range cell. The residual translation motion is depicted as $\Delta r(t_D)$. After such coarse alignment procedure, the residual translation motion is smaller than the range resolution. However, it can still be larger than the radar wavelength. Both the residual translation motion $\Delta r(t_D)$ and the rotational motion $\varphi(t_D)$ can be expanded into polynomial functions of the dwell time as

$$\begin{aligned} \Delta r(t_D) &= a_1 t_D + a_2 t_D^2 + a_3 t_D^3 \dots \\ \varphi(t_D) &= b_1 t_D + b_2 t_D^2 + b_3 t_D^3 \dots \end{aligned} \quad (3)$$

where any coefficients beyond the first order are detrimental to ISAR image formation. To solve the ISAR motion compensation problem, we need to determine these motion parameters and to remove the unwanted nonlinear phase terms from the radar data.

This task can be accomplished using the AJTF procedure [8]. The essential idea of this procedure is to find the basis function that most resembles the strongest signal component in (2). For our problem, a basis function in the form of

$$h(t_D) = \exp \left[-j \frac{4\pi f_0}{c} (f_1 t_D + f_2 t_D^2 + f_3 t_D^3 \dots) \right] \quad (4)$$

is used. The best basis is found by searching for parameters f_1, f_2, f_3, \dots that maximize the projection from the radar signal onto the basis, i.e.,

$$\langle f_1, f_2, f_3, \dots \rangle = \arg \max |\langle E_r(t_D), h(t_D) \rangle| \quad (5)$$

where the projection is formulated as the inner product of the two functions as

$$\langle E_r(t_D), h(t_D) \rangle = \int E_r(t_D) h^*(t_D) dt_D \quad (6)$$

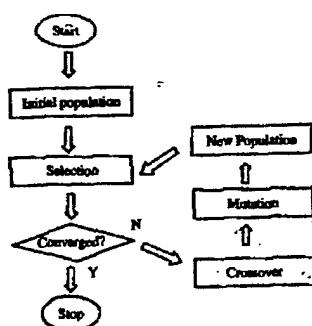


Fig. 1. Flowchart of GA.

In (5), the linear coefficient f_1 can be found efficiently with the fast Fourier transform (FFT). Coefficients for the nonlinear phase terms, f_2, f_3, \dots , must be determined through a more time-consuming search.

After the motion parameters of the prominent point scatterer are found, we can carry out the translation motion compensation by multiplying the radar data with the conjugate of this basis. Since all the point scatterers share the same translation motion in (2), this operation will remove the translation motion of the whole target. Rotational motion compensation can also be carried out by estimating the phase of a second point scatterer in a different range cell. After the phase estimation, we can resample the data in dwell time to make the phase linear [3, 4].

III. USE OF GENETIC ALGORITHMS FOR PHASE PARAMETER SEARCH

As we have discussed in the last section; ISAR motion compensation can be formulated as a parameterization process for both translation motion and rotational motion. In [8], a brute-force search procedure is employed to carry out the parameterization. This means that we exhaustively search the solution space for the maximum projection. GAs are investigated here to search for the motion parameters to reduce the computation time. We should point out that although a structured tree-search is an easy and straightforward way to decrease the computational complexity, it does not always lead to a global optimum.

GA is a global optimization method based on concepts from ecological systems [10, 12, 14]. The flowchart of a typical GA process is illustrated in Fig. 1. It starts by setting up the parameters for both the physical problem and the GA implementation. GA operates on a population of many individuals. The initial population is randomly generated within the searching space. The goodness of the solution is then evaluated based on an objective function. The objective function is chosen as the projection magnitude from the radar signal onto the basis function (see (5)) (although other objective functions

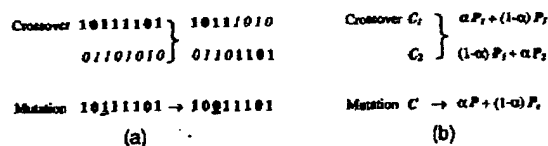


Fig. 2. Examples of crossover and mutation operations in binary and real-coded GA. (a) Binary-coded GA. (b) Real-coded GA.

such as entropy can also be used). The search is carried out in a range cell with a prominent point scatterer. When such a good range cell is not available, multiple range cells can be used to improve the GA phase estimation accuracy. If we are satisfied with the solution, the process is done. Otherwise, a new generation is produced for the next evaluation-reproduction iteration. To make up individuals in the new generation, some good parents are selected from the previous generation and two operations called crossover and mutation are applied to produce children in the next generation. Whether or not crossover and mutation occur is determined randomly. The crossover and mutation probabilities are chosen based on the tradeoff between two conflicting requirements. Increasing the variation in the new generation brings a chance for better solutions, but it tends to lose the features of the good solutions from the previous generation.

Roughly speaking, there are two kinds of GA. One is binary-coded GA [10]. The other is real-coded GA [15]. In the former, the physical parameters to be searched are first discretized into binary bits. There is a one-to-one mapping between a physical parameter C and its N -bit binary representation c_1, c_2, \dots, c_N as follows:

$$C = \frac{C_{\max} - C_{\min}}{2^N - 1} \sum_{i=1}^N c_i 2^{i-1} + C_{\min} \quad (7)$$

where the $[C_{\min}, C_{\max}]$ is the valid search space for C . A candidate solution of the problem is expressed in the form of a chromosome, which is the collection of bits representing all the parameters. For crossover, a random break point in the chromosome is picked. The bits before the point from one parent are combined with the bits after the point from another parent to form one child. Another child is generated in the reverse fashion. For mutation, a single bit is randomly picked and its value is inverted. The crossover and mutation operations for binary-coded GA are depicted in Fig. 2(a).

In real-coded GA, there is no coding-decoding process and the algorithm directly operates on the physical parameters. For crossover, a linear combination is usually used as follows

$$\begin{aligned} C_1 &= \alpha P_1 + (1-\alpha)P_2 \\ C_2 &= (1-\alpha)P_1 + \alpha P_2 \end{aligned} \quad (8)$$

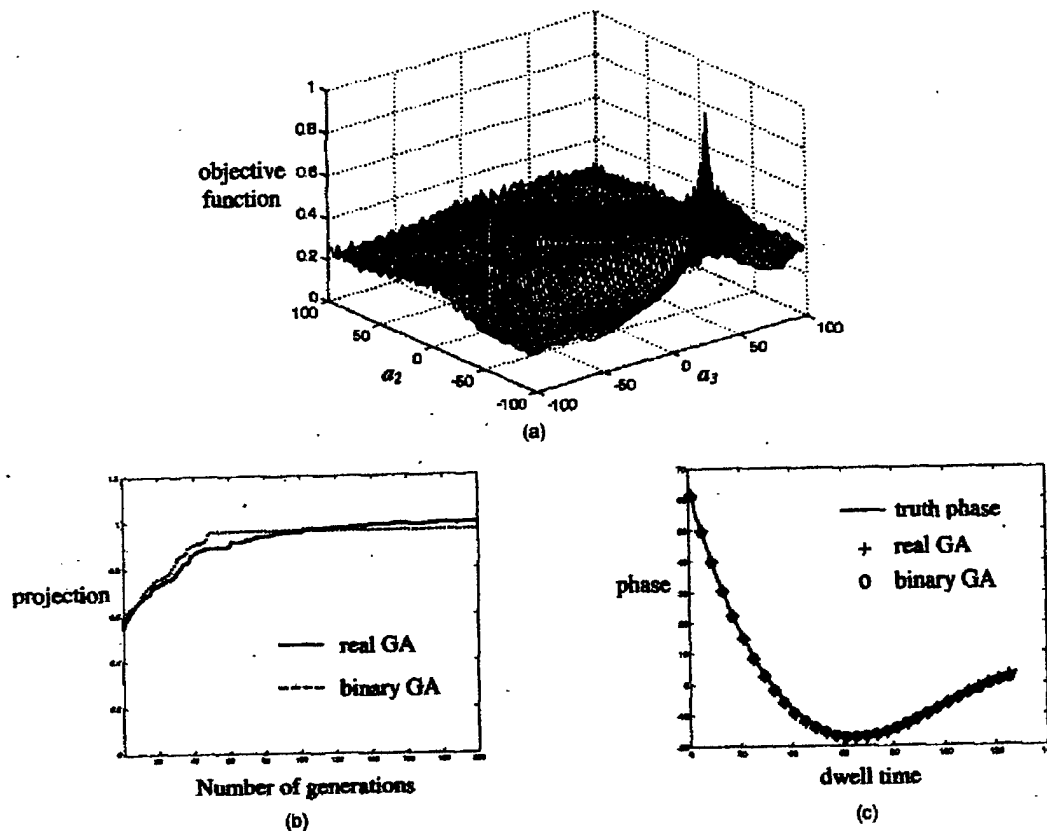


Fig. 3. GA for third-order phase estimation. (a) Multi-modal objective function. (b) GA convergence curves. (c) GA-estimated phase compared to the original truth phase.

where two children (C_1, C_2) are reproduced from two parents (P_1, P_2). α is a random number between 0 and 1 to ensure that the new parameters will not fall out of range. For mutation, a child C that is different from the parent P is needed. For this purpose, a solution P_r is picked up randomly from the searching space and linearly combined with P to generate C in the same way as described by (8). The crossover and mutation operations for real-coded GA are depicted in Fig. 2(b).

The basic theory in GA, the schemata theory, seems to favor the use of binary-coded GA [14]. Most work on GA has followed this path. Recently, researchers have also experimented with real-coded GA and have observed some advantages in convenience and accuracy [16]. In the next section, we test both binary-coded and real-coded GA in our phase estimation problem.

The GA process is usually stopped using criteria based on the performance of the available solutions in the present generation. In our case, we do not know the true maximum projection value. Therefore, we choose to stop the GA process when the projection value does not increase after a certain number of generations.

IV. POINT SCATTERER SIMULATION

Point scatterer simulations are first used to test the use of GA for ISAR motion compensation. We first test the accuracy of GA phase estimation. In this example, we use two point scatterers with amplitudes 1 and 0.2. They are located within one range cell and contain third-order translation motion (i.e., the coefficients a_1, a_2 , and a_3 in (3) are significant while all higher order coefficients are zero). We run both binary-coded GA and real-coded GA to search for a_2 and a_3 for this simple phase estimation problem. The population size is 50. In both cases, the crossover probability is 0.8 and the mutation probability is 0.3. For exhaustive search, the search for a_2 and a_3 is carried out on a 128 by 128 grid. We choose a 7-bit representation in binary-coded GA and search in the same discrete space as in the exhaustive search. The actual objective function surface is plotted in Fig. 3(a). We observe many local maxima, indicating this would be a challenging problem for a local optimization method. Fig. 3(b) shows the GA convergence curve, with the real-coded GA result in solid line and the binary-coded GA result in dashed line. Since GA is a statistical approach, we do not get exactly the same

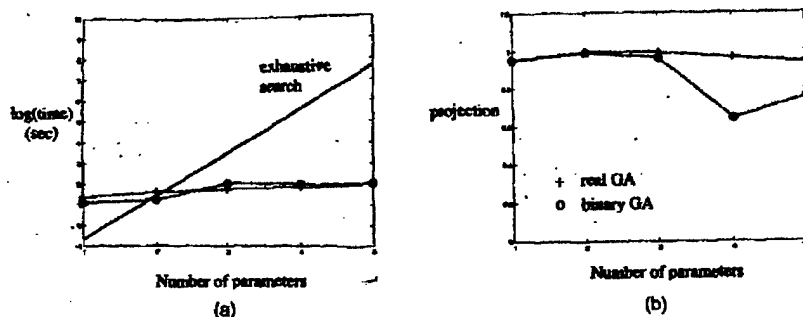


Fig. 4. Performance of GA compared to exhaustive search. (a) Computational complexity as a function of the number of parameters. (b) Accuracy.

result from each GA run. To decrease the statistical variation, the results in Fig. 3(b) are obtained by averaging over 20 GA runs. We can see that after about 150 generations the two projection curves nearly converge to the truth value of 1. We also observe that real-coded GA produces a slightly higher projection value. Fig. 3(c) shows the resulting phase from a single GA run after 200 generations. The estimated phase from binary-coded GA is plotted in circles, the phase from real-coded GA in crosses, and the original phase function in solid line. We see very good agreement among the three results, meaning good accuracy from the two GA results.

In the second example we compare the computational complexity of GA to exhaustive search for different orders of motion. As we have pointed out earlier, the main problem with exhaustive search for motion parameter extraction is the computational load. This problem becomes more acute when the order of the motion is high. Again, we use two point scatterers with amplitudes 1 and 0.2. We generate the radar data from these two point scatterers with some preset motion. We then apply exhaustive search, binary-coded GA, and real-coded GA for the phase estimation problem with different orders of motion. The same GA parameters as in the previous example are used and the results are averaged over 20 runs. The exhaustive search is known to have an exponential complexity of $O(\exp(n))$. As expected, the resulting computation time in logarithm scale shows up as a straight line in Fig. 4(a). For GA, no theoretical complexity formulation is available in general. (The complexity of $O(n \log n)$ is claimed for selected test functions in [17].) We run both binary-coded GA and real-coded GA up to sixth-order motion (i.e., search for 5 parameters) and plot the results in Fig. 4(a). It is observed that both binary-coded GA and real-coded GA have much lower complexity than exhaustive search. The difference in complexity between the two GAs is only minor. The projection values from binary-coded GA and real-coded GA are next plotted in Fig. 4(b) as circles and crosses, respectively. We see that the real-coded GA results are closer to the truth value

of 1.0 than the binary-coded GA results, especially for higher order motions. Since binary-coded GA searches on a finite grid as in exhaustive search, it can never get solutions that surpass the exhaustive search result. On the other hand, real-coded GA has the ability to search for any real values within the search range. Consequently, real-coded GA has more chance of finding a better solution. The same trend is also observed with measurement data and is discussed further in the next section.

V. MEASUREMENT DATA PROCESSING

We next apply GA on some measurement data. The data were collected from an in-flight aircraft using ground radar. 128 pulses are processed to form an ISAR image. This corresponds to an imaging interval of about 2.5 seconds. GA is evaluated for fine motion compensation. For the first data set, the image without any fine motion compensation is shown in Fig. 5(a). This image is unfocused due to the residual motion. We select a range cell with a dominant scatterer (range cell 79) and apply GA to estimate the phase based on a third-order translation motion model. The resulting images from binary-coded and real-coded GA are shown in Figs. 5(b) and 5(c), respectively. We observe that the two GA images are as focused as the reference image in Fig. 5(d) obtained using exhaustive search. The corresponding projection values are 2401 and 2595, as compared to the exhaustive search result of 2401. We continue this comparison using 19 other imaging intervals. Fig. 6(a) shows the projection values (normalized with respect to the exhaustive search result) for the 20 frames. For 19 out of 20 frames, real-coded GA gives larger projection values than exhaustive search. The resulting images are either on par or slightly better focused than those obtained from exhaustive search. For binary-coded GA, 7 frames have lower projection values and are of inferior image quality to those from exhaustive search. The other 13 frames have exactly the same projection values as the exhaustive search result. Similar to our conclusion earlier based on the simulation data, our experience with the

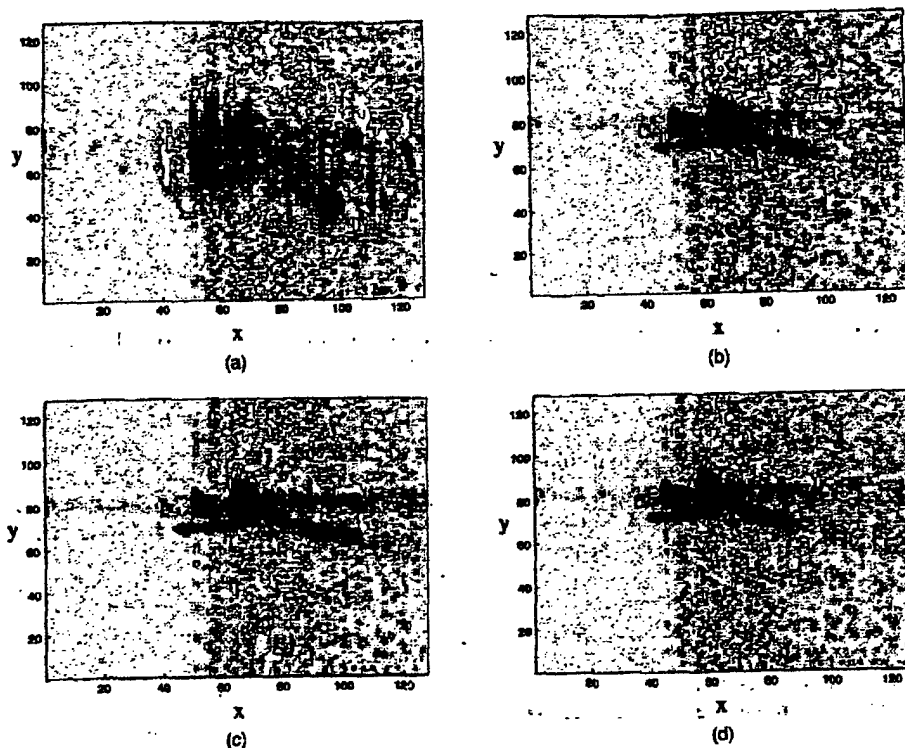


Fig. 5. Translation motion compensation applied to measurement data using a third-order motion model. (a) Image before fine motion compensation. (b) Binary-coded GA result. (c) Real-coded GA result. (d) Exhaustive search result.

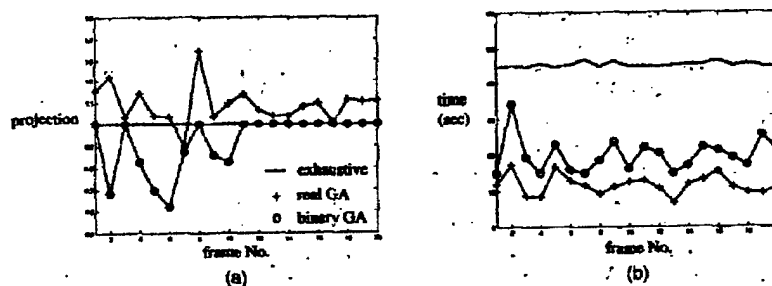


Fig. 6. Comparison of performance of GA and exhaustive search using measurement data. (a) Projection value. (b) Computation time.

measurement data indicates that real-coded GA consistently outperforms binary-coded GA in terms of accuracy. The computation time using Matlab codes on a Pentium III 750MHz PC is summarized in Fig. 6(b). While there is little change in the computational time for exhaustive search from one frame to another, the times for binary-coded and real-coded GA exhibit large variations in these single run results due to the statistical nature of GA. The average times for the binary-coded and real-coded GA are 19.5 s and 11.5 s, respectively. This is compared with the 45.5 s from exhaustive search. Finally, we note that for these 20 frames the third-order model is adequate

to model the translation motion. Inclusion of higher order translation motion or rotational motion does not improve the image quality for this data set.

For a second data set, we first apply third-order translation motion compensation using real-coded GA. The resulting image is shown in Fig. 7(a). It is seen that the selected dominant point scatterer at range cell 64 is not well focused. This means that the target contains higher motion that cannot be fully compensated by the third order motion model. This fact is also revealed by the spectrogram of the compensated signal in Fig. 7(b), as we observe a curved joint time-frequency (JTF) trajectory for

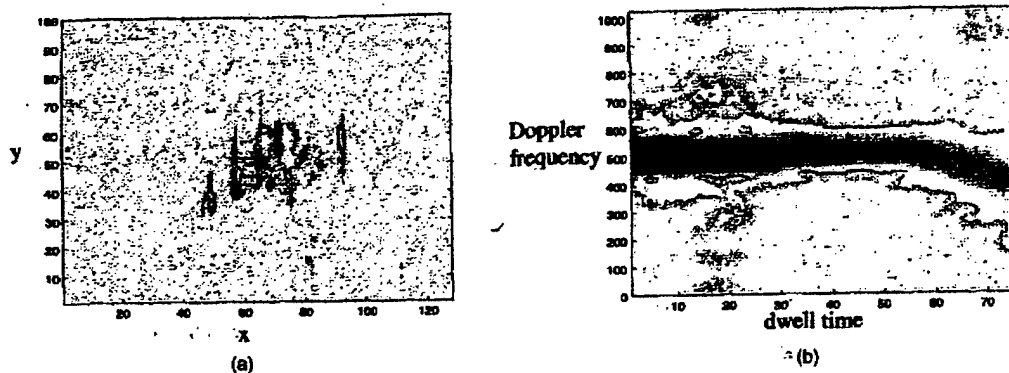


Fig. 7. Motion compensation example for another measurement data set. (a) Image after third-order translation motion compensation using real-coded GA. (b) Spectrogram of signal in range cell 64.

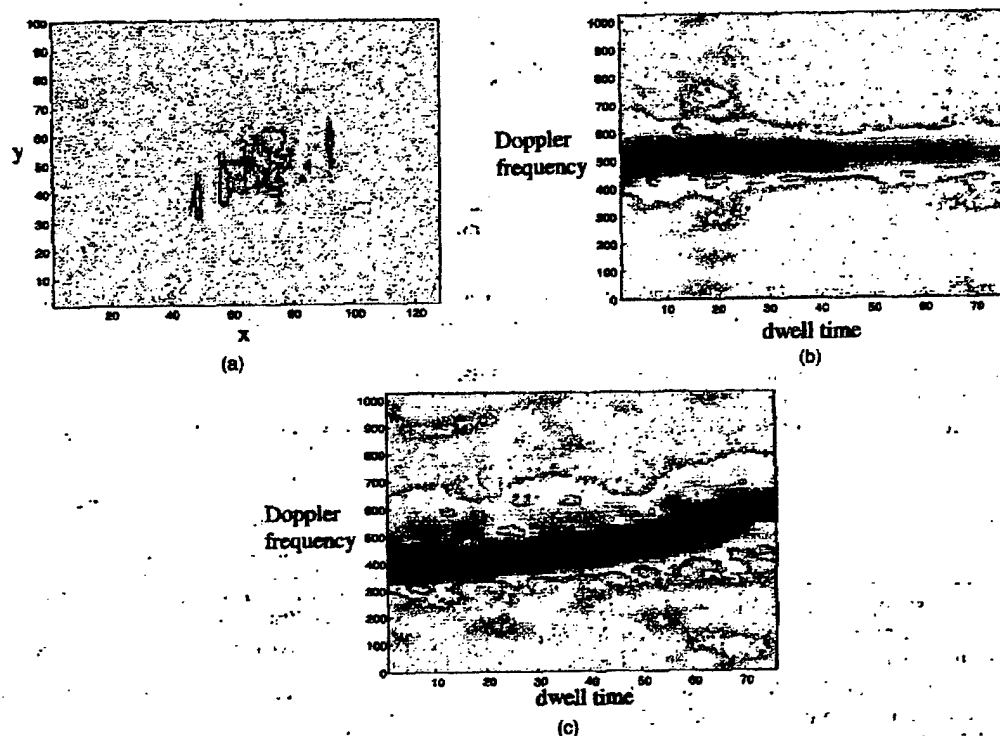


Fig. 8. Higher-order translation motion compensation. (a) Image after fourth-order translation motion compensation using real-coded GA. (b) Spectrogram of signal in range cell 64. (c) Spectrogram of signal in range cell 71.

the scatterer. Next, a fourth-order motion model is tried and the real-coded GA result is shown in Fig. 8(a). From this figure, the reference point scatterer is better focused and the spectrogram of the signal is straightened in Fig. 8(b). Fifth-order translation motion is also attempted, and the result does not show much improvement. However, we observe that other point scatterers in Fig. 8(a) are still smeared. This is confirmed by the spectrogram of the signal at a different range cell (number 71) shown in Fig. 8(c),

which shows that the signal trajectory is curved in the spectrogram. Thus rotational motion must exist in this data. We next apply fourth-order rotational motion compensation using real-coded GA. As shown in Fig. 9(a), the whole target is much better focused after the compensation. The spectrograms of the signal at both range cells become straightened in Figs. 9(b) and 9(c). While real-coded GA takes 45 s for the phase estimation problem, the computation time for fourth-order exhaustive search is estimated to be over

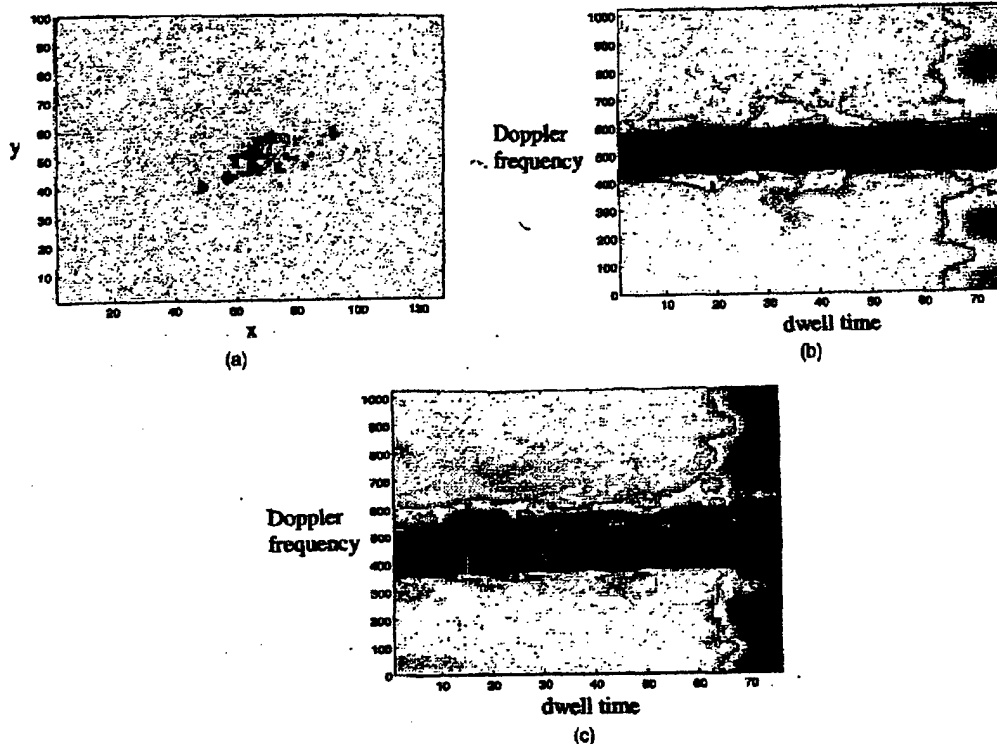


Fig. 9. Higher-order rotational motion compensation. (a) Image after fourth-order rotational motion compensation using real-coded GA. (b) Spectrogram of signal in range cell 64. (c) Spectrogram of signal in range cell 71.

50 min based on the complexity curve in Fig. 4(a). Therefore, the time savings of GA over exhaustive search is quite significant in this real-world example.

VI. CONCLUSIONS

In this paper, GAs have been applied to ISAR motion compensation. Based on the AJTF analysis, GA is used in the phase estimation of prominent point scatterers on the target. The resulting parameterized phases are then used for translation and rotational motion compensation. Both binary-coded GA and real-coded GA have been implemented and tested using simulation and measurement data. It is found that real-coded GA outperforms binary-coded GA in terms of accuracy in the phase estimation problem. It is also shown that the computational complexity of the GA search is much less than that of exhaustive search. The time savings can become especially significant when the target exhibits higher order motions.

JUNFEI LI
HAO LING
Department of Electrical and
Computer Engineering
The University of Texas at Austin
Austin, TX 78712-1084

REFERENCES

- [1] Ausherman, A., Kozma, A., Waker, J. L., Jones H. M., and Poggio, E. C. (1984) Developments in radar imaging. *IEEE Transactions on Aerospace Electronic Systems* AES-20 (Apr. 1984), 363-400.
- [2] Chen, C. C., and Andrews, H. C. (1980) Target motion induced radar imaging. *IEEE Transactions on Aerospace Electronic Systems*, AES-16 (Jan. 1980), 2-14.
- [3] Carrara, W. G., Goodman, R. S., and Majewski, R. M. (1995) *Spotlight Synthetic Aperture Radar—Signal Processing and Algorithms*. Boston, MA: Artech House, 1995.
- [4] Ribaczek, A. W., and Herzkowitz, S. J. (1996) *Radar Resolution and Complex-Image Analysis*. Boston, MA: Artech House, 1996.
- [5] Werness, S., Carrara, W., Joyce, L., and Franczak, D. (1990) Moving target imaging algorithms for SAR data. *IEEE Transactions on Aerospace Electronic Systems*, 26, 1 (Jan. 1990), 57-67.
- [6] Mallat, S. G., and Zhang, Z. (1993) Matching pursuits with time-frequency dictionaries. *IEEE Transactions on Signal Processing*, 41, 12 (Dec. 1993), 3397-3415.
- [7] Qian, S., and Chen, D. (1994) Signal representation using adaptive normalized Gaussian functions. *Signal Processing*, 36, 1 (Mar. 1994), 1-11.

- [8] Wang, Y., Ling, H., and Chen, V. C. (1998)
ISAR motion compensation via adaptive joint time-frequency technique.
IEEE Transactions on Aerospace Electronic Systems, 34 (Apr. 1998), 670-677.
- [9] Li, J., Wang, Y., Bhalla, R., Ling, H., and Chen, V. C. (1999)
Comparison of high-resolution ISAR imagery from measurement data and synthetic signatures.
In *Proceedings of the SPIE 44th Annual Meeting, Radar - Processing, Technology, and Applications*, vol. 3810, Denver, CO, July 1999, 170-179.
- [10] Goldberg, D. E. (1989)
Genetic Algorithms in Search, Optimization and Machine Learning.
Reading, MA: Addison-Wesley, 1989.
- [11] Li, J., and Ling, H. (2001)
ISAR motion detection and compensation using genetic algorithms.
In *Proceedings of SPIE Wavelet Applications VIII*, vol. 4391, Orlando, FL, Apr. 2001, 380-388.
- [12] Mitchell, M., and Taylor, C. E. (1999)
Evolutionary computation: An overview.
Annual Review of Ecology and Systematics, 30 (1999), 593-616.
- [13] Rahmat-Samii, Y., and Michielssen, E. (Eds.) (1999)
Electromagnetic Optimization by Genetic Algorithms.
New York: Wiley, 1999.
- [14] Holland, J. H. (1975)
Adaptation in Natural and Artificial Systems: An Introductory Analysis with Applications to Biology, Control, and Artificial Intelligence.
Ann Arbor, MI: The University of Michigan Press, 1975.
- [15] Goldberg, D. E. (1991)
Real-coded genetic algorithms, virtual alphabet, and blocking.
Complex Systems, 5 (1991), 139-167.
- [16] Herrera, F., Lozano, M., and Verdegay, J. L. (1998)
Tackling real-coded genetic algorithms: Operators and tools for behavioral analysis.
Artificial Intelligence Review, 12 (1998), 265-319.
- [17] Salomon, R. (1995)
Genetic algorithms and the $O(n \ln n)$ complexity on selected test functions.
Proceedings of Artificial Neural Networks in Engineering (ANNIE'95), New York, NY: ASME Press, 1995, 325-330.
- [18] Ribaczek, A. W., and Hershkowitz, S. J. (2000)
Theory and Practice of Radar Target Identification.
Boston, MA: Artech House, 2000.
- [19] Li, J., and Ling, H. (2001)
An algorithm to detect the presence of 3D target motion from ISAR data.
Multidimensional Systems and Signal Processing (special issue on radar signal processing), 14, 1 (2003), 223-240.
- [20] Li, J., and Ling, H. (2002)
ISAR feature extraction from non-rigid body targets using adaptive chirplet representation.
In *2002 IEEE AP-S International Symposium Digest*, San Antonio, TX, June 2002.

Global Range Alignment for ISAR

A new technique is developed for range alignment in inverse synthetic aperture radar (ISAR) imaging. The shifts made to the echoes are modeled as a polynomial, and the coefficients of this polynomial are chosen to optimize a global quality measure of range alignment. This technique is robust against noise and target scintillation, and avoids error accumulation. In addition, the shift in the time domain is implemented by introducing a phase ramp in the frequency domain, which removes the limitation of integer steps.

I. INTRODUCTION

Inverse synthetic aperture radar (ISAR) utilizes the Fourier transform to resolve the scatterers in azimuth. Before taking the Fourier transform, translation compensation is needed to remove the effects of the translation between the radar and the target in range. Translation compensation consists of range alignment, which shifts the echoes such that the signals from the same scatterer are centered at the same range bin in different echoes, and phase adjustment, which removes the Doppler phase caused by the translation.

If no prior knowledge is available about the translation, range alignment is usually based on the similarity of the envelopes of the echoes. Typical methods include the peak method [1], the maximum-correlation method [1], the frequency-domain method [1], the Hough-transform method [2] and the minimum-entropy method [3].

These methods, however, have a variety of disadvantages. The maximum-correlation method, for example, aligns each echo using the principle that the envelope correlation of two adjacent echoes is a maximum when they are aligned. Although more robust than the peak method, the method is still somewhat sensitive to noise and target scintillation. Also, it has the defect of error accumulation. In addition, the shift in the time domain has the limitation of integer steps, which means that even if two echoes are correctly aligned, there may still be an error of up to half a range bin.

We develop a new technique for range alignment in ISAR imaging. The shifts made to the echoes are modeled as a polynomial, and the coefficients of this polynomial are chosen to optimize a global quality

Manuscript received April 16 2001; revised September 17 and November 12, 2002; released for publication November 20, 2002.

IEEE Log No. T-AES/39/1/808687.

Refereeing of this contribution was handled by L. M. Kaplan.

0018-9251/03/\$17.00 © 2003 IEEE

the proposed codec averagely saves 8% bit rate compared to JM3.9 with the best settings. Complexity comparison between JM3.9 with five reference frames and the proposed algorithm is also analysed. The sprite buffer can be restricted within the constant size (e.g. 2.25 times the frame size). Therefore the memory cost in the proposed sprite coding is less than that in JM3.9. For computing complexity analysis, we only consider the computing time of motion estimation. In JM3.9, the local motion estimation (LME) is performed five times (i.e. once for each reference frame). In the proposed codec, LME is performed only once. The total time of motion estimation in the proposed codec is for one LME and one GME. By utilising the fast GME algorithm, the total time for LME plus GME is less than five times LME in JM3.9. Similar to the traditional dynamic sprite coding techniques, the proposed codec has the disadvantage that sprite warping has to be performed in the decoder. However, considering the significant improvement of coding efficiency, the extra computing complexity for sprite warping is acceptable.

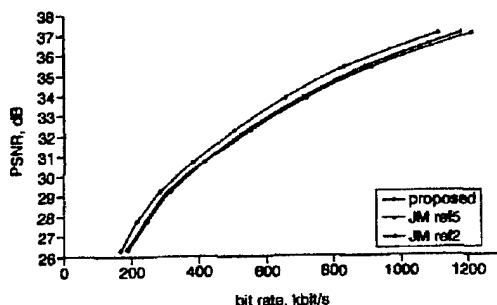


Fig. 3 PSNR bit rate curves achieved from testing on Stefan sequence

Conclusions: We have presented a highly efficient algorithm for dynamic sprite coding. The high coding efficiency is achieved due to two reasons. First, the new techniques developed in JVT codec are utilised; secondly, the fractional resolution sprite prediction is incorporated into the proposed algorithm.

© IEE 2003

12 November 2002

Electronics Letters Online No: 20030199

DOI: 10.1049/el:20030199

Yan Lu (Department of Computer Science, Harbin Institute of Technology, Harbin, 150001, People's Republic of China)

E-mail: ylu@jdl.ac.cn

Wen Gao (Institute of Computing Technology, Chinese Academy of Sciences, Beijing 100080, People's Republic of China)

Feng Wu (Microsoft Research Asia, Beijing 100080, People's Republic of China)

References

- SMOLIC, A., SIKORA, T., and OHM, J.-R.: 'Long-term global motion estimation and its application for sprite coding, content description, and segmentation', *IEEE Trans. Circuits Syst. Video Technol.*, 1999, 9, pp. 1227-1242
- Joint Video Team of ISO/IEC MPEG and ITU-T VCEG: 'Joint committee draft (CD)', Fairfax, USA, May 2002

Shape inversion of metallic cavities using hybrid genetic algorithm combined with tabu list

Yong Zhou, Junfei Li and Hao Ling

An approach combining the hybrid genetic algorithm (GA) with the tabu list concept is proposed to increase the search efficiency of the hybrid GA. The algorithm is applied to reconstruct the shape of a metallic cavity based on the Ipswich measurement data. Inversion results show good agreement with the actual shape and significant improvement in convergence rate over both simple GA and hybrid GA.

Introduction: Electromagnetic inverse scattering entails the reconstruction of the shape or material of an object from its scattered field data. The inverse problem can be cast into an optimisation problem whereby the difference between the measured fields and the computed fields from a forward electromagnetic solver is minimised. Genetic algorithms (GAs) have been tried as the global optimiser in these problems [1-3]. While GA is well suited in searching for the global optimum, it suffers from slow convergence. Since the evolutionary process for the standard GA to reach a cost minimum is in general very slow in comparison to a local search algorithm, a natural improvement to speed up the simple GA is to hybridise the simple GA with a local search. This type of algorithm is usually called the hybrid GA (HGA) and has been explored by researchers in different disciplines [4, 5]. While showing improvements in performance, the hybridisation of the two approaches also causes some inefficiency. As the parent selection scheme of GA gives priority to the best members, it usually leads to a population that is highly clustered around the local minima. This clustering is necessary for the simple GA to evolve closer to the exact minimum. For HGA, however, since the local minima have been completely explored by the local search, such clustering will lead to the re-exploration of these regions, which is quite wasteful.

Tabu search (TS) is another global search strategy that has been developed for combinatorial problems [6, 7]. It is a local search algorithm with memory. The most important feature of TS is that it utilises a tabu list to prevent the revisiting of local minima. In this Letter, we propose a technique combining HGA with the tabu list concept to increase the efficiency of the HGA. The tabu list is adopted to exclude those regions in the parameter space that have already been explored by the local search. In this manner, there will be no revisiting of the explored regions and the GA population can be spread out to explore new regions, thus improving the search efficiency. We apply this algorithm to the electromagnetic inverse problem of shape reconstruction of metallic cavity structures containing strong multiple scattering effects. Results based on the Ipswich measurement data set are presented.

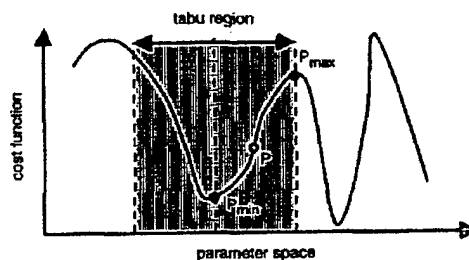


Fig. 1 Establishment of 'tabu region'

HGA-tabu approach: In our HGA-tabu implementation, the initial generation is produced randomly. The new population is then produced through the selection, crossover and mutation operators. After these standard GA processes, the best member P is selected as the initial guess to carry out a local search. We adopt the gradient search reported in [8] as the local search algorithm. The resulting local minimum in the parameter space is denoted as P_{min} (see Fig. 1). P_{min} is then placed into the new GA population. In addition, a gradient search is also carried out to obtain the local maximum P_{max} from the same initial guess in order to estimate the extent of the local minimum. Once both local searches are completed, we define the region that is centred at the minimum and limited by the radius $|P_{max} - P_{min}|$ as the 'tabu region', and record it into a tabu list. Symmetry around the local minimum is assumed in this construct. In subsequent GA reproductions, all of the new members are checked against this tabu list to ensure that none is in the tabu regions of the sample space. Thus the population is forced to spread out to the unexplored regions, resulting in higher HGA search efficiency. Further, a new tabu region is appended to the tabu list every time a new local minimum is explored by local search.

In implementing the inverse problem to reconstruct the shape of a cavity from its scattered field data, we start from a set of randomly created shapes that are described by N ordered points in a two-

dimensional space. The profile of the object is then obtained using spline interpolation. Next, the method of moments (MoM) solution to the electric field integral equation is used as the forward electromagnetic solver to generate the computed scattered field E^{cal} from each assumed shape. A cost function is defined as the root-mean-squared (rms) difference between E^{cal} and the measured scattered-field E^{mea} . The HGA-tabu algorithm is then applied as the optimiser to minimise the cost function. Binary-encoded GA is used in our implementation.

Results: We have applied the HGA-tabu algorithm to reconstruct the shape of a metallic, partially open, circular cylindrical cavity with a diameter of 10.8 cm (Ips011 in the Ipswich data set) [9]. The measurement was taken at a single frequency of 10 GHz in a bistatic configuration. There were a total of 36 transmitter positions around the object and 18 receiver locations for each transmitter position. The electric field was parallel to the axis of the cylinder.

The number of the population for GA was set to 200, the geometry was described by $N=5$ points, and the crossover and mutation rates were set to 0.8 and 0.4, respectively. The search area was chosen to be 16.2×16.2 cm. We first tested the inversion algorithms using MoM-simulated field data as the input. The results showed that the HGA-tabu was able to converge to the correct shape after an average of 75 generations and the final shape was in excellent agreement with the actual shape. In comparison to the HGA, the HGA-tabu also showed an improvement of about 100 generations for convergence.

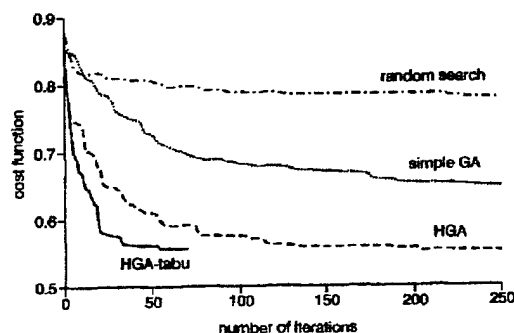


Fig. 2 Convergence comparison for inversion of Ips011 for random search, simple GA, HGA and HGA-tabu

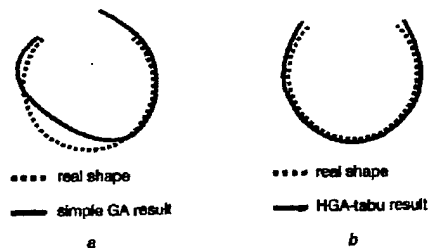


Fig. 3 Ips011 inversion results from measured data

a Typical inversion result by simple GA
b Typical inversion result by HGA-tabu

Next, we applied the inversion algorithms to the actual measured data for Ips011. Fig. 2 shows the convergence comparison between random search, simple GA, HGA and HGA-tabu. All the results were averaged over 10 independent runs with different initial populations. As expected, the simple GA showed improvement over the random search. The HGA further improved the convergence rate of the simple GA. The best results were consistently obtained by the HGA-tabu. To achieve an rms of 0.55, the HGA required an average of 220 generations while the HGA-tabu algorithm required only an average of 75 generations. (We note here that, due to the difference between the numerical modelling and the measurement, the rms error between the MoM-computed fields from the exact shape and the measured field data is 0.73.) Fig. 3a shows the typical shape from the simple GA after 250 generations plotted against the real profile of the cavity. The result

indicates that more iterations are needed for convergence. Fig. 3b shows the typical reconstructed shape from the HGA-tabu after 75 generations. As we can see, the inverted shape is very close to the real profile. The overhead of implementing the gradient search in each generation is about 10% of the total computation cost. The time for the tabu list check is negligible, as there is no cost function evaluation.

Conclusion: An approach combining the hybrid genetic algorithm with the tabu list concept has been proposed in this Letter. The tabu list was set up to increase the search efficiency by forbidding revisits of local minima already explored by the local search. The algorithm has been applied to reconstruct the shape of a metallic cavity based on the measured Ipswich data. Inversion results from the HGA-tabu showed faster convergence and higher success rate than those of the simple GA and hybrid GA. The computation overhead per generation for the new algorithm was small. The algorithm could potentially be useful in other optimisation problems.

Acknowledgment: This work is supported by the Office of Naval Research under Contract No. N00014-03-1-0021.

© IEE 2003

6 November 2002

Electronics Letters Online No: 20030207

DOI: 10.1049/el:20030207

Yong Zhou and Hao Ling (Department of Electrical and Computer Engineering, The University of Texas at Austin, Austin, TX 78712-1084, USA)

Junfei Li (Department of Electrical Engineering, The University of Texas-Pan American, Edinburg, TX 78539, USA)

References

- CHU, C.C., and LIU, P.T.: 'Image reconstruction of a perfectly conducting cylinder by the genetic algorithm', *IEEE Proc., Microw. Antennas Propag.*, 1996, 143, (3), pp. 249-253
- PASTORINO, M., MASSA, A., and CAORSI, S.: 'A microwave inverse scattering technique for image reconstruction based on a genetic algorithm', *IEEE Trans. Instrum. Meas.*, 2000, 49, pp. 573-578
- ZHOU, Y., and LING, H.: 'Electromagnetic inversion of Ipswich objects with the use of the genetic algorithm', *Microw. Opt. Tech. Lett.*, 2002, 33, pp. 457-459
- YEN, J., LIAO, J.C., LEE, B., and RANDOLPH, D.: 'A hybrid approach to modeling metabolic systems using genetic algorithm and simplex method', *IEEE Trans. Syst. Man Cyber.*, 1998, 28, pp. 173-283
- PARK, C., and JEONG, B.: 'Reconstruction of a high contrast and large object by using the hybrid algorithm combining a Levenberg-Marquardt algorithm and a genetic algorithm', *IEEE Trans. Magn.*, 1999, 35, pp. 1582-1585
- GLOVER, F.: 'Tabu search—part I', *ORSA J. Comput.*, 1989, 1, pp. 190-206
- GLOVER, F., and LAGUNA, M.: 'Tabu search: modern heuristic techniques for combinatorial problems' (Blackwell Scientific Publication, Oxford, UK, 1993)
- OTTO, G.P., and CHEW, W.C.: 'Microwave inverse scattering-local shape function imaging for improved resolution of strong scatters', *IEEE Trans. Microw. Theory Tech.*, 1994, 42, pp. 137-141
- MCGAHAN, R.V., and KLEINMAN, R.E.: 'Second annual special session on image reconstruction using real data', *IEEE Antennas Propag. Mag.*, 1997, 39, pp. 7-9

Publicly verifiable authenticated encryption

Changshe Ma and Kefei Chen

A new authenticated encryption scheme with public verifiability is presented. The new scheme requires less computational costs and communication overhead than the conventional signature-then-encryption approaches. Furthermore the message is not divulged during the public verification.

Introduction: Secure and authenticated message deliver/storage is one of the major aims of computer and communication security research. Horster, Michels and Petersen (HMP for short) [1] proposed an efficient authenticated encryption scheme with lower expansion

- 4 KAGAWA, K., *et al.*: 'Pixel design of pulsed CMOS image sensor for retinal prosthesis with digital photosensitivity control', *Electron. Lett.*, 2003, 39, p. 419
- 5 SHEN, C., *et al.*: 'Improved SOI image sensor design based on backside illumination on silicon-on-sapphire (SOS) substrate'. IEEE Int. SOI Conf., Williamsburg, VA, USA, 2002, pp. 73-74
- 6 STETT, A., *et al.*: 'Electrical multisite stimulation of the isolated chicken retina', *Vis. Res.*, 2000, 40, pp. 1785-1795

Sparse parameterisation of electromagnetic scattering data using genetic algorithm with adaptive feeding

J. Li, Y. Zhou and H. Ling

A method is presented to parameterise scattering data from complex targets. Based on a global model with both scattering centres and resonances, a genetic algorithm with adaptive feeding is proposed for a sparse representation. The algorithm is tested with measurement data and shows better performance than non-global parameterisation methods.

Introduction: Obtaining a sparse, physical representation of electromagnetic scattering data from a complex target is a problem of fundamental importance in radar signature analysis [1-9]. The scattering centre model is the standard way to represent scattering from large targets and has been used with success by the radar signature community for over two decades. Many techniques including super-resolution [1, 2], CLEAN [3], genetic algorithms (GA) [4-6] and evolutionary programming-based CLEAN [7] have been reported for determining model parameters based on the scattering centre model.

For targets containing convex, interior structures such as cavities, a model combining scattering centres and resonances has been shown to be a more efficient and physically meaningful representation of both exterior and interior scattering features [8, 9]. However, finding the model parameters in such cases is more challenging, since the scattering centre and resonance bases have complementary behaviours in time and frequency. In [8], a CLEAN-based algorithm was used to extract one scattering centre and/or resonance at a time iteratively. In [9], Prony's method was first used to extract all the scattering centres and then all the resonances. One drawback of these methods is that the parameterisation results are not very sparse since the scattering centres and resonances are not extracted simultaneously.

To improve the sparsity, we present in this Letter a global algorithm to parameterise complex scattering data using the combined scattering centre and resonance model. The method is based on a GA with adaptive feeding. The latter is devised to compensate for the disparity in strength between scattering centres and resonances and improve the performance of the GA.

GA with adaptive feeding: The scattering model is assumed to comprise responses from both scattering centres and resonances as [9]:

$$E(f) = \sum_{m=1}^M a_m f^{\alpha_m} e^{-j2\pi f t_m} + \sum_{n=1}^N b_n \frac{1}{j2\pi(f - f_n) + \beta_n} e^{-j2\pi f \tau_n} \quad (1)$$

where M and N are the number of scattering centres and resonances, respectively, and f the frequency. For each scattering centre, t_m is the time delay, α_m the frequency dependency coefficient and a_m the complex amplitude. For each resonance of complex amplitude b_n , f_n is the resonant frequency, τ_n the turn-on time and β_n the Q -factor. The parameterisation process can be formulated as a minimisation problem:

$$\{\alpha_m, t_m, f_n, \beta_n, \tau_n\} = \arg \min \|E(f) - E^w(f)\|_2 \quad (2)$$

where E^w denotes the measurement data to be parameterised. The amplitudes a_m and b_n are not included in the bracket as they can be derived from other unknowns using minimum least squares fitting.

GA has been used in many engineering applications as a global optimisation scheme. However, here we find that the standard simple GA (SGA) has difficulty in converging to the desired global optimum. Since the energy in a resonant term is typically much lower than that in a scatterer centre, the resonant terms are easily missed in the SGA

process. To overcome this, a parameterisation based on a community GA with adaptive feeding is devised. Fig. 1 illustrates the approach in extracting M scattering centres and N resonances. Each solid box represents a community [10] using a different parameterisation order number. For example, the highest order uses M scattering centres and N resonances while the lowest order uses one scattering centre and no resonance. The parameterisation consists of an iteration process as follows. First, for each community, standard GA operations including selection, crossover and mutation are used to reproduce members in the next generation for better solutions. Secondly, at the end of each generation, the residual signal of each community is calculated as the error between the best solution in the community and the original data $E^w(f)$ and is parameterised with GA. The order number for residual parameterisation is specified in the dashed box. It is the difference between the order number of the current community and the next higher community. Thirdly, the parameters from the best solution of a lower order community and its residue are combined to form a candidate solution in the next higher order community. A zero-mean Gaussian perturbation is added during this step to create a community-level mutation. By adaptively feeding the solutions from the lower order communities forward to the higher order communities, the convergence of the highest order community is significantly accelerated without sacrificing the optimality of the final solution.

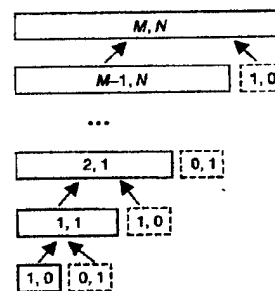


Fig. 1 GA with adaptive feeding

Best solution from lower order community (solid box) and residue (dashed box) combined and fed into next higher-order community. Convergence of highest order community with M scattering centres and N resonances accelerated

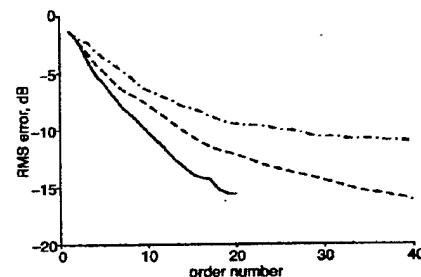


Fig. 2 Comparison of three parameterisation results of VFY 218 measurement data

--- CLEAN with scattering centres only
 -.-.- CLEAN with scattering centres and resonances
 — GA with adaptive feeding

VFY 218 measurement data results: The algorithm was first tested using numerical simulation data from a well-understood target, a plate with a partially open cavity [9]. The proposed method successfully extracted the four dominant scattering centres and three resonances with a 5% RMS error. By comparison, the RMS error from the CLEAN method is 10% after 20 terms, while the SGA always missed the weakest resonance. We next applied it to the VFY 218 measurement data [11]. The scattering data came from a 1:30 scale model aircraft using horizontal polarisation in the 8 to 16 GHz frequency band. The look angle was at 19.6° from nose-on so that the inlet contribution was prominent in the return. Fig. 2 shows RMS error against total model order number ($M+N$) for three different methods. The GA results were averaged over six runs. The CLEAN curve

with scattering-centre-only model decreases very little after 30 terms, indicating this model is very inefficient in modelling the resonance part of the data after the scattering centres are extracted. The CLEAN curve with both scattering centre and resonance model is better. However, the rate of convergence still slows down considerably after the first 18 terms. The GA curve shows the best sparsity. It requires only 20 terms to achieve the same accuracy as the CLEAN approach with 40 terms. The model orders used in the GA are $M=14$ and $N=6$. However, we found that the results were not very sensitive to the model order selection.

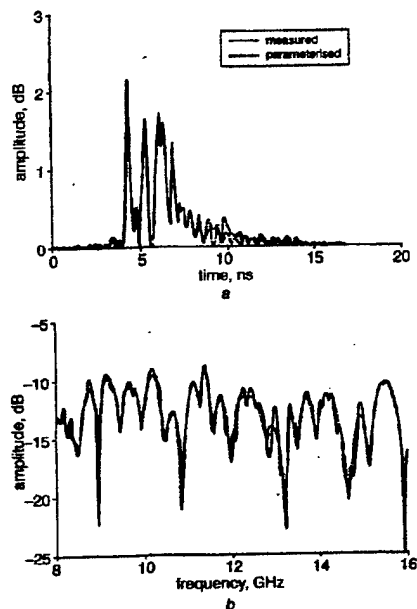


Fig. 3 Accuracy of parameterisation in time and frequency domains
a Time domain
b Frequency domain

To further interpret the physical significance of the GA-parameterised data, we correlated the extracted scattering centre positions with the peaks in the target range profile and found that they lined up well. Furthermore, the two strongest resonances extracted are at frequencies of 9.8 and 11.3 GHz. This is consistent with the size of the rectangular engine inlet openings, which have dimensions of 2.5×1.5 cm. (The cutoff frequencies of the TE_{01} and TE_{11} modes are estimated at 10 and 11.7 GHz, respectively.) The other four resonances at 8.6, 9.1, 9.4 and 13.3 GHz are harder to interpret given the complex shape of the actual inlet structure.

Comparisons of the parameterised result with the original measurement data in the time and frequency domains are shown in Fig. 3. We see fairly good agreements between the two. We suspect the small parameterisation error to be due to the model mismatch of (1) to the complex measurement data. Thus, increasing the model order for this data does not reduce the error significantly. We also processed data from 0° to 180° from nose-on in 5° increments, and found the GA with adaptive feeding to consistently outperform CLEAN at all angles.

Conclusions: We have proposed a GA-based method for parameterising scattering data from complex targets. Based on a global model with both scattering centres and resonances, our method uses GA with the adaptive feeding idea to simultaneously extract all the model parameters. The proposed method can achieve sparser results than other non-global based methods. The effectiveness of the proposed method is demonstrated using the VFY 218 measurement data. The resulting sparse model facilitates target feature interpretation and can be used for signature reconstruction in modelling and simulation applications.

Acknowledgment: This work is supported by the Office Of Naval Research under Contract No. N00014-03-1-0021.

© IEE 2003

9 April 2003

Electronics Letters Online No: 20030723

DOI: 10.1049/el:20030723

J. Li (Department of Electrical Engineering, University of Texas-Pan American, Edinburg, TX 78539, USA)

Y. Zhou and H. Ling (Department of Electrical and Computer Engineering, University of Texas at Austin, Austin, TX 78712, USA)

References

- HURST, M.P., and MITTRA, R.: 'Scattering center analysis via Prony's method', *IEEE Trans. Antennas Propag.*, 1987, 35, (8), pp. 986-988
- MOGIHADDAR, A., OGAWA, Y., and WALTON, E.K.: 'Estimating the time delay and frequency decay parameters of scattering components using a modified MUSIC algorithm', *IEEE Trans. Antennas Propag.*, 1994, 42, (10), pp. 1412-1418
- BHALLA, R., and LING, H.: 'Three-dimensional scattering center extraction using the shooting and bouncing ray technique', *IEEE Trans. Antennas Propag.*, 1996, 44, (11), pp. 1445-1453
- LI, Q., et al.: 'Scattering center analysis of radar targets using fitting scheme and genetic algorithm', *IEEE Trans. Antennas Propag.*, 1996, 44, (2), pp. 198-207
- HUGHES, E.J., and LEYLAND, M.: 'Using multiple genetic algorithms to generate radar point-scatterer models', *IEEE Trans. Evol. Comput.*, 2000, 4, (2), pp. 147-163
- SU, T., and MITTRA, R.: 'A genetic-algorithm-based extrapolation technique for high frequency scattering analysis', *Proc. 2002 URSI National Radio Science Mtg.*, San Antonio, TX, USA, 2002, Vol. 3, p. 307
- CHOI, I.-S., and KIM, H.-T.: 'One dimensional evolutionary programming-based CLEAN', *Electron. Lett.*, 2001, 37, (6), pp. 400-401
- TRINTINALIA, L.C., and LING, H.: 'Joint time-frequency ISAR using adaptive processing', *IEEE Trans. Antennas Propag.*, 1997, 45, (2), pp. 221-227
- MOORE, I., and LING, H.: 'Super-resolved time-frequency analysis of wideband backscattered data', *IEEE Trans. Antennas Propag.*, 1995, 43, (6), pp. 623-626
- WEILE, D.S., and MICHELSEN, E.: 'E-plane microwave filters: community genetic algorithm optimization' in RAHMAT-SAMIL, Y., and MICHELSEN, E. (Eds.): 'Electromagnetic optimization by genetic algorithms' (John Wiley & Sons, New York, 1999), pp. 324-343
- WANG, H.T.G., SANDERS, M.L., and WOO, A.: 'Radar cross section measurement data of VFY 218 configuration', Naval Air Warfare Center, China Lake, CA, USA, Tech. Rep. NAWCWPNS TM07621, 1994

400 mW uncooled MiniDIL pump modules

S. Mohrdiek, T. Pliska, R. Bättig, N. Matuschek,
B. Valk, J. Troger, P. Mauron, B.E. Schmidt,
I.D. Jung, C.S. Harder and S. Enoch

A new generation of wavelength stabilised, uncooled 980 nm pump modules in MiniDIL housings is presented, enabling 400 mW ex-fibre power over a temperature range of 10°C to 70°C . At 100°C 200 mW power is still obtained with a robust fibre coupling scheme.

Introduction: As the focus in optical telecommunications systems turns more towards affordability, there is a push to produce EDFAs of lower cost, smaller size and less power consumption. Operation of 980 nm pump modules without a thermo-electric cooler (TEC) has been presented in [1]. The removal of the bulky and power-consuming TEC allowed us to develop pump modules in a smaller, less expensive MiniDIL housing. Though low cost is crucial, performance and reliability comparable to conventional Butterfly-type modules has to be demonstrated, in order to satisfy the yet stringent requirements for metro systems.

In this Letter we present results of 550 mW fibre coupled power at 25°C , 400 mW at 70°C and 200 mW at the extreme temperature of 100°C , with MiniDIL modules incorporating the latest developments in pump laser devices [2, 3] and wavelength stabilisation by fibre Bragg gratings (FBGs) [4]. Little change in fibre coupling efficiency with temperature demonstrates the robustness of the fibre alignment scheme.

Application of adaptive chirplet representation for ISAR feature extraction from targets with rotating parts

J. Li and H. Ling

Abstract: The problem of feature extraction from inverse synthetic aperture radar (ISAR) data collected from targets with rotating parts is addressed. In traditional ISAR imaging, rigid-body motion is usually assumed. When non-rigid-body motions are present, it is not possible to obtain a focused image of both the target and the rotating part. To solve this problem, the radar signal is first parameterised using the adaptive chirplet signal representation. The signal from the body and that from the rotating part are then separated in the parameter space. Point-scatterer simulation results show that better geometrical features of the body and better micro-Doppler features of the rotating part can be extracted after the separation. The algorithm is also demonstrated using the measurement data from an in-flight aircraft and a walking person.

1 Introduction

Recently, there has been increasing interest in studying the so-called micro-Doppler phenomenon [1, 2] for radar target identification applications. Micro-Doppler is used to describe the fine Doppler feature from some moving part on the target that is different from the main body Doppler feature. In most of the conventional work on inverse synthetic aperture radar (ISAR) imaging, the target is assumed to have rigid-body motion [3, 4]. However, non-rigid-body targets can often be found in real-world situations. As a simple case, a target may consist of a main body and a rotating part. For example, an in-flight aircraft with jet engine rotation, a ship with scanning antenna motion and a ground vehicle with spinning tyre motion all involve this type of configuration. Under these conditions, difficulties in understanding the resulting ISAR image arise due to the violation of the rigid-body assumption.

In this paper, we set out to extract better target features from ISAR data when a target has a rotating part beside the main body. The challenge is that the body image is contaminated due to the interference from the rotating part. It is also more difficult to extract the motion information from the rotating part as it is overshadowed by the body returns. Our approach is to first parameterise the radar signal using the adaptive chirplet representation [5, 6]. The chirplet basis is a four-parameter function localised in the joint time-frequency plane. While both Gaussian [7] and chirp-type [8] bases have been reported for joint

time-frequency processing of ISAR data, the chirplet basis is selected to represent the radar signal in this paper. Since both amplitude modulation (AM) and frequency modulation (FM) are part of the basis, the chirplet can more efficiently represent the radar signal from a target with a rotating part. With the adaptive chirplet representation, different motion behaviours of the target components are mapped into different parameters of the corresponding bases. Consequently, the returns from the body and the rotating part can be more easily separated. After the separation, better target feature extraction can be realised by processing the two parts individually. This includes both the extraction of the geometrical features from the main body and the micro-Doppler features from the moving part.

In the following section, we present the model and formulation of the problem. After a close examination of the point-scatterer signal model of a target with individual motions, we show that the chirplet basis is well suited for parameterising and separating the rotating part signal from the main body signal. The chirplet-based adaptive signal representation algorithm is tested with point-scatterer simulation data and results are shown from two sets of measurement data. The first data set is from an in-flight aircraft with jet engine rotation motion. The second data set is from a walking person with arm swinging motion.

2 Signal model and formulation

2.1 Point-scatterer model of radar signal from target with rotating part

The point-scatterer model is usually used in radar imaging to model the radar signal scattered by an unknown target. In this model, the radar return signal is expressed as a sum of point-scatterer responses

$$E(f, t) = \sum_{m=1}^M \sigma_m \exp \left\{ -j \frac{4\pi f}{c} [R_m(t) + x_m \cos \theta_m(t) + y_m \sin \theta_m(t)] \right\} \quad (1)$$

© IEE, 2003

IEE Proceedings online no. 20030729

doi: 10.1049/ip-rsn:20030729

Paper first received 31st January and in revised form 6th June 2003

J. Li is with the Department of Electrical Engineering, The University of Texas-Pan American, Edinburg, TX 78539, USA

H. Ling is with the Department of Electrical and Computer Engineering, The University of Texas at Austin, Austin, TX 78712, USA

where the radar signal E is a two-dimensional function of transmitting radar frequency f and pulse dwell time t . The target consists of M point-scatterers, each with position (x_m, y_m) and complex scattering coefficient σ_m . Suppose the radar is stationary, the target motion is described by the translation motion $R_m(t)$ and the angular motion $\theta_m(t)$ for each scatterer.

A rigid-body target is usually assumed in traditional ISAR imaging, i.e. all the point-scatterers in (1) share the same translation motion $R_m(t)$ and rotational motion $\theta_m(t)$. Here, we shall consider a non-rigid-body target consisting of two parts, a main body and a rotating part. In this case, we can simplify the model in (1) by using different motions for the two parts while still applying the rigid-body assumption for each part. This leads to

$$\begin{aligned} E(f, t) &= E_B(f, t) + E_R(f, t) \\ &= \sum_{m=1}^M \sigma_m \exp \left\{ -j \frac{4\pi f}{c} [R_B(t) + x_m \cos \theta_B(t) \right. \\ &\quad \left. + y_m \sin \theta_B(t)] \right\} + \sum_{n=1}^N \sigma_n \exp \left\{ -j \frac{4\pi f}{c} [R_R(t) \right. \\ &\quad \left. + x_n \cos \theta_R(t) + y_n \sin \theta_R(t)] \right\} \end{aligned} \quad (2)$$

with subscripts B and R denoting the body and the rotating part, respectively.

Both the main body and the rotating part move with respect to the radar. The difference is that the rotating part has an additional rotation motion beside all the motions of the main body. For the main body, during the imaging interval we can apply the small-angle approximation usually used in ISAR imaging. That is

$$\begin{cases} \cos \theta_B(t) \approx 1 \\ \sin \theta_B(t) \approx \theta_B(t) \end{cases} \quad (3)$$

We also assume that a standard motion compensation algorithm [4, 9, 10] has been utilised to remove both the translation motion and the nonuniform rotational motion from the body, after which we can write

$$\begin{cases} R_B(t) \leftarrow 0 \\ \theta_B(t) \leftarrow \omega_B t \end{cases} \quad (4)$$

where ω_B is the effective body rotation rate after the motion compensation. The arrow symbol above is used to indicate a new assignment of the variable on the left after the motion compensation operation.

For the rotating part, the motion relative to the main body is rotation only. This implies that the rotating part has the same translation motion as that of the body while the rotation motion will change accordingly, i.e.

$$\begin{cases} R_R(t) \leftarrow 0 \\ \theta_R(t) \leftarrow \theta_k^l(t) \end{cases} \quad (5)$$

However, the small-angle approximation does not hold for the rotating part. Since its rotation rate is usually much larger than that of the main body, a rotating scatterer might undergo many cycles while the main body rotates only a few degrees during the imaging interval. Substituting (3)–(5) into (2), we have

$$\begin{aligned} E(f, t) &= \sum_{m=1}^M \sigma_m \exp \left\{ -j \frac{4\pi f}{c} [x_m + y_m \omega_B t] \right\} \\ &\quad + \sum_{n=1}^N \sigma_n \exp \left\{ -j \frac{4\pi f}{c} [x_n \cos \theta_R^l(t) + y_n \sin \theta_R^l(t)] \right\} \end{aligned} \quad (6)$$

which is the radar signal from a target with a rotating part in the two-dimensional (frequency, dwell time) domain after motion compensation of the main body. Since it is more efficient to process range compressed data, we Fourier transform (6) with respect to f and bring the radar data into the (range, dwell time) domain. The radar signal through a fixed range cell r is given by

$$\begin{aligned} E_r(t) &= \sum_{m=1}^M \sigma_m f_{bw} \text{sinc} \left[\frac{2\pi f_{bw}}{c} (r - x_m) \right] \\ &\quad \times \exp \left\{ +j \frac{4\pi f_c}{c} (r - x_m - y_m \omega_B t) \right\} \\ &\quad + \sum_{n=1}^N \sigma_n f_{bw} \text{sinc} \left\{ \frac{2\pi f_{bw}}{c} [r - x_n \cos \theta_R^l(t) \right. \\ &\quad \left. - y_n \sin \theta_R^l(t)] \right\} \exp \left\{ +j \frac{4\pi f_c}{c} [r - x_n \cos \theta_R^l(t) \right. \\ &\quad \left. - y_n \sin \theta_R^l(t)] \right\} \end{aligned} \quad (7)$$

where f_c and f_{bw} are the carrier frequency and the bandwidth of the radar, respectively.

Some observations can be made here about (7). There exist substantial differences between the main body signal and the rotating part signal. Each body-scatterer in the first term has constant amplitude σ_m and constant Doppler frequency $-(2f_c/c)\omega_B y_m$ with respect to t . However, the signal of each rotating scatterer in the second term contains both AM and FM components. This can be seen by the presence of the time-varying function $\theta_R^l(t)$ in both the *sinc* and the exponential terms. Consequently, a second Fourier transform of (7) with respect to t will focus the target body in cross-range, but not the rotating part return. This results in the observed interference from the rotating part in the ISAR image.

2.2 Chirplet basis

The chirplet basis function [5, 6] is well suited for parameterising the AM-FM radar signal in (7). A chirplet is a four-parameter basis of the form

$$\begin{aligned} h_k(t) &= \left(\frac{\pi}{\alpha_k} \right)^{\frac{1}{4}} \exp \{ -\alpha_k (t - t_k)^2 \} \exp \{ -j2\pi f_k (t - t_k) \\ &\quad - j\pi \beta_k (t - t_k)^2 \} \end{aligned} \quad (8)$$

where t_k is the time centre of the signal, f_k is the centre frequency, β_k is the frequency modulation rate and α_k defines the time extent of the signal. The joint time-frequency plot of a chirplet function is illustrated in Fig. 1a.

Actually, the chirplet basis is one of the many options that can be used to model the radar signal accurately. However, there are some attractive attributes of this basis. First, the basis function is an AM-FM signal and only a sparse set of these bases is needed to approximate the time-frequency structure of the radar signal in (7). Secondly, the chirplet basis is a well understood basis with only four parameters. Only moderate computation time is needed to search for the basis parameters. Thirdly and most importantly, the parameters of the chirplet can be used to separate the two components of the signal. This is because signals from the main body and the rotating part are captured by chirplet bases with different parameters.

To see this more explicitly, let us assume a first-order rotational motion in the time neighbourhood of each chirplet

$$\theta_R^l(t) = \theta_c + \omega_R (t - t_k) \quad (9)$$

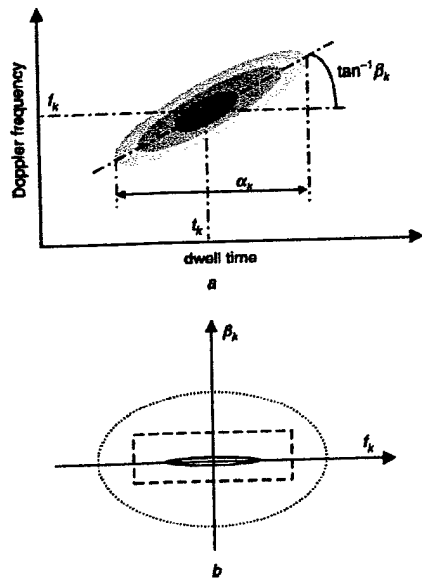


Fig. 1 Chirplet basis and chirplet parameters

a Joint time-frequency representation of a chirplet basis
b Distribution of chirplet parameters for the main body (solid) and rotation parts (dotted) and separation thresholds (dashed)

where θ_c is the angle at the time centre. The rotating part is assumed to have a constant rotation rate ω_R during the time interval near t_k although it could have more complex motions during the whole imaging interval.

After substituting (9) into (7), we take the first and second derivatives of the phase term with respect to t and compare them to those from (8) to arrive at expressions for f_k and β_k . The results can be written as

$$f_k = -\frac{2f_c}{c} \omega_R [x_n \sin \omega_R(t - t_k) - y_n \cos \omega_R(t - t_k)]$$

$$= -\frac{2f_c}{c} l_n \omega_R \sin[\omega_R(t - t_k) - \zeta_n] \quad (10a)$$

$$\beta_k = -\frac{2f_c}{c} l_n \omega_R^2 \cos[\omega_R(t - t_k) - \zeta_n] \quad (10b)$$

where (l_n, ζ_n) are the polar representations of (x_n, y_n) . It can be seen from (10a) and (10b) that the parameters f_k and β_k are distributed along an ellipse as follows:

$$\frac{f_k^2}{(l_n \omega_R)^2} + \frac{\beta_k^2}{(l_n \omega_R^2)^2} = \left(\frac{2f_c}{c}\right)^2 \quad (11)$$

where the size and the axial ratio of the ellipse are controlled by ω_R and l_n . Similarly, the equation to associate the chirplet parameters with the main body signal is given by

$$\frac{f_k^2}{(l_m \omega_B)^2} + \frac{\beta_k^2}{(l_m \omega_B^2)^2} = \left(\frac{2f_c}{c}\right)^2 \quad (12)$$

where the scatterer radial length l_m and the rotation rate ω_B are used for the main body.

Even though (11) and (12) have exactly the same form, the main body and the rotating part are separable in the parameter space because of their different motions. Essentially, while the sizes of the two parts are comparable, the rotating part rotates much faster than the main body during the imaging interval, i.e.

$$\omega_R \gg \omega_B \quad (13)$$

Consequently, the chirplet parameters f_k and β_k for the main body and the rotating part are distributed very differently in the parameter space. A rotating part scatterer is represented as a larger and rounder ellipse while a body-scatterer is represented as a smaller and flatter ellipse. Actually, the ellipse for the main body is nearly a line segment on the f_k axis since the first term of (7) is assumed to have zero Doppler rate. The different distributions of the chirplet parameters are illustrated in Fig. 1b, where the outer ellipse represents the rotating part signal while the inner one represents the main body signal. A simple criterion to separate the two parts can thus be defined; the body signal has small f_k and β_k while the rotating part signal has either large f_k or β_k .

Another interesting observation we can make from the above discussion is that the main body and the rotating part signals have large overlaps in f_k , while they have little overlap in β_k . Therefore, the Doppler rate is more important than the Doppler frequency in separating the two signal components. This point will be further illustrated by examples later.

To summarise, if we parameterise the radar signal in question into a set of chirplet bases, it is possible to separate the contributions from the target body and the rotating part based on the parameters of the chirplet bases, as we have discussed above.

2.3 Signal separation based on adaptive chirplet signal representation

To decompose the radar signal into a set of chirplet bases, we apply the adaptive signal parameterisation algorithm [11, 12]. We start with the radar signal in a fixed range cell with returns from both the body and the rotating part, which is labelled as $E_r(t)$ in (7). Next, we parameterise $E_r(t)$ by projecting the signal onto chirplet bases of different parameters and find the one with the maximum projection value. Next, a residual signal is generated by subtracting the contribution of the just-found basis from the signal. This process is then iterated to generate a series of chirplet basis functions that, when summed, can approximate the original signal. The steps are summarised below:

Step 1. Set iteration index number k to 1 and the residual signal $R_k(t)$ to $E_r(t)$

Step 2. Find the k th chirplet $h_k(t)$ by maximising the projection from the residual signal $R_k(t)$ onto the basis, i.e.

$$\{t_k, f_k, \alpha_k, \beta_k\} = \arg \max |\langle R_k(t), h_k(t) \rangle| \quad (14)$$

where the inner product is defined as

$$\langle R_k(t), h_k(t) \rangle = \int_{t_0}^{t_1} R_k(t) h_k^*(t) dt \quad (15)$$

The radar data are assumed to exist over the time interval t_0 to t_1 . The coefficient of the chirplet is the corresponding projection

$$c_k = \langle R_k(t), h_k(t) \rangle \quad (16)$$

Step 3. Subtract the extracted signal from the residual

$$R_{k+1}(t) \leftarrow R_k(t) - c_k h_k(t) \quad (17)$$

Step 4. Increment k by one and repeat steps 2 and 3 until k reaches a preset number or until the energy of the residual signal is below some threshold set based on the signal-to-noise ratio. Suppose N chirplets are found from this procedure, the radar signal is parameterised as

$$E_r(t) \approx \sum_{k=1}^N c_k \left(\frac{\pi}{\alpha_k} \right)^{\frac{1}{4}} \exp \left\{ -a_k(t-t_k)^2 e^{-j2\pi f_k(t-t_k)} e^{-j\pi \beta_k(t-t_k)^2} \right\} \quad (18)$$

After the parameterisation of the radar signal, the body signal can be separated from the rotating part signal using the criteria discussed previously. We classify those chirplets with small f_k and β_k as the main body components and the chirplets with either large f_k or large β_k as the rotating part components. The final body-only signal and the rotating part signal are assembled from the corresponding chirplet bases according to (18).

Following the separation, we can process the main body signal and the rotating part signal individually for better information extraction. Based on our discussion about (7), for the target body the feature of interest is the geometrical information in the ISAR image. A better body image can be reconstructed after removing the rotating part components. For the rotating part signal, it may be impossible to also construct a focused image of the rotating part if the PRF of the radar is too low. However, it is possible to extract useful information about the motion of the rotating part from the separated data.

3 Point-scatterer simulation results

We first test our algorithm with point-scatterer simulation data. Six point-scatterers are used in the simulation with five points representing the rigid body and one representing the rotating part. The positions and the strengths of the six scatterers are shown in Fig. 2. Scatterer 6 rotates around scatterer 2 at a rate of 6.67 Hz and a rotation radius of 20 cm. We assume the radar has a 10 GHz centre frequency, 800 MHz bandwidth and 1400 Hz PRF. The target body rotates about 4° over 384 pulses during the data collection time.

Simulated radar data are generated using the point-scatterer model in (6). The resulting radar image is shown in Fig. 3. The three point-scatterers in the centre range cell are shadowed by a noisy vertical micro-Doppler band due to the motion of the rotating point-scatterer. Our objective is to reconstruct the five body-scatterers and to estimate the rotation rate of the rotating scatterer from the radar signal.

Different behaviours of the body and the rotating part are better identified in the joint time-frequency

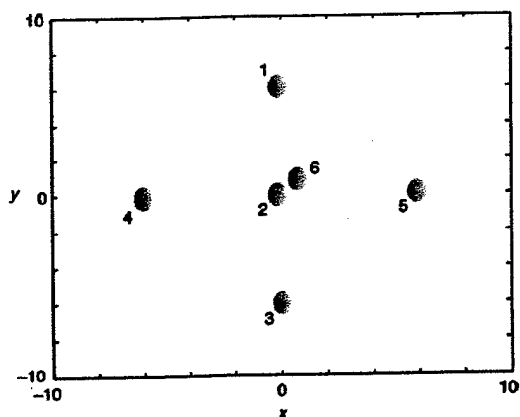


Fig. 2 Point-scatterer representation of the original target consisting of five rigid points (1–5) and one rotating point (6) with strengths 2, 5, 2, 1, 1, and 3.33, respectively

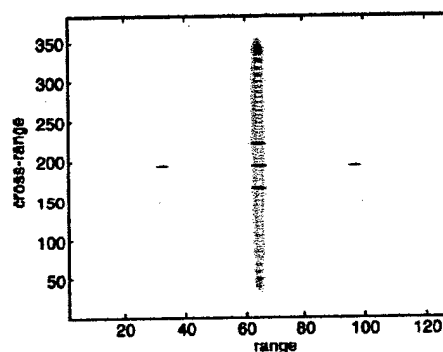


Fig. 3 Simulated ISAR image of the target with non-rigid-body motion

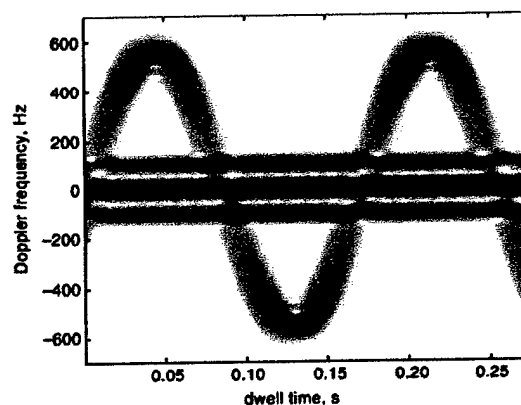


Fig. 4 Spectrogram of the radar signal through range cell 65

domain. The spectrogram obtained from the short-time Fourier transform is shown in Fig. 4 using the data in range cell 65, which contains responses from scatterers 1, 2, 3 and 6. In this Figure, we see interesting features about the target. First, there are three horizontal Doppler lines. The one at zero Doppler is due to scatterer 2. The two at ± 100 Hz are due to scatterers 1 and 3. Secondly, there is a sinusoidal-like micro-Doppler curve due to the rotating scatterer 6. Amplitude modulation of this signal is also observed.

Following the steps in Section 2.3, we first parameterise the signal using $N = 100$ chirplets. The spectrogram of the resulting parameterised signal is shown in Fig. 5. We see fairly good agreement between the original signal and the parameterised signal. Next, we separate the contributions from the static and dynamic parts of the target based on the Doppler frequency f_k and the Doppler rate β_k of the chirplet bases. A simple threshold of 3200 Hz/s on the Doppler rate and 300 Hz on the Doppler frequency is used to discriminate the static and dynamic part of the target. The spectrograms of the resulting radar signals are shown in Figs. 6a and 6b for the rigid body and the rotating part, respectively. We see that the body with nearly constant Doppler and the rotating part with fast changing Doppler are separated.

We use the same procedure to parameterise and separate the radar signals from range cells 60 to 70. After removing the rotating part interference, the final ISAR image is shown in Fig. 7. The five scatterers of the static body are now correctly focused. To obtain more

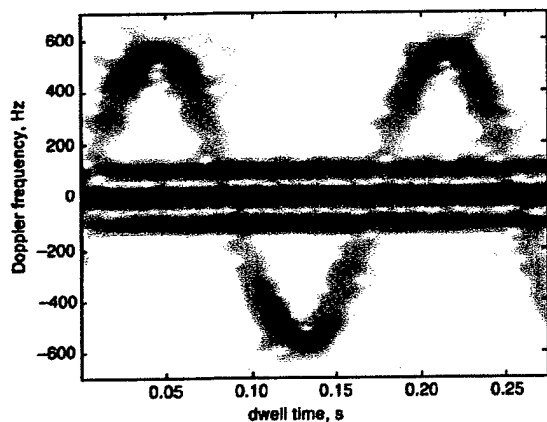


Fig. 5 Spectrogram of the parameterised radar signal using 100 chirplet bases

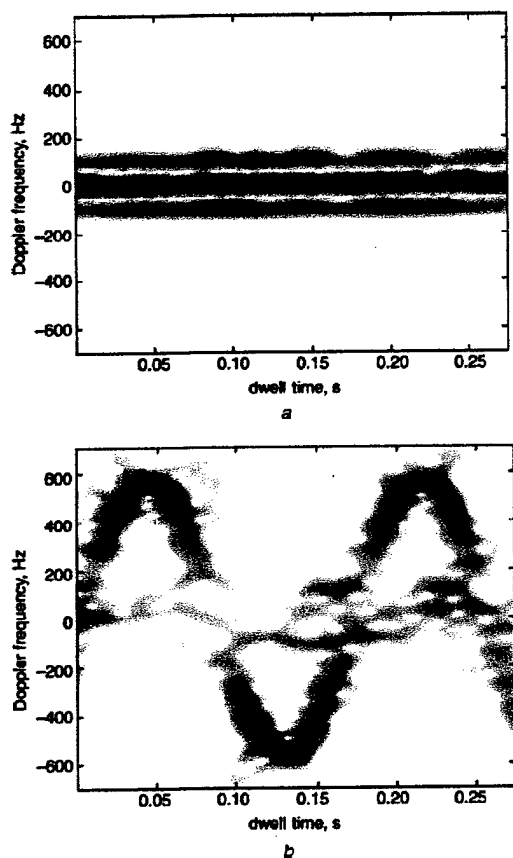


Fig. 6 Separated body and rotating part signal
a Spectrogram of the three main body scatterers
b Spectrogram of the rotating part

information about the rotation motion, an autocorrelation analysis of the separated rotating point signal is shown in Fig. 8a. The period of the rotation motion is determined to be 0.15 s from this Figure. This agrees with the true rotation rate of 6.67 Hz. For comparison, the autocorrelation of the raw radar signal before separation is shown in Fig. 8b. It is difficult to detect the periodicity from the plot as the rotating scatterer signal is heavily contaminated by the large body return.

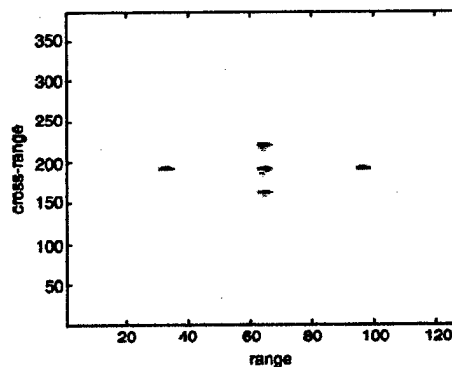


Fig. 7 Reconstructed ISAR image using the main body signals only

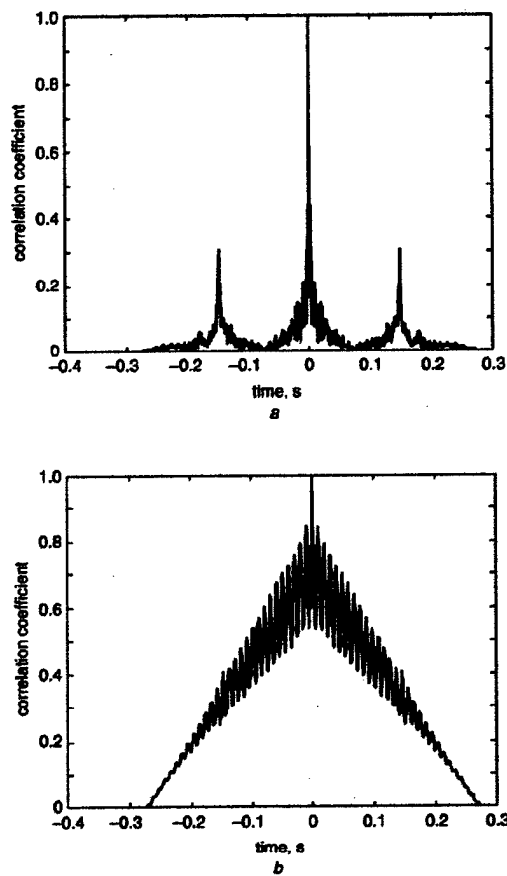


Fig. 8 Rotation rate estimation using autocorrelation
a Result from the rotating part signal after separation
b Result from the original signal before separation

4 Measurement data results

The algorithm is next applied to two sets of measurement data. The first data set is the radar data collected from an in-flight aircraft during the frontal view of the target. The second data set is the radar data collected from a walking person. In both cases, the goal is to separate the main body signal from the rotating part return for better target feature extraction.

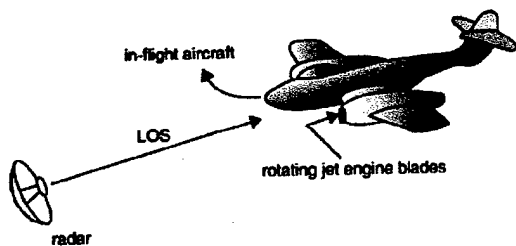


Fig. 9 ISAR imaging of an aircraft during frontal view

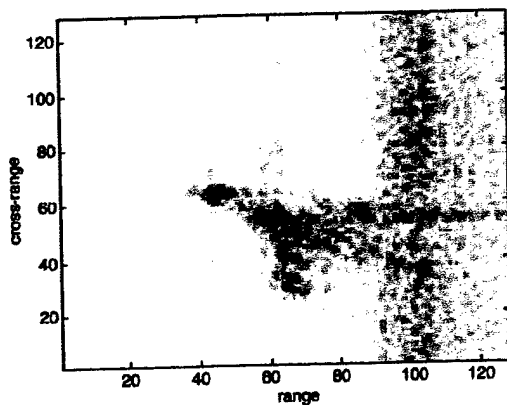


Fig. 10 ISAR image of the aircraft with JEM lines

4.1 Jet engine modulation removal from an in-flight aircraft

The geometry of the problem is shown in Fig. 9. The radar collects backscattering data from an in-flight aircraft. The resulting ISAR image obtained using a joint time-frequency based motion compensation algorithm [9] is shown in Fig. 10. We observe a vertical noisy band due to the rotating engine blades, which is the well known jet engine modulation (JEM) phenomenon [13]. The geometry of the aircraft body is obscured due to the presence of the JEM lines.

Simple Doppler gating is typically used to alleviate this problem. The result in Fig. 11a is generated by putting zeros in cross-range cells 1–32 and 62–128 in the image area with JEM lines. The high Doppler frequency components in the jet engine return are removed in this manner. However, we see that in areas where the JEM lines overlap with the target image, this technique does not work well, as it cannot distinguish the aircraft body signal from the JEM signal with low Doppler frequency.

Using the chirplet-based adaptive signal representation, we first parameterise the radar signal. Figure 11b is the reconstructed ISAR image using a separation criterion based on β_k only, i.e. we remove those chirplet bases with large β_k from the parameterised signal. It is much better than Fig. 11a in revealing the aircraft body feature. This confirms our previous observation that the Doppler rate is a better discriminator than the Doppler frequency in separating the two signals. Finally, we use both β_k and f_k to separate the two signals. The aircraft body image reconstructed from chirplet bases with both small β_k and small f_k is shown in Fig. 11c. We see an even better representation of the aircraft

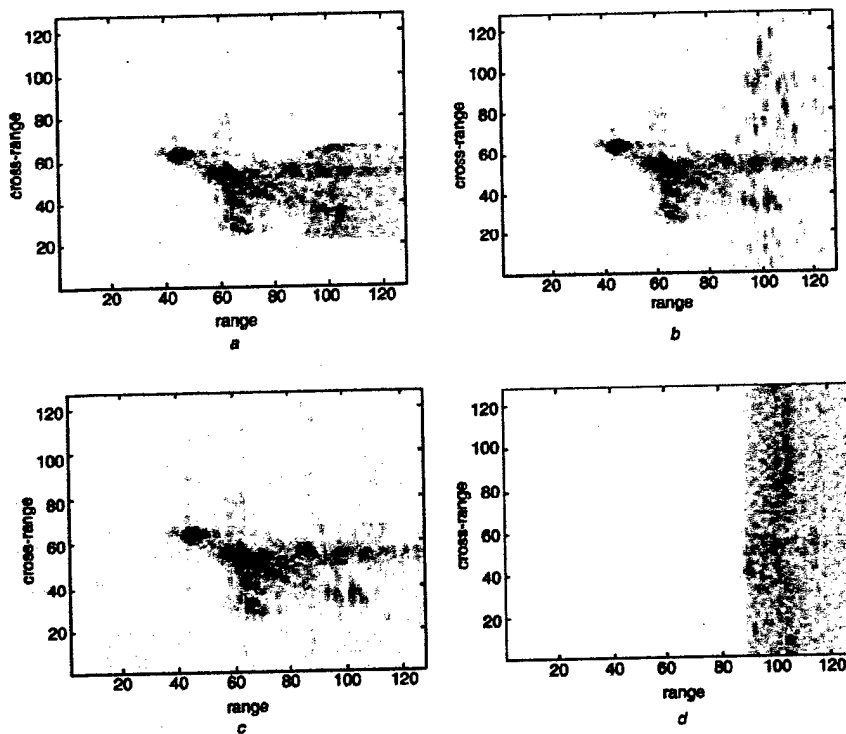


Fig. 11 Aircraft body and JEM line separation

- a Body ISAR image with Doppler frequency gating only
- b Body ISAR image with Doppler rate gating only
- c Body ISAR image based on both Doppler frequency and Doppler rate parameters
- d Separated JEM signal

body feature in the JEM region. The JEM signal is also displayed in Fig. 11d. The signal is aliased because of the low PRF of the radar in comparison with the rotation rate of the engine blades. This example shows that this algorithm works despite the strong Doppler aliasing of the rotating part signal.

4.2 Arm swing rate estimation from a walking person

The second data set is the measured radar data collected from a walking person. The geometry of the problem is shown in Fig. 12. Two types of motions are involved; the translation motion of the person's body and the swinging motion of the arms (or legs). Figure 13 shows the range profiles after coarse range alignment using amplitude correlation. Due to the limited range resolution relative to the target size, it is very hard to discern any useful features about either the body or the arms in this Figure. Figure 14 is the spectrogram of the radar signal through range cell 32. Interesting target features are revealed in this Figure. The horizontal Doppler line is due to the body motion as the person walks at a relatively constant speed during the 1.28 s dwell interval. The sinusoidal-like curve shows the micro-Doppler phenomenon from the swinging arm motion. The Doppler spread is caused by the varying speed of the arm and the changing angle between the instantaneous swinging motion and the radar incident wave. We also observe the periodicity of the arm motion.

To separate the body and the arm returns, the adaptive chirplet representation is applied. After the parameterisation, we again separate the body return from the arm return by classifying those bases with large Doppler frequency f_k or large Doppler rate β_k as contributions from the arms. The spectrograms of the separated body and arm signals are shown in Figs. 15a and 15b, respectively. The main features of the target are kept after the separation, indicating good accuracy of the parameterisation. We also observe a significant denoising effect from the parameterisation. This is because noise in the measured data does not have the time-frequency characteristics of a chirplet and it is left

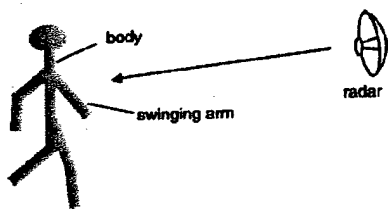


Fig. 12 ISAR imaging of a walking person

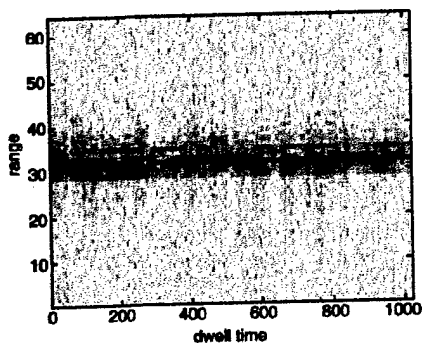


Fig. 13 Radar data after range compression

in the residual signal after the parameterisation. The arm-swing period can be easily estimated from the arm-only data by taking the autocorrelation of the time sequence. The peaks in Fig. 16a correspond to the period of the signal, which is found to be 0.44 s. Based on this swing rate and the speed of the person (2.3 m/s) estimated from the same radar data, the stride size of the person is determined to be about 1.0 m. For comparison, we have also generated the autocorrelation of the original data without the joint time-frequency processing (Fig. 16b). In this case, the radar return from the arm is overshadowed by the body

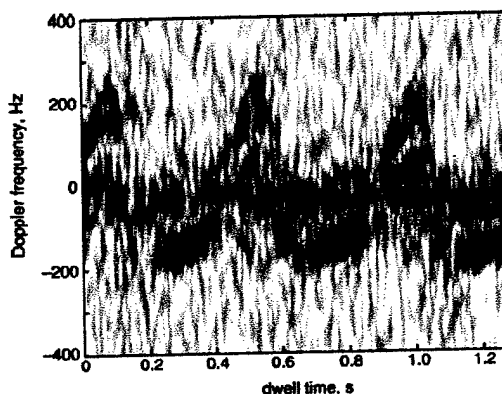


Fig. 14 Spectrogram of the radar signal containing body and arm components

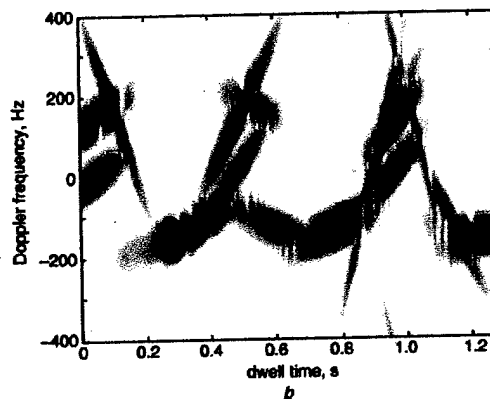
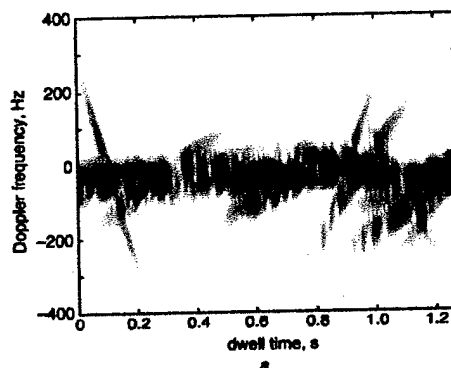


Fig. 15 Separated signal components

a Body
b Swinging arm

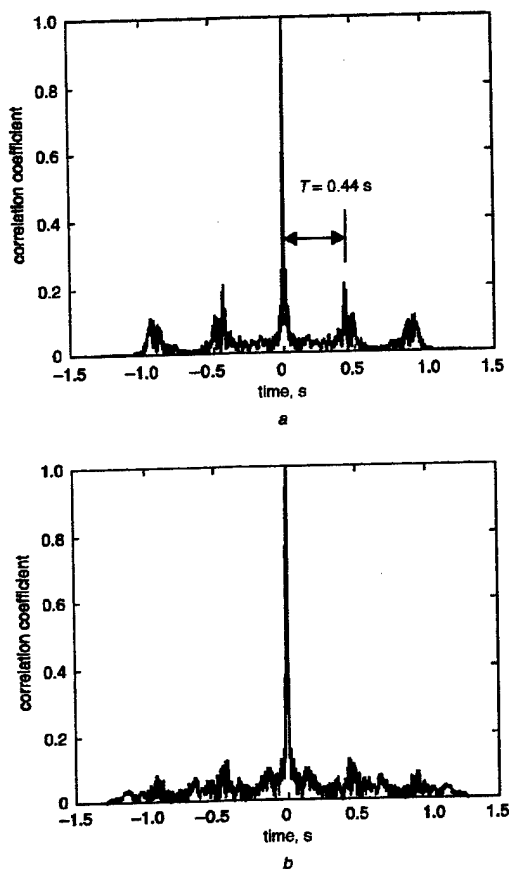


Fig. 16 Arm-swing rate estimation using autocorrelation

a After signal separation
b Before signal separation

return and the peaks in the autocorrelation function are significantly less pronounced.

Finally, we note here that only a simple exhaustive search has been implemented to carry out the chirplet decomposition in our examples. In the walking person example, the decomposition of a signal with 1024 data samples into 50 chirplets took 1050 s using MATLAB on a personal computer with a 2.26 GHz Pentium 4 CPU. A fast implementation of the chirplet decomposition has recently been reported in [14] and should speed up the processing significantly.

5 Conclusions

In this paper, a chirplet-based adaptive signal representation algorithm has been applied to extract features from ISAR data of a target with a rigid main body and a rotating part. Because the micro-Doppler feature of the rotating part is very different from the body Doppler, the two interfere with each other if processed together. To overcome this problem,

we parameterise and separate the two parts using the adaptive signal representation. In particular, after formulating an AM-FM model for the radar signal, the four-parameter chirplet basis is used to account for the time and frequency localisation of the signal. After the parameterisation, the separation is achieved by a criterion based on the extracted Doppler frequency and Doppler rate parameters. The algorithm has been successfully tested with point-scatterer simulations and applied to two measurement data sets. In the aircraft data, we are able to reconstruct a better aircraft body image after the separation. In the walking person data, we are able to more accurately estimate arm swing rate. The results demonstrate the potential application of this algorithm for target identification using ISAR data from non-rigid-body targets.

6 Acknowledgments

This work is supported by the Office of Naval Research under contract No. N00014-98-1-0615. The authors also thank Dr. V.C. Chen of Naval Research Laboratory for providing the measurement data used in this work. In addition, J. Li gratefully acknowledges summer support from the Computing and Information Technology Center at the University of Texas-Pan American.

7 References

- Chen, V.C.: 'Analysis of radar micro-Doppler with time-frequency transform', Proc. 10th IEEE Workshop on Statistical signal and array processing, Pocono Manor, PA, USA, Aug. 2000, pp. 463-466.
- Greiner, E.F., Geisheimer, J.L., and Asbell, D.: 'Extraction of micro-Doppler data from vehicle targets at X-band frequencies', *Proc. SPIE-Int. Soc. Opt. Eng.*, 2001, **4374**, pp. 1-9.
- Ausherman, A., Kozma, A., Waker, J.L., Jones, H.M., and Poggio, E.C.: 'Developments in radar imaging', *IEEE Trans. Aerosp. Electron. Syst.*, 1984, **20**, (4), pp. 363-400.
- Carrara, W.G., Goodman, R.S., and Majewski, R.M.: 'Spotlight synthetic aperture radar - Signal processing and algorithms' (Artech House, Boston, MA, 1995).
- Qian, S., Chen, D., and Yin, Q.: 'Adaptive chirplet based signal approximation', Proc. ICASSP, Seattle, WA, USA, May 1998, vol. III, pp. 1871-1874.
- Bultan, A.: 'A four-parameter atomic decomposition of chirplets', *IEEE Trans. Signal Process.*, 1999, **47**, pp. 731-745.
- Trintinalia, L.C., and Ling, H.: 'Joint time-frequency ISAR using adaptive processing', *IEEE Trans. Antennas Propag.*, 1997, **45**, (2), pp. 221-227.
- Wang, Y., Ling, H., and Chen, V.C.: 'Application of adaptive joint time-frequency processing to ISAR image enhancement and Doppler feature extraction for targets with rotating parts', *Proc. SPIE-Int. Soc. Opt. Eng.*, 1998, **3462**, pp. 156-163.
- Wang, Y., Ling, H., and Chen, V.C.: 'ISAR motion compensation via adaptive joint time-frequency techniques', *IEEE Trans. Aerosp. Electron. Syst.*, 1998, **34**, (2), pp. 670-677.
- Rihaczek, A.W., and Hershkowitz, S.J.: 'Radar resolution and complex-image analysis' (Artech House, Boston, MA, 1996).
- Mallat, S.G., and Zhang, Z.: 'Matching pursuits with time-frequency dictionaries', *IEEE Trans. Signal Process.*, 1993, **41**, (12), pp. 3397-3415.
- Qian, S., and Chen, D.: 'Signal representation using adaptive normalized Gaussian functions', *Signal Process.*, 1994, **36**, (1), pp. 1-11.
- Bell, M., and Grubbs, R.A.: 'JEM modeling measurement for radar target identification', *IEEE Trans. Aerosp. Electron. Syst.*, 1993, **29**, (1), pp. 73-87.
- Yin, Q., Qian, S., and Feng, A.: 'A fast refinement for adaptive Gaussian chirplet decomposition', *IEEE Trans. Signal Process.*, 2002, **50**, (6), pp. 1298-1306.

A SYNTHETIC APERTURE ALGORITHM FOR GROUND-PENETRATING RADAR IMAGING

C. Ozdemir¹, S. Lim² and H. Ling²

¹ Dept. of Electrical-Electronics Engineering, Mersin University,
Ciftlikkoy, 33343 Mersin, TURKEY.

² Dept. of Electrical and Computer Engineering, the Univ. of Texas at Austin,
Austin, TX 78712-1084 USA.

A formulation for ground penetrating radar (GPR) imaging using synthetic aperture concept is introduced. We show that it is possible to form a 3D image by inverse Fourier transforming the multi-frequency, multi-spatial scattered field. The proposed algorithm for GPR imaging is tested with measured and simulation data. The resulting images demonstrate good agreement between the measured and simulated cases.

Introduction: The imaging of buried objects or inhomogeneities underground using ground penetrating radars (GPR) has been a topic of interest for a wide variety of applications ranging from mine detection to archeology. Many GPR imaging algorithms have been proposed in the literature [1-5]. Although good depth resolution can usually be realized in GPR images using frequency diversity, good resolution in the cross-range dimensions is much harder to achieve. Capineri et al. [3] proposed a method for obtaining good resolution in GPR images out of B-scan data by applying the Hough transformation technique. Morrow and Van Genderen [4] and Van Dongen et al. [5] applied the back propagation and conjugate gradient inversion techniques to form two-dimensional (2D) and three-dimensional (3D) images for a borehole radar. However, these techniques have significant computational burden. Therefore, there is a need for obtaining images with good range and cross-range resolution with a fast algorithm.

We have previously developed a synthetic aperture algorithm for imaging antenna-platform interactions based on multi-frequency, multi-spatial scattered field data [6-8]. In this paper, we extend our algorithm to generate 3D GPR images of scattered data from buried objects underground. This technique is based on the approximate Fourier transform

relationship between the frequency-spatial variables and the distance-angle information of the buried scatterer. The algorithm is quite attractive since it forms 3D images by using a fast Fourier transform (FFT) followed by a simple transformation from the distance-angle domain to the image domain. It is computationally fast. Furthermore, the cross-range resolution can be made as good as the range resolution by controlling the size of the collection aperture.

SAR Approach for GPR Imaging: Similar to the antenna synthetic aperture radar algorithm [6-8], our GPR imaging algorithm is based on collecting the multi-frequency scattered electric field over a two-dimensional spatial grid lying on top of the ground as shown in Fig. 1. We assume the target point P is located at an unknown location (x_i, y_i, z_i) . We also assume that the frequency bandwidth is small compared to the center frequency and that the aperture dimensions are small compared to R_{2i} , the path length from P to the receiver. Under these assumptions, the scattered electric field at the receiver can be approximated as follows:

$$E_s(k, x', z') = A_i \cdot e^{-jk(R_{1i} + R_{2i})} \cdot e^{-jk_c \cdot x' \sin \alpha_i} \cdot e^{-jk_c \cdot z' \sin \alpha_i \sin \beta_i} \quad (1)$$

where A_i is the strength of the scattered field, $k = 2\pi\sqrt{\epsilon_r} / \lambda$ is the wave number in the soil and ϵ_r is the relative permittivity of the ground. k is proportional to the radar frequency, and k_c corresponds to the wave number at the center frequency. By taking the 3D inverse Fourier transform of the scattered electric field with respect to k , x' and z' , it is possible to pinpoint the total travel distance and the angles related to the scatterer location as follows:

$$E_s(R, U, V) = A_i \cdot \delta(R - (R_{1i} + R_{2i})) \cdot \delta(U - \sin \alpha_i) \cdot \delta(V - \sin \alpha_i \sin \beta_i) \quad (2)$$

Here, we introduce three new variables $R = R_1 + R_2$, $U = \sin \alpha$ and $V = \sin \alpha \sin \beta$ for simplicity. Once an image in the (R, U, V) domain is generated, we can then transform it from the (R, U, V) into the spatial (x, y, z) domain by using the trigonometric relationship between the

variables (R, α, β) and (x, y, z) . The transformations from (R, U, V) to (x, y, z) is unique and correctly maps the scatterer location [8]. However, the resultant point spread response in the image is slightly distorted due to the nonlinear nature of the transformation.

Experimental Results: To test our GPR imaging algorithm, we built an experimental setup shown in Fig. 2. In this setup, a wooden pit was constructed and was filled with play sand. The dielectric constant of the sand was measured by comparing the phase delay between a pair of antennas in the air to that in the sand. The dielectric constant of the sand was found to be nearly constant at 2.26 for the frequency range from 5GHz to 6GHz. For our GPR experiment, a rectangular copper plate whose dimensions are 46cm in the x-direction and 30cm in the z-direction was buried at 46cm below the sand surface. The plate is located at 50cm away from the transmitter along the x-axis. The S_{21} between the transmitter and the receiver was measured using an HP8753C network analyzer. As the transmitter and the receiver antennas, identical coax-fed, rectangular waveguide antennas whose dimensions are 3.81cm and 1.91cm were used. The transmitter antenna was assumed to be placed at the origin and the receiving grid was assumed to be centered at 1m along the positive x-direction. Both antennas were horizontally polarized such that the electric field was parallel to the metal plate. The scattered field was collected over 100 different spatial points. The size of the 10-by-10 receiving grid was 31.04cm in the x-direction and 14.83cm in the z-direction. For all 100 points, the signal frequency varied from 4.9226 GHz to 5.9352 GHz over 25 evenly sampled points. The measured data from the experimental setup in Fig.2 were collected onto a computer and processed. After applying the proposed algorithm, we generated a 3D GPR image of the region below the surface. Fig.3 (a) shows the 2D projected GPR images onto the principal Z-Y, X-Y and X-Z planes. Overlaid on the images are the projected outlines of the plate. We observe two main hot spots in the image. The stronger one corresponds to the

scattering from the middle of the plate where a specular point exists. The weaker one corresponds to the diffraction mechanism from the front edge of the plate. Both image features agree well with the geometrical locations of the plate. In addition, resolutions in the cross range directions (i.e., in the x - and z -directions) are nearly the same as the resolution in the range (y) direction. Note that the spots in the image do not have a simple point spread form and they are somewhat defocused. This is due the non-linear transformation from the (R, α, β) to the (x, y, z) domain, and a method to overcome this effect has been discussed in [7, 8]. Nonetheless, we can still see the separation between the two points on the plate, which are spaced 23 cm apart. Therefore, our technique is able to achieve good resolutions in both the range and the cross-range dimensions.

Simulation was also carried out using a physical optics calculation. After obtaining the simulation data of the experimental setup, we applied the same imaging algorithm to form the simulated GPR image. Fig.3 (b) demonstrates the 2D projected GPR images from the simulation data. By comparing the measured GPR images to the simulated ones, we see good agreement between the two. Since the physical theory of diffraction contribution was absent in the simulation, we notice that the edge diffraction contribution in the simulation is weaker than that from the measured image. Finally, data were also collected and images formed using other non-metallic objects. High-resolution images could be formed consistently using the algorithm.

Conclusion: We presented a Fourier based imaging algorithm for ground penetrating radar based on the synthetic aperture radar concept. The algorithm uses the phase information of the scattered field. By inverse Fourier transforming the scattered field data, we have shown that it is possible to form high-resolution 3D GPR image of the region below the ground surface. To test our imaging algorithm, data were collected from a buried metallic plate using an

experimental setup. Our imaging algorithm successfully formed a 3D GPR image of the plate. The measured image was also compared to that formed from simulation data generated using the physical optics calculation. Good agreement between the measured and simulated images was observed. The limitation of the present imaging algorithm is that it assumes the soil medium to be homogeneous and the soil property is known a priori.

Aknowledgements: This work is supported by *the Scientific and Research Council of Turkey* (TUBITAK) under NATO-B2 research scholarship programme and in part by the Office of Naval Research under contract No. N00014-03-1-0021. The authors would also like to thank to Dr. Hosung Choo (now with Hongik University, Korea) for his help during the experiments.

References

- 1 DANIELS, D.J., *Surface-Penetrating Radar*, 1996, London: IEE Press.
- 2 MAST, J. E., LEE, H., and MURTHA, J. P., "Application of Microwave Pulse-Echo Radar Imaging to the Nondestructive Evaluation of Buildings," *Int. J. Imaging Syst. Tech.*, 1992, 4, pp. 164-169
- 3 CAPINERI, L., GRANDE, P., TEMPLE, J. A. G., "Advanced Image-Processing Technique for Real-Time Interpretation of Ground-Penetrating Radar Images," *Int. J. Imaging Syst. Tech.*, 1998, 9, (1), pp. 51-59
- 4 MORROW, I.L., and VAN GENDEREN, P, "A 2-D Polarimetric Backpropagation Algorithm for Ground-Penetrating Radar Applications," *Microwave Opt. Tech. Lett.*, 2001, 28, (1), pp. 1-4
- 5 VAN DONGEN, K.W.A., VAN DEN BERG, P.M. and FOKKEMA, J.T., "A Directional Borehole Radar for Three-Dimensional Imaging, *Proc. GPR 2002, Ninth Intern. Conf. on GPR*, 2002, I, Santa Barbara, USA, pp. 25-30
- 6 OZDEMIR, C., BHALLA, R., TRINTINALIA, L.C. and LING, H., "ASAR - Antenna Synthetic Aperture Radar Imaging," *IEEE Trans. Antennas Propagat.*, 1998, 46, (12), pp. 1845-1852
- 7 OZDEMIR, C., BHALLA, R., and LING, H., "A Radiation Center Representation of Antenna Radiation Patterns on a Complex Platform," *IEEE Trans. Antennas Propagat.*, 2000, 48, (6), pp. 992-1000
- 8 OZDEMIR, C. and LING, H., "ACSAR - Antenna Coupling Synthetic Aperture Radar (ACSAR) Imaging Algorithm," *J. Electromag. Waves App.*, 1999, 13, (3), pp. 285-306

List of Figures:

Figure 1. Geometry for GPR Imaging

Figure 2. Experiment setup.

Figure 3. 2D projected GPR images for (a) measurement data, (b) simulation data.

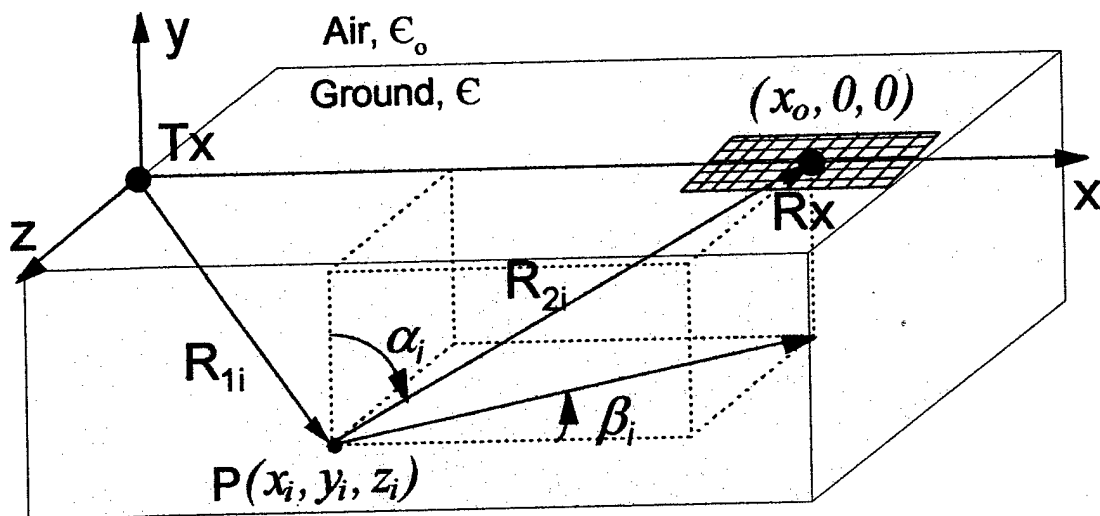


Figure 1. Geometry for GPR Imaging

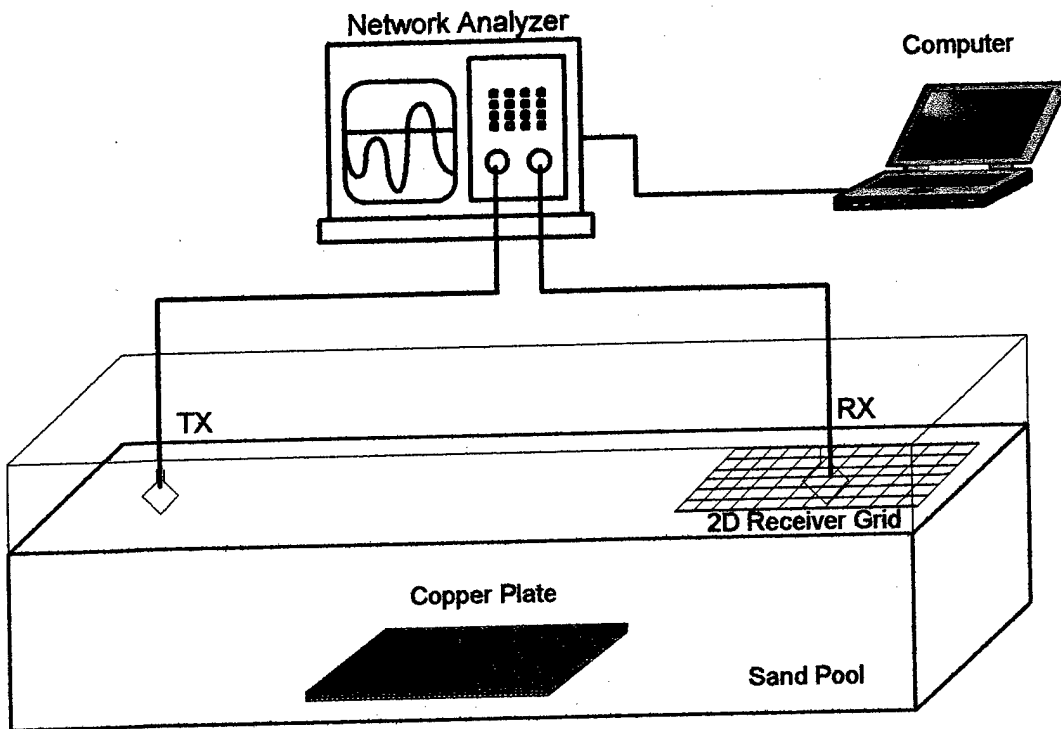


Figure 2. Experiment setup.

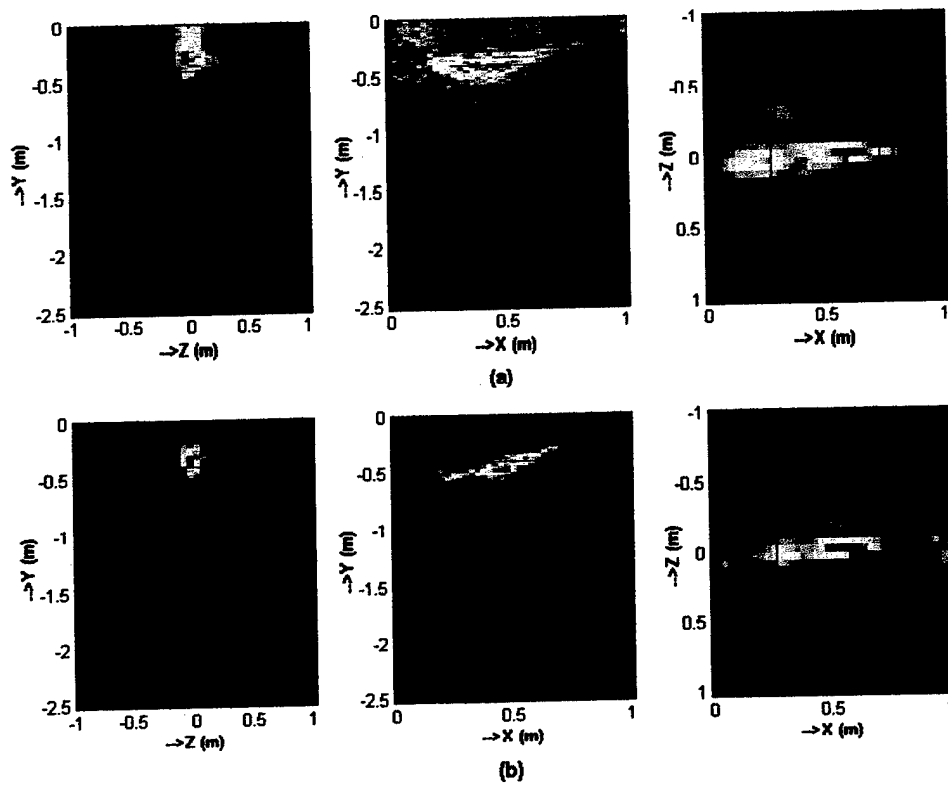


Figure 3. 2D projected GPR images for (a) measurement data, (b) simulation data.